

**University of Alberta**

**Rock Type Identification and Abundance Estimation From Hyperspectral Analysis**

by



**Jilu Feng**

A thesis submitted to the Faculty of Graduate Studies and Research in partial fulfillment  
of the requirements for the degree of Doctor of Philosophy

Department of Earth and Atmospheric Sciences

Edmonton, Alberta

Fall 2002



National Library  
of Canada

Acquisitions and  
Bibliographic Services

395 Wellington Street  
Ottawa ON K1A 0N4  
Canada

Bibliothèque nationale  
du Canada

Acquisitions et  
services bibliographiques

395, rue Wellington  
Ottawa ON K1A 0N4  
Canada

*Your file Votre référence*

*Our file Notre référence*

The author has granted a non-exclusive licence allowing the National Library of Canada to reproduce, loan, distribute or sell copies of this thesis in microform, paper or electronic formats.

The author retains ownership of the copyright in this thesis. Neither the thesis nor substantial extracts from it may be printed or otherwise reproduced without the author's permission.

L'auteur a accordé une licence non exclusive permettant à la Bibliothèque nationale du Canada de reproduire, prêter, distribuer ou vendre des copies de cette thèse sous la forme de microfiche/film, de reproduction sur papier ou sur format électronique.

L'auteur conserve la propriété du droit d'auteur qui protège cette thèse. Ni la thèse ni des extraits substantiels de celle-ci ne doivent être imprimés ou autrement reproduits sans son autorisation.

0-612-81187-5

**Canada**

**UNIVERSITY OF ALBERTA**  
**LIBRARY RELEASE FORM**

**NAME OF AUTHOR:** JILU FENG

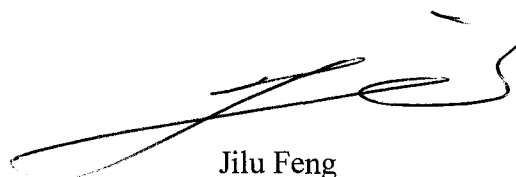
**TITLE OF THESIS:** ROCK TYPE IDENTIFICATION AND ABUNDANCE  
ESTIMATION FROM HYPERSPECTRAL ANALYSIS

**DEGREE:** DOCTOR OF PHILOSOPHY

**YEAR THIS DEGREE GRANTED:** 2002

Permission is hereby granted to the University of Alberta Library to reproduce single copies of this thesis and to lend or sell such copies for private, scholarly, or scientific research purposes only.

The author reserves all other publication and other rights in association with the copyright in the thesis, and except as hereinbefore provided, neither the thesis nor any substantial portion thereof may be printed or otherwise reproduced in any material form whatever without the author's prior written permission.



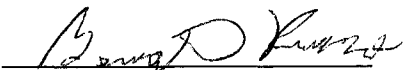
Jilu Feng  
F3, Garden Grove  
Edmonton, Alberta  
Canada, T6J 2L3

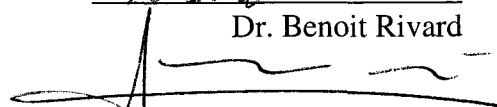
**DATED:** July 23, 2002


**University of Alberta**


**Faculty of Graduate Studies and Research**

The undersigned certify that they have read, and recommend to the Faculty of Graduate Studies and Research for acceptance, a thesis entitled *Rock Type Identification and Abundance Estimation From Hyperspectral Analysis* by *Jilu Feng* in partial fulfillment of the requirements for the degree of *Doctor of Philosophy*.

  
Dr. Benoit Rivard

  
Dr. G. A. Sanchez-Azofeifa

  
Dr. Andrew Bush

  
Dr. Moritz Heimpel

  
Dr. Ed Cloutis

Date: JULY 11 2002

## ABSTRACT

This study explores the usefulness of hyperspectral data to discriminate rock units and estimate the abundance of sulfides in rocks. Airborne visible-near infrared (VIS-NIR) hyperspectral data collected from northern Cape Smith, Quebec and laboratory thermal infrared reflectance (TIR) data measured on rock samples from eight different mines in the Sudbury Basin, Ontario are involved in the analysis. The study addressed four different geological application scenarios with the aim of retrieving useful lithological information from rock spectra while minimizing the influence of varying environmental factors.

The research first examines the effects of topography on the selection of rock endmembers from airborne VIS\_NIR spectra and demonstrates how a topographic correction process can improve the discrimination of rock units. It demonstrates that traditional ways of selecting spectral endmembers from hyperspectral data for areas of rugged terrain cannot provide representative rock unit signatures. The second part of the research targeted the mapping of wall rock in an underground environment using TIR spectra. Rock samples from mines of the Sudbury Basin in Ontario were measured using naturally broken surfaces both dry and wet to address environmental conditions encountered underground. An innovative method applying a spectral angle mapper on the 2<sup>nd</sup> derivative of rock spectra from 700-1300 cm<sup>-1</sup> was proved to be robust to remove the effect of liquid water, local geometry and disseminated sulfide ores while preserving diagnostic rock signatures for mapping. The study then focuses on retrieving sulfide information from TIR to estimate ore (total sulfide abundance) grade on naturally broken rock faces and separate ore-bearing rocks from their host rocks in an underground

environment regardless of rock types. An important finding is that reflectance at  $1319\text{ cm}^{-1}$ , where most silicate rocks demonstrate low reflectance, is related to total sulfide concentration in rocks. Finally, a study was conducted on core and cut rock faces to examine the usefulness of TIR in detecting sulfide ore zones and estimating total sulfide content in cores and cut rocks. Adaptable mathematical models were established and tested for potential core logging applications.

The most important result of this research is that rock spectra can be used to identify different rock types in an underground environment and on surface exposures in the field. Total sulfide content can be detected and predicted on naturally broken and cut rock faces using hyperspectral data.

## ACKNOWLEDGMENTS

I am very grateful to my supervisor, Dr. Benoit Rivard, who provides me rich opportunities to participate in his research projects. His projects laid the foundation both intellectually and financially on which this thesis is based. Many of the ideas and studies in this thesis are direct extension of this foundation. I feel honored to work and study with Dr. Rivard, who has been taking time and effort to teach me lessons that are beneficial both for my study and professional career.

Dr. Arturo Sanchez has given me constructive suggestions on my research. His help is as invaluable as that from a supervisor and a friend. I'd like to thank my other committee members, Dr. Andrew Bush, Dr. Jeremy Richards and Dr. Moritz Heimpel for their precious direction and advice guiding my research.

Thanks to the Geoide Network Centre of Excellence, NSERC, the Canadian Foundation for Innovation, the European Space Agency (ESA), Inco Ltd. and Bomem Inc. These institutions and industrial partners provided funding or in kind support for my research.

Thanks to Helen Francis, Brian Thompson, Greg Greenough and Wayne Garland from Inco Ltd in obtaining and identifying rock samples. Thanks to Dr. Ann Gallie, a research partner, of Laurentian University for her constructive criticisms and suggestions during my research. Thanks to Dr. John Miller of York University, for access to the Casi hyperspectral data. Thanks to Stephen Hamilton and Sheri Foley for their time and effort to polish my thesis manuscript. Thanks to Randy Pakan for technical assistance, and to my friend, Jinkai Zhang for his support in programming IDL.

I am deeply grateful to my wife Qin Zhou, a network specialist, who has contributed to my study endless hours of child care and set up a cozy and reliable home computing environment for me, and my parents for their support throughout my graduate career.



## TABLE OF CONTENTS

<b>CHAPTER 1: INTRODUCTION</b>	<b>1</b>
1.1 Key research avenues in geological hyperspectral analysis	2
1.2 Research conducted in this thesis	4
1.3 Major contribution to sciences	7
REFERENCES	7
<b>CHAPTER 2: THE TOPOGRAPHIC NORMALIZATION OF HYPERSPECTRAL DATA AND ITS IMPLICATIONS ON THE SELECTION OF SPECTRAL ENDMEMBERS FOR LITHOLOGIC MAPPING</b>	<b>13</b>
2.1 Introduction	13
2.2 Study area and data sets	16
2.3 Radiance correction	17
2.4 Implication on the selection of endmembers	19
2.5 Lithologic mapping using radiance corrected data	23
2.6 Discussion	24
2.7 Summary	25
REFERENCES	26
<b>CHAPTER 3: ROCK TYPE DISCRIMINATION IN A SIMULATED UNDERGROUND ENVIRONMENT USING 2<sup>nd</sup> ORDER DERIVATIVE THERMAL INFRARED REFLECTANCE SPECTRA</b>	<b>41</b>
3.1 Introduction	41

3.2. Sample suite and experimental setup	43
3.2.1 Sample suite	43
3.2.2 Measurement set-up	44
3.2.3 S/N ratio and spectral resolution	45
3.2.4 Reproducibility	46
3.3 Results and discussion	46
3.3.1 Role of liquid water	46
3.3.2 Effect of disseminated sulfides	48
3.3.3 Use of 2 <sup>nd</sup> order derivative spectra	48
3.3.4 Rock type discrimination	50
3.3.5 Assessment of rock type classification	51
3.4 Conclusions	53
REFERENCES	55

## **CHAPTER 4: ORE DETECTION AND GRADE ESTIMATION IN SUDBURY**

<b>MINES USING THERMAL INFRARED SPECTROSCOPY</b>	<b>73</b>
4.1 Introduction	73
4.2 Materials and methods	75
4.2.1 Sample suite	75
4.2.2 Instrumentation and set-up	76
4.2.3 Experimental work	77
4.3 Results and discussion	78

4.3.1 Spectral statistics	78
4.3.2 Spectral characteristics of ores and silicate-rich rocks	78
4.3.3 Identification of ore-bearing rocks	80
4.3.4 Correlation between reflectance and sulfide concentration	82
4.4 Conclusions	83
REFERENCES	85

## **CHAPTER 5: TOTAL SULFIDE ESTIMATION OF CORES AND CUT ROCK**

<b>SURFACES BY THERMAL INFRARED REFLECTANCE</b>	<b>105</b>
5.1 Introduction	105
5.2 Materials and methods	107
5.2.1 Sample description	107
5.2.2 Laboratory setup and experiment	108
5.2.3 Sampling strategy and data arrangement	109
5.3 Data modeling for rock slab	110
5.3.1 Calculation of local TSC (%) from the digital photo	111
5.3.2 Relationship between TSC and TIR signatures	111
5.4 Model validation on cores and cut rock faces	113
5.4.1 Spectral statistics	115
5.4.2 Qualitative assessment of models	117
5.5 Discussion on practical issues	120
5.5.1 Effect of spectral continuum removal	120
5.5.2 Model calibration	121
5.6 Conclusions	122

REFERENCES	124
<b>CHAPTER 6: SUMMARY AND CONCLUSIONS</b>	<b>146</b>
<b>APENDIX A: EFFECT OF CHANGES IN INSTRUMENT FIELD OF VIEW ON THE ESTIMATION OF SULFIDE ORE</b>	<b>150</b>
A1 Problem description and approaches	150
A2 Analysis of data from various FOV	151
A2.1 Square FOV	151
A2.2 Rectangle FOV	153
A3 Conclusions	155
REFERENCES	155
<b>APENDIX B: THEORY AND PROCESSING TOOLS FOR TIR SPECTROSCOPY OF GEOLOGIC MATERIALS</b>	<b>165</b>
B1 Spectroscopy	165
B2 Absorption and reflection of minerals and rocks	166
B3 Emissivity and reflectance in the thermal spectral region	168
B4 TIR research in geology and TIR spectral library of rocks and minerals	168
B5 Hyperspectral data analysis software	169
REFERENCES	170

## LIST OF TABLES

### CHAPTER 2:

Table 2.1 Standard deviation of peridotite and gabbro radiance DN on CASI bands before and after topographic correction	30
--	----

Table 2.2 Confusion matrix for accuracy assessment of rock units	31
--	----

### CHAPTER 3:

Table 3.1 List of rock samples included in the experiment	59
---	----

Table 3.2 Major mineral components from thin section analysis of rock samples	60
---	----

Table 3.3 List of samples used to assess reproducibility	61
--	----

Table 3.4 Confusion matrix of rock type classification assessment	62
---	----

Table 3.5 Endmember/classification statistics	63
---	----

### CHAPTER 4:

Table 4.1 List of rock samples	89
--------------------------------	----

Table 4.2 List of samples used to assess reproducibility	90
--	----

Table 4.3 Correctly identified ore-bearing samples at $1319\text{cm}^{-1}$ using CRR values	91
---	----

### CHAPTER 5:

Table 5.1 List of core and cut rock samples	129
---	-----

Table 5.2 Classification results of the digital photo for rock slab sp#8	130
--	-----

Table 5.3 Suspicious samples resulting from expectation test and the expected ore prediction bias	131
Table 5.4 TSC predicted from $TIR_{1319}$ and $TIR_{index}$	132
Table 5.5 Statistics of total sulfide predictions	133
Table 5.6 Error in TSC as a function of the model and confidence level	134

**APENDIX A:**

Table A1 Basic statistics of TSC and TIR1319 over varying square FOV	156
Table A2 TSC prediction errors from $TIR_{1319}$ model under different square dimensions of FOV	157

## LIST OF FIGURES

### CHAPTER 2:

- Figure 2.1 (a) Geographical location and regional geologic setting of the working region (modified after St-Onge and Lucas 1993); (b) Local geologic setting (modified after 1:50,000 geology map, Scott, 1988). 32
- Figure 2.2 Mean surface digital number (DN) of 325 pixels from Lake Vaillant (shown on Figure 2.1) extracted from radiance CASI data. 33
- Figure 2.3 Shaded terrain relief using the solar position at 15:25 GMT on July 27, 1995. Line A-B marks the location of a cross-ridge profile used to explore topographic effects. 34
- Figure 2.4 Elevation profile along transit A-B shown on Figure 2.2. 35
- Figure 2.5 (a) upper: Uncorrected Radiance DN along profile A-B (A corresponds to pixel #1 and B to pixel #60); (b) lower: Topographically corrected radiance DN. Diamond = band 1 (475.29um). Circle = band 2 (490.14um). Star = band 5 (619.55 um). 36
- Figure 2.6 Color composite image of CASI bands, Red=band 11 (881.04 nm), Green=band 7 (710.68 nm), Blue=band 3(540.52 nm); (a) Before radiance correction. (b) After radiance correction. 37
- Figure 2.7 (a) left: Data clusters of the 5 classes from unsupervised classification before topographic correction. Circles mark the traditional location for selecting possible endmembers; (b) right: Cluster breakdown after correction. Circles mark the positions of approximate cluster centers. Blue

+ green: volcanoclastic sediments, Yellow: gabbro, White: peridotite. Red:  
vegetated alluvium 38

Figure 2.8 (a) Histogram of endmembers on CASI band 3 (540.52nm); (b) Histogram  
of endmembers on CASI band 13 (969.24nm). Solid line: histogram after  
topographic correction, Dash-dot and dot line: histogram before  
topographic correction. 39

Figure 2.9 Distribution map of five classes created by applying 0.8 as the threshold to  
constrained spectral linear unmixing results. 40

### CHAPTER 3:

Figure 3.1 Averaged single scan signal-to-noise ratio (S/N) measured over five days  
using the MB102 FTIR and a 100% reflectance Infragold panel and global  
illumination. 64

Figure 3.2 Important atmospheric bands ( $\text{CO}_2$  and  $\text{H}_2\text{O}$ ) seen in the radiance spectra  
of the diffuse gold panel measured at  $16 \text{ cm}^{-1}$  spectral resolution. 65

Figure 3.3 Average RMS deviation in % reflectance from 4 four samples measured  
during the reproducibility test. 66

Figure 3.4 Effect of water on reflectance spectra: (a) upper: Spectra of granite and  
amphibolite under dry and wet conditions; (b) lower: %Ratio of radiance  
for the diffuse gold panel under wet and dry conditions. 67

Figure 3.5 Spectra of granite gneiss (sample #19) collected during the drying process.  
Six of the eleven spectra collected are displayed. The time interval  
between each acquisition was 20 seconds. 68



Figure 3.6 (a) Reflectance spectra of sulfide mineral powders and broken rock surfaces. The spectra of sulfide powder (212-600 um grain size) were measured in bi-directional reflectance mode at RELAB, Brown University. The powders were created from massive sulfide samples of the same Sudbury locality. Bold solid line = Granite sample #30; bold dash line = amphibolite sample #10; thin solid line = massive sulfide sample #9, 26% Cp, 63% PnPo; thin dash line = massive sulfide sample #1, 80% Cp, 15% PnPo; stars = chalcopyrite powder spectra; circles = pentlandite powder spectra; black squares = wet/dry ratio spectra of diffuse gold panel; (b) 2<sup>nd</sup> order derivatives of the spectra shown in (a). 69-70

Figure 3.7 Spectral angle (in radian) map for the diabase endmember. Darker spots represent smaller angle values indicating a higher similarity to the diabase endmember spectrum. Refer to Figure 3.8 for the locations of the diabase (DIA) spots. 71

Figure 3.8 Results of the rock type classification. (a) upper: Schematic representation of the image construct. Each square represents one spot/measurement; each column of squares includes all spectral measurements for one sample, and each pattern groups spectra from one rock type. The lighter coloured squares at the bottom of each column correspond to measurements from dry surfaces, while darker shades represent measurements from wet surfaces. There are no spectra in areas occupied by white squares. Rock acronyms are detailed in Table 3.1; (b) lower: Color-coded classification results using SAM applied to the 2<sup>nd</sup> order

**CHAPTER 4:**

Figure 4.1 Averaged single scan signal-to-noise ratio (S/N) measured over five days using the MB102 FTIR and a 100% reflectance Infragold panel and global illumination. 92

Figure 4.2 RMS error in % reflectance averaged for 32 measurements from four samples during the reproducibility test. 93

Figure 4.3 Average reflectance at  $1319\text{ cm}^{-1}$  for dry locations of sp50 (diamonds), 51 (squares), 52 (triangles), 55 (circles), and 59 (stars) as a function of the number of measurements for these samples. Results show that these samples exhibit a stabilized average at the end of the experiment. All results shown are for samples with measurement areas of  $4\times 4\text{ mm}$ . 94

Figure 4.4 Average reflectance at  $1319\text{ cm}^{-1}$  for wet locations of sp50, 51, 52, 55, and 59 as a function of the number of measurements for a these sample. Results show that these samples exhibit a stabilized average at the end of the experiment. Symbols as shown on Figure 4.3. 95

Figure 4.5 Average reflectance at  $1319\text{ cm}^{-1}$  for dry locations of sp53 (diamonds), 54 (squares), 56 (triangles), 57(circles), and 58(stars) as a function of the number of measurements for a these sample. Results show that these samples exhibit a stabilized average at the end of the experiment. 96

Figure 4.6 Average reflectance at  $1319\text{ cm}^{-1}$  for wet locations of sp53, 54, 56, 57, and 58 as a function of the number of measurements for a these sample.

Results show that these samples exhibit a stabilized average at the end of the experiment. Symbols as shown on Figure 4.5. 97

Figure 4.7 Comparison of spectra for typical dry ore-free rocks (sp33, sp17) and massive sulfides (sp1, sp14). The spectra labeled "wet panel" was acquired for the wetted Infragold panel. (By definition, the dry infragold panel has perfectly flat spectra with a reflectance of 100%.) 98

Figure 4.8 Continuum removed reflectance spectra of single measurements of dry, ore-bearing samples. The total sulfide % is shown in parenthesis for each sample. The continuum was calculated for the 500-4000  $\text{cm}^{-1}$  spectral range. 99

Figure 4.9 (a) Schematic representation of the artificial images displayed in b and c. Each square represents one spectral measurement, each column of squares includes all spectral measurements for one sample, and each pattern groups spectra from one rock type. The lighter coloured squares at the top of each column correspond to measurements from dry surfaces, while darker shades represent measurements from wet surfaces. There are no spectra in areas occupied by black squares; (b) continuum removed reflectance at  $1319\text{cm}^{-1}$  calculated from  $1080\text{-}1504\text{ cm}^{-1}$ ; (c) image shown in b with a threshold corresponding to  $>20\%$  total sulfide concentration. 100

Figure 4.10 Regression between total sulfide and CRR values at  $1319\text{ cm}^{-1}$  for the average of dry locations for a given sample. Continuum removal was

carried out from 1080-1504  $\text{cm}^{-1}$ . Total sulfide concentration was estimated via thin section point counting. 101

Figure 4.11 Regression between total sulfide and CRR values at 1319  $\text{cm}^{-1}$  for the average of wet locations for a given sample. See Figure 4.10 for additional details. 102

Figure 4.12. Regression between total sulfide and average CRR values at 1319  $\text{cm}^{-1}$ . The mean CRR values were calculated from all available dry and wet measurements for a given sample. See Figure 4.10 for additional details. 103

Figure 4.13 Observed minus predicted sulfide concentration for each ore bearing sample, the average norite, and the average quartz diorite. Positive values indicate an underprediction. Negative values indicate an overprediction. Predicted values were calculated using the regressions shown on Figure 4.10-4.12. 104

## CHAPTER 5:

Figure 5.1 (a) left: Digital photograph of rock slab (Sp#8) and the grid system (5 mm x 5 mm) showing each cell measured; (b) right: Supervised classification result showing white pixels as sulfide locations and black pixels as silicate matrix. 135

Figure 5.2 Schematic diagram of general layout of spots measured on cores. 136

Figure 5.3 Schematic diagram of general layout of spots measured on cut rock faces. 137

Figure 5.4 TIR spectra from typical spots on rock slab (sp#8) with different TSC values. 138

- Figure 5.5 (a) left: visualization of local TSC (%) Estimated from photo of sp#8. Brighter grid cells indicate higher local TSC; (b) middle: visualization of TIR spectral slice of reflectance at  $1319\text{cm}^{-1}$ . Brighter positions represent higher TIR values. (c) right: visualization of TIR ratios. Brighter squares indicate bigger spectral ratios and lower TSC values. 139
- Figure 5.6 (a) upper: relationship between TSC (%) and  $TIR_{1319}$  (%) on rock slab sp#8; (b) lower: relationship between TSC (%) and  $TIR_{ratio}$  on rock slab sp#8. 140
- Figure 5.7 Distribution of estimation error (residuals) for different spectral indices. (a) upper: estimation by  $TIR_{1319}$ ; (b) middle: estimation by  $TIR_{ratio}$ ; (c) lower: estimation by  $TIR_{index}$  (linear combination of  $TIR_{1319}$  and  $TIR_{ratio}$ ). 141
- Figure 5.8 Average reflectance at  $1319\text{ cm}^{-1}$  of five samples as a function of the number of measurements on each sample. 142
- Figure 5.9 Scatter plots of observed total sulfide from thin section analysis and predicted total sulfide by  $TIR_{1319}$  and  $TIR_{ratio}$ . 143
- Figure 5.10 Error distributions for ore free samples and ore containing samples. 144
- Figure 5.11 The effect of continuum removal on the relationship between TSC and reflectance at  $1319\text{cm}^{-1}$ . Black dots: original reflectance at  $1319\text{cm}^{-1}$ ; squares: reflectance at  $1319\text{cm}^{-1}$  after continuum removal over  $500\text{ cm}^{-1}$  to  $5000\text{ cm}^{-1}$ ; triangles: reflectance at  $1319\text{cm}^{-1}$  after continuum removal over  $1080\text{ cm}^{-1}$  to  $3000\text{ cm}^{-1}$ . 145

## APENDIX A:

- Figure A1 Schematic representation of simulating variable field of views on the cut surface of rock sample sp#8. 158
- Figure A2 (a) Mean TSC (diamond, from digital photo) and mean TIR<sub>1319</sub> (circle, from spectra) for all pixels at a given FOV. Results are shown for square FOV ranging 25-900mm<sup>2</sup>; (b) Standard deviation of local TSC (diamond) and TIR<sub>1319</sub> (circle) under various square FOV. 159
- Figure A3 Scatter plot of local total sulfide content (TSC) vs. thermal infrared reflectance at 1319 cm<sup>-1</sup> (TIR<sub>1319</sub>) at different square field of view sizes. Cross=5mm x 5mm FOV; Diamond=15mm x 15 mm FOV; Black dot=30mm x 30 mm FOV. 160
- Figure A4 Distribution of absolute prediction errors at different total sulfide concentration under 5mm x 5mm (square) and 30mm x 30 mm (black dot) field view setups. 161
- Figure A5 Distribution of total sulfide prediction errors from TIR<sub>1319</sub> model at different square (a) and rectangle (b) FOV sizes. 162
- Figure A6 Variation of mean and deviation of total sulfide prediction errors from TIR<sub>1319</sub> model under different square (a) and rectangle (b) FOV sizes. 1 x 1 is original 5mm x 5mm square FOV. N x N FOV sizes represent (Nx5mm) x (Nx5mm) square FOV. Star= mean (*m*) absolute prediction error; Diamond=standard deviation (*stdev*) of absolute prediction error; Circle=  $m+1.64*stdev$ . 163

Figure A7 Relationship between standard deviation of sulfide prediction errors from TIR<sub>1319</sub> model and physical field of view coverage. Empty circle=data from square FOV setup; Filled circle=data from rectangle FOV setup. 164

#### **APENDIX B:**

Figure B1 (a) Real (n) and Imagery (K) part of the complex refraction index of quartz (Clark, 1998); (b) TIR reflectance spectrum of quartz measured in this study. 172

## LIST OF ABBREVIATIONS

AVIRIS	<i>Airborne Visible/Infrared Imaging Spectrometer</i>
CASI	<i>Compact Airborne Spectrographic Imager</i>
Cp	<i>Chalcopyrite</i>
CRR	<i>Continuum Removed Reflectance</i>
DEM	<i>Digital Elevation Model</i>
DN	<i>Digital Number</i>
ESA	<i>European Space Agency</i>
FOV	<i>Field-of-view</i>
FTIR	<i>Fourier Transform InfraRed</i>
HYDICE	<i>Hyperspectral Digital Imagery Collection Experiment</i>
MIR	<i>Mid-infraRed</i>
MCT	<i>Mercury/Cadmium/Telluride</i>
PoPn	<i>Pentlandite and Pyrrhotite</i>
$R^2$	<i>Square of Correlation Coefficient ( R )</i>
RMS	<i>Root Mean Square</i>
SAM	<i>Spectral Angle Mapping</i>
S/N	<i>Signal to Noise ratio</i>
TSC	<i>Total Sulfide Content</i>
TIR	<i>Thermal Infrared Reflectance</i>
VIS	<i>Visible</i>
VNIR	<i>Visible and Near-infrared</i>



# CHAPTER 1

## INTRODUCTION

Hyperspectral sensors, unlike multispectral sensors (e.g., Landsat Thematic Mapper), provide co-registered images with high spectral resolution (<20nm) and have greater capability to discriminate compositional variations of exposed terrestrial materials. Using data acquired from airborne hyperspectral sensors, like AVIRIS (Kruse *et al*, 1997, 1993, 1990; Mustard *et al*, 1993, 1992, 1987; Boardman *et al*, 1997, 1994, 1993; Rowan *et al*, 1995), CASI (Staenz *et al*, 1992; Neville *et al*, 1995) and HYDICE (Resmini *et al*, 1997) over arid and semi-arid regions, researchers have demonstrated that these data have promising potential for geological applications. Most reported geological hyperspectral applications were conducted at a broad scale under a specific geological setting or environment (case based) using data collected from airborne sensors. Laboratory measurements of rock spectra (Lyon 1965; Vincent *et al*, 1975; Hunt *et al*, 1976,1974; Grove *et al*, 1992; Clark *et al*, 1997, 1984; Salisbury *et al*, 1993, 1991, 1985; Walter *et al*, 1989) were mostly conducted to find typical rock features, which if present could be used for mapping from airborne surveys. The future usefulness of hyperspectral data will depend on whether hyperspectral data can provide detailed information to identify the presence of different rocks/minerals and allow valid mapping of the abundance and spatial variation of rocks/minerals in different environments, and whether the approaches developed for a given mapping scenario can be adapted to other environments.

## 1.1 Key research avenues in geological hyperspectral analysis

In operational geological application scenarios, rocks can be situated in a variety of environments and exposing a variety of surface properties. Rocks can be exposed above ground in rugged terrain, which is the case for most field surveys, or underground on tunnel faces or on drill cores, which is the case in mining sites. Rock surfaces can be naturally broken, cut, dry or wet. This thesis will explore the possibility of identifying rock units and sulfide mineral assemblages in different environments while minimizing influences from the above factors. The following key revenues were identified in this research.

(a) Removing the effect of topography to facilitate rock endmember selection. Rock endmembers are the spectral representations of key rock units needed to be traced from hyperspectral data. Many of the approaches and tools available (Boardman *et al*, 1993; Bateson *et al*, 1997) for the selection of image endmembers have limitations when the hyperspectral data are not normalized to a uniform imaging geometry. At times the spectra identified in the field and in the laboratory (on rock samples collected in the field) suggest the existence of distinct endmembers that are unrecognized in the image data despite their occurrence over pixel size areas. Sometimes the spectral signatures of a selected “image endmember” (rock spectra selected from data cube) are not statistically representative of a distinct class because the spectral amplitude and feature depth of the endmember is dependent on location and imaging geometry, which are related to local slope and aspect of rugged terrain. Additionally, expected endmembers (pure pixels) can not often be determined confidently using multi-dimensional visualizing tools because topographic effects tend to smear the related data clusters which become mixed with each

other or with other irrelevant targets in the scene. Removing the topographic effect will unveil a clearer signature of a rock unit and facilitate the selection of representative endmembers necessary for rock unit mapping.

(b) Rock type identification in an underground environment using naturally broken surfaces. Rock unit mapping in an underground environment (such as a tunnel face) is of particular interest for the mining industry. It is closely related to mine exploration but generally overlooked by the remote sensing community. The complexity of underground rock face mapping comes from many environmental factors such as liquid water, the irregular orientation of local rock facets on broken rock surfaces and the influence of disseminated ore. Using hyperspectral technology in an underground environment represents a new application of remote sensing.

(c) Sulfide ore detection on broken and cut rock faces using hyperspectral analysis. The detection and abundance estimation of specific mineral assemblages is a challenging but useful application of hyperspectral data. Goetz (1982) demonstrated that spectroscopy could aid in mapping surface mineralogy. Crowley (1993) presented a study on mapping of evaporite minerals with AVIRIS in Death Valley. Kruse (1996) reported the potential of mapping -OH containing minerals from drill cores. No research has been conducted on detecting sulfide minerals in rocks using hyperspectral data. The occurrence of sulfide minerals is a common indicator of many types of mineralization, at times the sulfide minerals themselves are the mining targets. Sulfide ores can be seen in rock samples, on tunnel faces (might be dry or wet) or in cores. A robust approach for detecting the occurrence of sulfide minerals and a method for the fast estimation of their abundance could greatly benefit the mining industry by replacing some labor-intensive routines with

automated processes (such as the automation of core logging).

This thesis tackles the above issues on the basis of research projects sponsored by the mining industry and stemming from collaborations with industry. Though specific problems were targeted, the science contribution of this thesis resides in the fundamental research results with broad geological applications.

## **1.2 Research conducted in this thesis**

Chapter 2 explores how a topographic correction implemented using publicly accessible DEM's (digital elevation models) can significantly facilitate the selection of realistic rock endmembers from hyperspectral data. Using an example intended for lithologic mapping, the research illustrates the benefit of a topographic correction in combination with standard visualization tools for an improved visualization of rock endmembers, for the selection of statistically more representative rock spectra, and for the detection of subtle spectral variations introduced by rock compositions. CASI (Compact Airborne Spectrographic Imager) data over North Cape Smith, Quebec, is used to investigate the effects of topography on the selection of endmembers, and to test how the topographic correction process improves the discrimination of rock units necessary for lithologic mapping. A simple atmospheric correction method involving the removal of skylight is implemented in the pre-processing of the data prior to the application of a generic Lambertian radiance correction model using a DEM. The chapter does not focus on atmospheric or topographic correction models and their possible improvement, which have been discussed extensively (Smith *et al*, 1980; Teillet, 1982; Woodham *et al*, 1987; Proy *et al*, 1989; Meyer *et al*, 1993; Sandmeier *et al*, 1997; Dymond *et al*, 1999). Rather, it focuses on analyzing the merits of a topographic correction for the selection of

spectrally uniform and geologically meaningful rock endmembers.

Chapter 3 investigates the usefulness of thermal infrared reflectance spectroscopy (TIR) to map rock faces in an underground environment. Mapping of wall rock and rock cores in the underground environment is part of routine mine operations. It is generally conducted visually by geologists. Research in this chapter explores the feasibility of using thermal infrared reflectance (TIR) spectroscopy to automate this operation with a long-term aim of improving reliability and reducing operation costs. Rock types are identified using TIR spectroscopy while addressing important considerations relevant to the underground mining environment namely the presence of water on rock surfaces, the presence of disseminated sulfides in rocks, and the broken characteristics of freshly blasted rock which, unlike natural rock exposures, largely lack weathering minerals. A laboratory Fourier Transform Infrared (FTIR) spectrometer was used to measure reflectance spectra ( $500\text{ cm}^{-1}$ - $5000\text{ cm}^{-1}$ ) of rock samples on naturally broken surfaces. A total of twenty-nine samples covering 10 different rock types, including barren silicate rocks and sulfide disseminated rocks, were collected from eight mines around the Sudbury Basin in Ontario. Broken rock surfaces were measured wet and dry to address environmental conditions encountered underground. Spectral data were processed using 2<sup>nd</sup> order derivative analysis and the spectral angle mapper algorithm (Kruse *et al*, 1993) for rock type identification. This research resulted in a methodology for rock face mapping that minimizes the effects of environmental factors. Factors examined are liquid water on the rock surface, variations in local rock facet geometry and the presence of disseminated sulfides. The ability to map rock type in the underground environment using spectroscopy combined with ore grade estimation capability reported in chapter 4

and chapter 5, would be a valuable asset to the automation of mine operations.

Chapter 4 investigates the usefulness of thermal infrared reflectance spectroscopy (TIR) to estimate ore grade in an underground environment and separate ore-bearing samples from their silicate host rocks. Work was carried out under laboratory conditions to test the initial concept and all samples had naturally-broken faces, to mimic the situation in a freshly blasted underground opening. A total of twenty-six samples, including massive and disseminated ores, were collected from eight mines around the Sudbury Basin in Ontario. Rock surfaces were measured wet and dry to address environmental conditions encountered underground. The study demonstrates the feasibility to separated ore bearing rocks from barren rocks and estimate total sulfide (chalcopyrite + pyrrhotite + pentlandite) concentration using TIR reflectance data.

Chapter 5 extends the study of sulfide estimation to cut rocks and cores with a view towards future applications in the mining industry, especially towards automated core logging and sulfide ore grading, using TIR hyperspectral devices. The immediate goal was to assess whether sulfide-bearing cores and cut rocks could be discriminated from barren cores and whether their ore grade could be related to raw TIR spectral data rather than continuum removed spectra as used in chapter 4. Using raw (absolute) reflectance will improve the ability of detecting ore in real-time. An empirical relation was established between total sulfide content and TIR data. A suite of thirty samples, including 17 core sections and 13 cut rocks for a variety of rock types and sulfide contents collected from the Sudbury Basin in Ontario, are used to test the TSC-TIR model. Promising results indicate that it is possible to build a core-logging prototype sensor. Many application-related issues, such as the dimension of the instrument field of

view (FOV), the calibration model and the effect of removing the spectral continuum are also discussed in this study and the corresponding appendix.

### **1.3 Major contribution to sciences**

The major contributions of this thesis can be summarized as follows.

- (a) It establishes that the topographic normalization of hyperspectral data using publicly available topographic maps can significantly improve the ability of identifying proper rock unit endmembers from hyperspectral data collected over rugged terrains.
- (b) It demonstrates that underground rock face mapping is possible while minimizing the impacts of underground environmental factors, namely the presence of liquid water, the irregular orientation of rock faces and the presence of disseminated sulfide ores.
- (c) It demonstrates that sulfide ores (chalcopyrite + pyrrhotite + pentlandite) can be detected and the ore grade can be estimated using TIR hyperspectral data , regardless of whether the rocks are cut or broken, dry or wet. A unique band position ( $1319\text{cm}^{-1}$ ) is found in this study to be sensitive to the presence of sulfide minerals and the absolute reflectance at  $1319\text{cm}^{-1}$  is linearly related to the total sulfide concentration in cut rocks.

### **REFERENCES**

- Bateson, A. and Curtiss, B., 1997, A method for manual endmember selection and spectral unmixing. *Remote Sens. of Environ.*, **55**, 229-243.

- Boardman, J.W., 1993, Automating Spectra Unmixing of AVIRIS Data Using Convex Geometry Concepts. Summaries of the Fourth Annual JPL Airborne Geoscience Workshop, JPL Publication 93-26, Pasadena, California, **1**, 11-14.
- Boardman, J.W. and Huntington, J.F., 1997, Mineralogic and Geochemical Mapping at Virginia City, Nevada Using 1995 AVIRIS Data, Proceedings of the Twelfth ERIM Applied Geologic Remote Sensing Conference, Boulder, Colorado, 191- 198.
- Boardman, J.W. and Kruse, F.A., 1994, Automated Spectral Analysis: A Geological Example Using AVIRIS Data, North Grapevine Mountains, Nevada. Proceedings of the Tenth ERIM Applied Geologic Remote Sensing Conference, San Antonio, Texas. 407-418.
- Clark, R.N., 1997. Rock and Mineral Spectra, (Chapter 1). Manual of Remote Sensing, 3<sup>rd</sup> Edition.
- Clark, R.N. and Roush, T.L., 1984, Reflectance spectroscopy: Quantitative analysis techniques for remote sensing applications. J. Geophys. Res., **89(B7)**, 6329-6340.
- Crowley, J.K., 1993, Mapping Playa Evaporite Minerals with AVIRIS data: a First Report from Death Valley, California. Remote Sensing Environ., **44**, 337–356.
- Dymond J.R. and Shepherd J.D, 1999, Correction of the topographic effect in remote sensing. IEEE Trans. Geosci. Remote Sensing, **37(5)**, 2618-2620.
- Goetz, A.F.H., Rowan, L.C. and Kingston, M.J., 1982, Mineral Identification from Orbit: Initial Results from the Shuttle Multispectral Infrared Radiometer. Science, **218**, 1020–1031.
- Grove, C.I., Hook, S.J. and Paylor, E.D., 1992, Laboratory Reflectance Spectra of 160



- Minerals, 0.4 to 2.5 Micrometers. NASA-JPL Publication, **92-2**, Pasadena, 300.
- Hunt, G.R. and Salisbury, J.W., 1974, Mid-infrared spectral behavior of igneous rocks. Environmental Research Paper **496-AFCRL-TR-74-0625**, Hanscom Air Force Base, Air Force Cambridge Research Laboratories, U.S.A.
- Hunt, G.R. and Salisbury, J.W., 1976, Mid-infrared spectral behavior of metamorphic rocks. Environmental Research Paper **543-AFCRL-TR-76-0003**, Hanscom Air Force Base, Air Force Cambridge Research Laboratories, U.S.A.
- Kruse, F.A., 1996, Identification of minerals in drill core using hyperspectral image analysis of infrared reflectance spectra. *Int. J. of Remote Sensing*, **9**, 1623-1632.
- Kruse, F.A., 1997, Regional geologic mapping along the Colorado Front Range from Ft Collins to Denver using the Airborne Visible/Infrared Imaging Spectrometer (AVIRIS). Proceedings of the 12<sup>th</sup> International Conference on Applied Geologic Remote Sensing, Denver, Colorado, USA, **II**, 91-98.
- Kruse, F.A., Kierein-Yong, K.S. and Boardman, J.W., 1990, Mineral mapping at Caprite, Nevada with a 63-channel imaging spectrometer. *Photogrammetric Engineering & Remote sensing*, **56(1)**, 83-92.
- Kruse, F.A., Lefkoff, A.B. and Dietz, J.B., 1993, Expert system-based mineral mapping in Northern Death Valley, California/Nevada, using the airborne visible/infrared imaging spectrometer (AVRIS), *Remote Sens. of Environ.*, **44**, 309-336.
- Lyon, R.J.P., 1965, Analysis of rocks by spectral infrared emission (8-25  $\mu\text{m}$ ). *Econ. Geol.*, **60**, 715-736.
- Meyer P., Itten K.I., Kellenberger T., Sandmeier S. and Sandmeier R., 1993, Radiometric

- corrections of topographically induced effects on Landsat TM data in an alpine environment. *ISPRS J. Photogramm. Remote Sensing*, **48**, 17-28.
- Murphy, R.J., 1995, Mapping of Jasperoid in the Cedar Mountains, Utah, U.S.A., using Imaging Spectrometer Data, *Int. J. Remote Sensing*. **16(6)**, 1021–1042.
- Mustard, J.F., 1993, Relationship of soil, grass and bedrock over the Kaweak serpentinite mélange through spectral mixture analysis of AVIRIS data. *Remote Sens. of Environ.*, **44**, 293-308.
- Mustard, J.F., Hurtrez, S., Pinet, P. and Sontin, C., 1992, First results from analysis of coordinated AVIRIS/TMS, and ISM (French) data for the Ronda (Spain) and Beni Boussers (Morocco) Peridotites. Summaries of the Third Annual JPL Airborne Geosciences Workshop, AVIRIS workshop, Pasadena, CA. JPL Publication 92-14, **1**, 26-28.
- Mustard, J.F. and Pieters, C.M., 1987, Abundance and distribution of Ultramafic Microbreccia in Moses Rock dike: Quantitative application of mapping spectroscopy. *J. Geophys. Res.*, **92(B10)**, 10376-10390.
- Neville, R.A., Rowlands, N., Marois, R. and Powell, I., 1995, SFSI: Canada's First Airborne SWIR Imaging Spectrometer. *Canadian J. of Remote Sensing*, **21(3)**, 328-336.
- Proy, C., Tanre D. and Deschemps P.Y., 1989, Evaluation of topographic effects in remotely sensed data. *Remote Sens. of Environ.*, **30**, 21-32.
- Resmini, R.G., Kappus, M.E., Aldrich, W.S., Har-sanyi, J.C. and Anderson, M., 1997, Mineral Mapping with Hyperspectral Digital Imagery Collection Experiment

- (HYDICE) Sensor Data at Cuprite, Nevada, U.S.A. *Int. J. Remote Sensing*, **18(7)**, 1553–1570.
- Rowan, L.C., Bowers, T.L, Krowley, J.C, Anton – Pacheo, C., Gumiel, P. and Kingston, M.J, 1995, Analysis of Airborne Visible / Infrared Imaging Spectrometer (AVIRIS) Data of the Iron Hill, Colorado, Carbonate - Alkalic Igneous Complex. *Econ. Geol.*, **90**, 1966-1982.
- Salisbury, J.W., 1993, Thermal infrared (2.5-13.5  $\mu\text{m}$ ) spectroscopy: Laboratory data, Chapter 4, *in* Pieters, C., and Englert, P., *Remote Geochemical Analysis: Elemental and Mineralogical Composition*. Cambridge University Press.
- Salisbury, J.W. and Eastes, J.W., 1985, The effect of particle size and porosity on spectral contrast in the mid-infrared. *Icarus*, **64**, 586-588.
- Salisbury, J.W., Walter, L.S., Vergo, N. and D'Aria, D.M., 1991, *Infrared (2.1-25  $\mu\text{m}$ ) spectra of minerals*. Johns Hopkins University Press.
- Sandmeier S. and Itten K.I., 1997, A physically-based model to correct atmospheric and illumination effects in optical satellite data of rugged terrain. *IEEE Trans. Geosci. Remote Sensing*, **35**, 708-717.
- Smith J.A., Lin T.L. and Ranson K.J., 1980, The Lambertian assumption and Landsat data. *Photogrammetric Engineering & Remote sensing*, **46**, 1183-1189.
- Staenz, K., 1992, A Decade of Imaging Spectrometry in Canada. *Canadian J. of Remote Sensing*, **18(4)**, 187-190
- Teillet P.M., Guindon B. and Goodnough D.G, 1982, On the slope-aspect correction of multispectral scanner data. *Can. J. Remote Sensing*, **8(2)**, 84-106.
- Vincent, R.K., Rowan, L.C., Gillespie, R.E. and Knapp, C., 1975, Thermal infrared

spectra and chemical analysis of 26 igneous rock samples. *Remote Sens. of Environ.*, (4), 199-209.

Walter, L.S. and Salisbury, J.W., 1989, Spectral characterization of igneous rocks in the 8- to 12- $\mu$ m region. *J. Geophys. Res.*, **94(B7)**, 9,203-9,212.

Woodham R.J. and Gray M.H., 1987, An analytical method for radiometric correction of satellite multispectral scanner data, *IEEE Trans. Geosci. Remote Sensing*, (25), 258-171.

**CHAPTER 2**  
**THE TOPOGRAPHIC NORMALIZATION OF HYPERSPECTRAL DATA AND**  
**ITS IMPLICATIONS ON THE SELECTION OF SPECTRAL ENDMEMBERS**  
**FOR LITHOLOGIC MAPPING**

**2.1 Introduction**

For decades, topography has been known to introduce variations in the radiance detected by air and spaceborne sensors (Temps *et al*, 1977; Smith *et al*, 1980). The effect of topography on remotely sensed data has been explored by many researchers (Kimes *et al*, 1981; Conese *et al*, 1993; Itten *et al*, 1993; Sandmeier *et al*, 1997; Gu *et al*, 1998) who have attempted to model and reduce the influence of local terrain slope and aspect with the aim of improving land cover identification. Such studies have focused on multispectral data with the goal of looking at the anisotropic effects of topography on surface reflectance. Few examples in the literature explore the effect of topography in hyperspectral data sets, particularly in terms of its influence on the signature of spectral endmembers (Adams *et al*, 1986). In geology the analysis of hyperspectral data for lithologic mapping and mineral exploration is now becoming routine (Adams *et al*, 1986; Boardman *et al*, 1994) and the use of representative spectra of rock units of interest (generally referred to as endmembers in general terms) is key for referencing targets of interest.

Endmembers can be obtained from *in-situ* field measurements or, more typically, they are extracted from imagery data due to a number of possible constraints including the remoteness of the study area. Consequently, recent research (Boardman *et al*, 1993; Bateson *et al*, 1996; Ifarraguerra *et al*, 1999) has started to focus on the development of

methodologies (Kneubühler *et al*, 1998) that can be used to select feasible endmembers from hyperspectral data sets. Methodologies such as the Minimum Volume Transform (Craig *et al*, 1994), the N-Dimensional Projection (Jimenez *et al*, 1999), Convex Set Theory (Boardman *et al*, 1993), and the Maximum Noise Fraction Transform (Green *et al*, 1988; Gordon *et al*, 2000), have been proposed for the extraction of endmembers from hyperspectral data sets. Some have been implemented to visualize endmembers (Boardman *et al*, 1993, 1994) and others to perform the automatic selection of endmembers (Bowles, 1995; Winter, 1999).

In practice, many of the tools available for the selection of image endmembers have limitations. At times the spectra identified in the field and in the laboratory (on rock samples collected in the field) suggest the existence of distinct endmembers unrecognized in the image data despite their occurrence over pixel size areas. Sometimes the spectral signatures of a selected “image endmember” is not statistically representative of a distinct class because the spectral amplitude and feature depth of the endmember is dependent on location and imaging geometry. Additionally, expected endmembers can often not be determined confidently using multi-dimensional visualizing tools because topographic effects tend to smear the related data clusters which become mixed with each other or with other irrelevant targets in the scene.

Once defined from the image data, the endmembers can be used to classify each pixel in the image via either spectral similarity tools (e.g., spectral angle mapper, Kruse *et al*, 1993) or spectral deconvolution (e.g., spectral mixture analysis, Boardman *et al*, 1989). A common assumption of many spectral analysis methods that make use of spectral endmembers for image classification is that each pixel shares the same illumination and

imaging geometry as that of the endmembers selected. However, this assumption is rarely satisfied. The primary cause of heterogeneity in imaging geometry for different pixels is local topography, where varying surface slope and aspect (orientation) results in variably illuminated areas and thus variations in illumination intensity. Data acquired using high spatial resolution airborne sensors, such as CASI (Compact Airborne spectrographic Imager, ITRES Research Limited) and Probe (Earth Search Sciences, Inc.), are particularly sensitive to local topographic variations at the scale of meters (Conese *et al*, 1993). Due to the effect of topography, the spectra of neighboring pixels are subject to amplitude variations and thus contrast variations, in accordance with local slope and slope aspect. Endmember signatures selected from specific pixels are subject to these same variations and therefore may not form distinct clusters of pixels when viewed using multi-dimensional visualizing tools.

This paper explores how a topographic correction applied to hyperspectral data and implemented using publicly accessible 1:50,000 DEM's (digital elevation models), can significantly facilitate the selection of representative endmember signatures. Using an example intended for lithologic mapping, we illustrate 1) the benefit of a topographic correction in combination with standard visualization tools for an improved visualization of endmembers, 2) for the selection of statistically more representative endmember spectra, and 3) for the detection of subtle spectral variations. A simple atmospheric correction method involving the removal of skylight is implemented in the pre-processing of the data prior to the application of a generic Lambertian radiance correction model using a DEM. The paper does not focus on atmospheric or topographic correction models per-se, or their possible improvement, which have been discussed extensively (Teillet

1986; Woodham *et al*, 1987; Meyer *et al*, 1993; Sandmeier *et al*, 1997; Dymond *et al*, 1999; Proy *et al*, 1989). Rather, we focus on analyzing the merits of a topographic correction for the selection of spectrally uniform and geologically meaningful endmembers.

## 2.2 Study area and data sets

The selected study area is located in the Ungava peninsula of Northern Quebec, Canada (Figure 2.1) and covers an area of approximately 2 x 2 kilometers (Figure 2.1a and 2.1b). Ground cover consists largely of grasses and mosses with lichen partially covering rock outcrops. Relief is moderate and the altitude ranges from 1,500 - 1,750 feet with more than 80% of the terrain characterized by slopes less than 15°. The region is located geologically within the Cape Smith Belt (Figure 2.1a), which is generally interpreted to be a foreland fold and thrust belt of the early Proterozoic Ungava Orogen (St-Onge and Lucas, 1993). Outcrops of two early Proterozoic rock groups (ca 2.04-1.92 Ga; Parrish, 1989) are exposed in the study site. The Watts group, which contains distinctive mafic and ultramafic rocks including layered gabbro and layered peridotite, and the lower Povungnituk group, which comprises a sequence of complex clastic sedimentary rocks (sandstone, pelite, dolomite, basalt and minor gabbro and peridotite sills).

A detailed knowledge of the spatial distribution and continuity of the gabbro, peridotite, and sedimentary rocks is important for mining exploration efforts in the region. Numerous sulfide deposits have been discovered since the 1950's, and the mineralization has been found to be associated with differentiated mafic-ultramafic bodies (principally gabbro and peridotite sills and sheeted dykes) (GioVenazzo *et al*,



1989; Barnes, 1990). These sills and dykes range from several meters to 600 meters thick (M.R. St-Onge *et al*, 1993).

Due to the logistical difficulties associated with accessing this region, airborne remote sensing has been used for regional mapping. For this study we use CASI Radiance data acquired from a nominal altitude of 3,628 m above sea level near Lake Vaillant (73.84°W, 61.46°N), Cape Smith Belt around 15:00 GMT on July 27, 1995. The data was geometrically corrected using on board GPS data and re-sampled to a 10-meter spatial resolution. The CASI spectral data has 13 narrow spectral bands (2 nm-12 nm bandwidth) located between 0.43-0.96 nm and centered at 475.29 nm, 490.14 nm, 540.52 nm, 564.90 nm, 619.55 nm, 665.03 nm, 678.33 nm, 710.68 nm, 750.76 nm, 800.50 nm, 881.04 nm, 950.15 nm, and 969.24 nm. These band locations were carefully selected to maximize the possibility of differentiating compositional variations in ground targets.

To correct the influence of topography on CASI radiance using the radiance correction approaches described below, a digital elevation model created from a 1:50,000 topographic map with 50 meter grid was used in the process. The DEM was registered to CASI data with 10 meter pixel spacing and less than 1 pixel RMS registration error. Though the pixel spacing of the above DEM is 10 meters, it does not portray topographic details at a scale equivalent to that of the CASI pixels because of the limited spatial resolution of the original DEM.

### **2.3 Radiance correction**

The illumination over the study region comes from two different sources, direct and diffuse solar illumination. Terrain relief changes the direct solar illumination by modulating the solar radiance at different slope angles and aspects. Diffuse light, which is

a result of multiple scattering from atmospheric constituents, is non-directional and not significantly modulated by topography. It can, therefore, be treated as an additive term to the surface illumination. Before making the DEM-based radiance correction, the additive diffuse component must be subtracted from each pixel/spectrum.

For each spectral band, the additive component can be roughly estimated using the measured radiance of a deep lake within the scene (Chavez, 1988; Crippen, 1987, 1988), in this case Lake Vaillant (Figure 2.1b). This estimation is based on two assumptions: (1) the atmospheric conditions within the scene (2km x 2 km) are uniform, (2) the radiance of Lake Vaillant is negligible implying that the lake is sufficiently deep and clear, and (3) the lake surface is sufficiently calm to prevent the occurrence of glare. Figure 2.2 displays the average DN  $((W/m^2 \mu m^{-1} sr^{-1}) * 100)$  reading for 325 pixels of Lake Vaillant. This spectrum is taken to represent the overall contribution of diffuse light during data acquisition and was subtracted from each pixel in the scene at the onset of the analysis.

In this study scattering of the direct illumination by the surface was modeled using a Lambertian scattering model (Conese *et al*, 1993; Douté *et al*, 1998; Chang *et al*, 2000). More complex scattering models (Dymond *et al*, 1999; Sandmeier *et al*, 1997) were not explored because of the insufficient spatial resolution of the DEM. The Lambertian model provides a fast method to normalize the directional solar radiance that was calculated using:

$$NormalizedRadiance = RawRadiance * (\cos \theta / \cos i)$$

where  $\theta$  is the solar zenith angle at the time of acquisition and  $i$  is the local incidence angle, which can be determined using the DEM and the following equation:

$$\cos i = \cos \beta \cos \theta + \sin \beta \sin \theta \cos(\lambda - \phi)$$

where  $\beta$  is the terrain slope,  $\phi$  is the solar azimuth angle and  $\lambda$  is the local terrain aspect. *RawRadiance* represents the CASI detected radiance ( $(W/m^2 \mu m^{-1} sr^{-1}) * 100$ ) after removal of the diffuse component. The local instantaneous solar azimuth and solar elevation angle were calculated as  $212.85^\circ$  and  $37.86^\circ$ . Figure 2.3 shows a shaded relief of the study area using the solar position at the time of data collection. The radiance profiles (a transit from point A to point B on Figure 2.3) of three of the CASI bands (centered at 475.29nm, 490.14nm, and 619.55 nm,) were examined to assess the performance of the topographic correction in a typically rugged terrain. The transit is 600 meters long (covering 60 pixels) and crosses a ridge (dominantly peridotite) recording an elevation change from 1640 feet to 1690 feet (Figure 2.4). A comparison of the radiance profiles pre (Figure 2.5a) and post (Figure 2.5b) correction suggests that the correction process performs well for the normalization of dominant topographic effects in this terrain. Prior to the correction (Figure 2.5a), the modulation of radiance by topography resulted in a dome-shaped profile on which was superposed high frequency variations attributed to local differences in surface materials. The profile of the corrected data shows a flat baseline indicating that the dominant effect of topography along the 600 meters transit has been removed. Variations due to transitions in surface materials and coherent returns from adjacent pixels belonging to a common map unit are more clearly recognized. Consequently delineation of map units and their contacts is facilitated. A visual comparison of the uncorrected (Figure 2.6a) and corrected data (Figure 2.6b) for the entire study area shows the same improvement. The contrast between different cover/rock units is improved, and the boundary/contacts between units are better defined.

#### **2.4 Implication on the selection of endmembers**

To compare the spectral signatures of geological targets before and after the correction process and to examine the impact of the correction on the extraction of spectral endmembers, distribution maps of rock units were created from the CASI data. For this purpose an unsupervised classification (arbitrarily set to 18 classes for the whole region) was first conducted on the corrected data set using a pipe-line/Parallelepiped classifier (Richards, 1994). This step provided guidance for easily identifying endmembers and reducing the spatial scope to locate rock endmembers of specific interest, such as gabbro and peridotite. Five classes (gabbro, peridotite, two sedimentary rock types and vegetated alluvium) that fall in respective geological categories on the geological map were identified as physically meaningful units. The two sedimentary rock classes, which are mapped as volcanoclastic, are included in the analysis to assess the correctness of their contact with gabbro and peridotite. The vegetated alluvium is located near valleys or along rivers where rock outcrops are less abundant. The results of the unsupervised classification for the above noted five classes provided a suite of five masks that were applied to the corrected and uncorrected CASI data sets. Using only these 5 classes in our discussion avoids any unnecessary influence from other unknown classes and best highlights the topographic effect on an individual class.

Multi-dimensional scatter plots were used to explore the hyperspectral data. These provide an intuitive way to determine the separability of, and relationship between, different data clusters. Figure 2.7a shows a scatter plot of the data for the 5 classes prior to the correction. CASI band 3 (540.52 nm) and band 13 (969.24 nm) were carefully selected for their maximum separability of the five endmember classes. It is clear that all of the classes are shown as elongated pixel clusters before correction. The degree of

elongation is a function of topography, which in turn is determined by the spatial locations of all of the pixels within a specific class. The triangular cluster in the lower part of Figure 2.7a is actually composed of three endmember classes (peridotite, gabbro and one sedimentary unit). It is hard to separate these three clusters confidently on the scatter plot before the correction, because they overlap. Most of the gabbro pixels are mixed with peridotite and sediment before the correction. Figure 2.7b shows the scatter plot of these endmember clusters after the correction, and they are clearly separable using only bands 3 and 13. The correction process results in clusters with a near circular shape, indicating that the spectral signature of each ground target should be uniform and statistically normal. The correction process not only normalizes the endmember distribution, but also decreases the standard deviation of each endmember for all bands (Table 2.1) except band 12 (950.15 nm), a band subject to the influence of atmospheric water vapor. The decrease of the radiance variation caused by local topography results in spectral clusters for each endmember with a distribution closer to normal. The histograms of bands 3 and 13 (Figure 2.8a and 2.8b) suggest that the corrected data clouds for the above five classes can be approximated by a suite of normally distributed clusters. The benefit of the topographic correction for data analysis is not confined to facilitating the separation of gabbro and peridotite as in this particular case.

This case study also brings to our attention the way in which we can select proper endmembers. Figure 2.7a shows two well-known approaches used to select endmembers or training clusters for hyperspectral classification. In the first case, high-radiance pixels are selected for each cluster (shown in region A and B on Figure 2.7a) on the basis that these pixels demonstrate clearer spectral signatures with stronger spectral contrast. It

should be noted that such pixels are likely the over-illuminated pixels located on sun facing slopes. In the second case, the corners of the cluster convex hull (extremities like region C, D and E on Figure 2.7a) are selected on the basis that they represent distinct spectral signatures, which assumes that all of the pixels within the convex hull are mixtures of these signatures. However, when the topographic effect is present, as in Figure 2.7a, the above assumption is not valid because the extremities of the data clouds are endmembers displaced to that position as a result of the topographic influence (as in region D and E which are mainly peridotite in Figure 2.7a)). Consequently the selected pixels are most likely contaminated by over-illuminated or under-illuminated pixels, which do not represent the true mean signature of a class. Additionally, some endmembers can be hidden within the convex hull (i.e gabbro). Thus, endmembers selected by these methods are very likely “incomplete” or “non-representative” if the topographic effect is embedded in the data. The endmember list may be “incomplete” by lacking some endmembers that cannot be confidently selected because their data clusters are mixed with that of other classes. An example is gabbro, which cannot be distinguished from peridotite and volcanoclastic sediments, without a topographic correction. “Non-representative” endmembers means that the spectrum of a selected endmember from the un-corrected data is likely to be contaminated by pixels at extreme illumination conditions, or affected by other classes. An example is location C (Figure 2.7a), which is a mixture of over-illuminated pixels of the peridotite and one of the sediment units. When the clusters shrink following the topographic correction, their statistical centers (Figure 2.7b) are representative of each class. If a spectral mixture exists after the correction, a convex hull method can then be confidently applied to the

corrected data cube to locate or refine endmembers.

## **2.5 Lithologic mapping using radiance corrected data**

The distribution of gabbro and peridotite from the unsupervised classification generally coincides with the respective rock unit distribution on the published geologic map. This approach does not, however, ensure that they are properly mapped. This is because (1) the total number of classes, which is a subjective classifier input, influences the final distribution of gabbro and peridotite in the unsupervised classification, and (2) it is assumed that all pixels are pure, which means that target detection at the sub-pixel scale is not important. This assumption does not always hold in the study area, where gabbro dykes can be meters thick and thus smaller than one CASI pixel. Existing spectral mixing techniques (Boardman, 1991,1993) provide approaches for improving the tracing of these rock units at the sub-pixel scale, if the pure endmember spectra of gabbro and peridotite are available.

Pure endmembers of the above 5 classes were selected from a scatter plot of CASI band 3 (540.52  $\mu\text{m}$ ) and band 13 (969.24  $\mu\text{m}$ ) using radiance corrected data. Endmember spectra were created by interactively selecting and averaging the central 8 to 12 pixels of each cluster on the scatter plot (Figure 2.7b). When used as inputs into a constrained linear spectral unmixing (Adams *et al.*, 1985) model, the resulting abundance maps provide the distribution of the above five endmembers within the scene. A uniform threshold (0.8) for all five classes was applied to the individual endmember proportion images to create the distribution map shown on Figure 2.9. Applying 0.8 as a threshold to the unmixing results indicates that the distribution map shows pixels with more than 80% spatial coverage of the corresponding endmembers. The accuracy of the final map was

assessed using a confusion matrix (Congalton, 1999), which examines every pixel in each class and determines how many are attributed a proper “ground truth” category, and how many are misclassified when compared to the published geological map. The assessment (Table 2.2) indicates that the unmixing results achieved an overall accuracy of 83.4% for gabbro, peridotite and two sediment rock units (12,087 out of 14,486 pixels are properly classified). Gabbro shows the lowest accuracy (62%) which reflects that gabbro generally occurs as dykes whose thickness can be at the meter scale, and whose locational accuracy can therefore be greatly affected by small registration errors between the geologic map and the classification result; an error less than 10 meters in this case. Furthermore, gabbro is a rock type that is resistant to physical weathering and tends to generate resistant debris in the proximity to rock outcrops. Thus the CASI data represents not only the original location of gabbro occurrences, but quite possibly also that of gabbros that has undergone secondary transport – which would not be reflected on the geologic map.

## **2.6 Discussion**

It has been reported (Ekstrand, 1996; Conese *et al*, 1993) that over correction tends to occur with a bigger local incidence angle as a result of assuming a Lambertian surface scattering mode. This cannot be confirmed in this region because the DEM used is not detailed enough to distinguish correction errors; those due to the over correction of the Lambertian model and those due to the fact that micro-topography is not present in the 1:50,000 topographic map. Errors of registration between the geologic map and the unmixing results can affect quantitative assessment results, especially for rock units with small outcrops like gabbro dykes. Mis-registration due to instantaneous platform instability could cause errors not recognizable during registration but with significant



consequences for quantitative evaluation.

Geologic studies have shown compositional variations within the gabbros and peridotites exposed in the north Cap Smith region due to differentiation, mineralization and contact metamorphism (Barnes, 1990; M.R. St-Onge, 1993). The topographically corrected data cluster for peridotite (Figure 2.7b) does show a triangular shape rather than a circular one. This indicates that it may be possible to use topographically corrected CASI hyperspectral data to explore the compositional variability within the peridotites.

An issue raised but not included in this study is the sensitivity analysis of the DEM resolution. It would be important to know how the capability of differentiating rock outcrops will change as a function of the resolution of DEM used to correct the topographic effect. This is open to further study when proper DEM data become available.

## **2.7 Summary**

This case study suggest that publicly accessible 1:50,000 topographic maps can be used to remove the dominant topographic effects embedded in CASI hyperspectral data, and improve the ability of separating and tracing gabbro and peridotite in the north Cape Smith region, using an existing spectral unmixing methodology. The fast radiance correction approach, using the Lambertian model, taken in this research highlights the merit of making topographic corrections before selecting endmembers. When topographic effects are embedded in the data, methods typically used for the selection of endmembers, such as the convex hull method, can miss endmembers or select non-representative pixels as endmember candidates. Following the topographic correction, the statistical center of a specific data cluster is a more representative endmember location

for circular isolated clusters. For the mixed data cloud that displays convex extremities, the apices of the cloud can be confidently treated as endmembers for spectral mixtures.

### **Acknowledgement**

Field work was funded by grants to B. Rivard by the GEOIDE centre of the Networks of Centres of Excellence and NSERC and grant 2041 from the Canadian Foundation for Innovation to Arturo Sanchez. We wish to thank John Miller of York University, for access to the CASI hyperspectral data.

### **REFERENCES**

- Adams, J.B. and Smith, M.O., 1986, Spectral mixture modeling: A new analysis of rock and soil types at Viking Lander 1 site. *J. Geophys. Res.*, **91(B8)**, 8089-8112.
- Anger, C.D., Babey, S.K. and Adamson, R.J., 1990, A new approach to imaging spectroscopy of the terrestrial environment. *SPIE proceedings*, **1298**, Orlando, Florida, 72-86.
- Barnes, S.J., 1990, A new interpretation of the Katiniq Nickle Deposit, Ungava, northern Quebec. *Econ. Geol.*, **85**, 1269-1272.
- Bateson, A. and Curtiss B., 1996, A method for manual endmember selection and spectral unmixing. *Remote Sens. of Environ.*, **55**, 229-243.
- Boardman, J.W., 1989, Inversion of imaging spectrometry data using singular value decomposition. *Proceedings, IGARSS'89, 12th Canadian Symposium on Remote Sensing*, **4**, 2069-2072.
- Boardman, J.W., 1990, Inversion of high spectral resolution data, *Proc. SPIE Tech. Symposium*, **I298**, 222-233.

- Boardman, J.W., 1993, Automated spectral unmixing of AVIRIS data using convex geometry concepts. Summaries of the 4<sup>th</sup> annual JPL airborne geoscience workshop, 11-14.
- Boardman, J.W. and Kruse, F.A., 1994, Automated spectral analysis: A geologic example using AVIRIS data, north Grapevine Mountains, Nevada. 10<sup>th</sup> thematic conference on geologic remote sensing, ERIM, Ann Arbor, MI, **1**, 407-418.
- Chavez, P.S., 1988, An improved dark-object subtraction technique for atmospheric scattering correction of multispectral data. *Remote Sens. of Environ.*, **24**, 459-479.
- Cheng, A.F. and Domingue, D.L., 2000, Domingue, Radiative transfer models for light scattering from planetary surfaces. *J. Geophys. Res.*, **105**, 9477- 9482.
- Conese, C., Gilabert, M.A., Maselli, F and Bottai, L., 1993, Topographic normalization of TM scenes through the use of an atmospheric correction method and digital terrain models. *Photogrammetric Engineering & Remote sensing*, **59**, 1745-1753.
- Crippen, R.E. 1987, The Regression Intersection Method of Adjusting Image Data for Band Ratioing. *Int. J. of Remote Sensing*, **8(2)**, 137-155.
- Crippen, R.E., 1988, The dangers of underestimating the importance of data adjustments in band ratioing. *Int. J. of Remote Sensing*, **9**, 767-776.
- Douté, S. and Schmitt, B., 1998, A multiplayer bidirectional reflectance model for the analysis of planetary surface hyperspectral images at visible and near-infrared wavelengths. *J. Geophys. Res.*, **103**, 1367-31390.
- Dymond, J.R. and Shepherd, J.D, 1999, Correction of the topographic effect in remote sensing. *IEEE Trans. Geosci. Remote Sensing*, **37(5)**, 2618-2620.

- Ekstrand, S., 1996, LANDSAT TM-based forest damage assessment: correction for topographic effects. *ISPRS J. Photogramm. Remote Sensing*, **62**, 151-161.
- Giovenazzo, D., Picard, C. and Guha, J., 1989, Tectonic setting of Ni-Cu-PGE deposits in the central part of the Cape Smith Belt. *Geosciences Canada*, **16**, 134-136.
- Gu, D. and Gillespie, A., 1998, Topographic normalization of Landsat TM images of forest based on subpixel sun-canopy-sensor geometry. *Remote Sens. of Environ.*, **64**, 166-175.
- Ifarraguerri, A., 1999, Multispectral and hyperspectral image analysis with convex cones. *IEEE Trans. Geosci. Remote Sensing*, **37(2)**, 756-769.
- Itten, K.I. and Meyer, P., 1993, Geometric and Radiometric correction of TM data of mountainous forested areas. *IEEE Trans. Geosci. Remote Sensing*, **31**, 764-770.
- Kneubühler, M., Schaepman, M., Schläpfer, D. and Itten, K. I., 1998, Comparison of Different Approaches of Selecting Endmembers to Classify Agricultural Land by Means of Hyperspectral Data (DAIS-7915). *Proc. IGARSS Seattle*, **2**, 888-890.
- Kruse, F.A., Lefkoff, A.B., Boardman, J.B., Heidebrecht, K.B., Shapiro, A.T., Barloon, P.J. and Goetz, A.F.H., 1993, The Spectral Image Processing System (SIPS) - Interactive Visualization and Analysis of Imaging spectrometer Data. *Remote Sens. of Environ.*, **44**, 145 - 163.
- Meyer, P., Itten, K.I., Kellenberger, T., Sandmeier, S. and Sandmeier, R., 1993, Radiometric corrections of topographically induced effects on Landsat TM data in an alpine environment. *ISPRS J. Photogramm. Remote Sensing*, **48**, 17-28.
- Parrish, R., 1989, U-Pb geochronology of the Cape Smith belt and Sugluk block, northern Quebec. *Geoscience Canada*, **16**, 126-130.

- Proy, C., Tanre, D. and Deschemps, P.Y., 1989, Evaluation of topographic effects in remotely sensed data. *Remote Sens. of Environ.*, **30**, 21-32.
- Richards, J.A., 1994, *Remote Sensing Digital Image Analysis*. Springer-Verlag press. 210-280.
- Sandmeier, S and Itten, K.I., 1997, A physically-based model to correct atmospheric and illumination effects in optical satellite data of rugged terrain. *IEEE Trans. Geosci. Remote Sensing*, **35**, 708-717.
- Smith, J.A., Lin T.L. and Ranson, K.J., 1980, The Lambertian assumption and Landsat data. *Photogrammetric Engineering & Remote sensing*, **46**, 1183-1189.
- St-Onge, M.R. and Lucas, S.B., 1993, Geology of the eastern cape smith belt. Geological Survey of Canada, Memoir **438**.
- Teillet, P.M., 1986, Image correction for radiometric effects in remote sensing, *Int. J. Remote Sensing*, **7**, 1637-1651.
- Teillet, P.M., Guindon, B. and Goodenough, D.G, 1982, On the slope-aspect correction of multispectral scanner data. *Canadian. J. Remote Sensing*, **8(2)**, 84-106.
- Temps, R.C. and Coulson, K.L., 1977, Solar radiation incident upon slopes of different orientations. *Solar Energy*, **19**, 179-184.
- Woodham, R.J. and Gray, M.H., 1987, An analytical method for radiometric correction of satellite multispectral scanner data. *IEEE Trans. Geosci. Remote Sensing*, **25**, 258-171.

Table 2.1 Standard deviation of peridotite and gabbro radiance DN on CASI bands before and after topographic correction

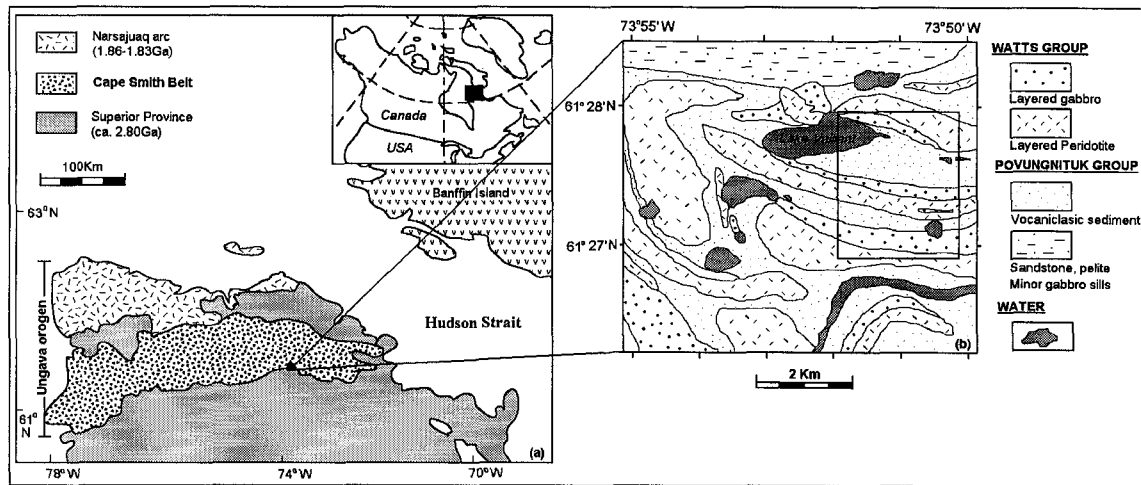
Band	Gabbro		Peridotite	
	Uncorrected	Corrected	Uncorrected	Corrected
1	841.05	623.56	820.88	445.96
2	787.64	644.12	769.53	461.26
3	790.33	612.45	802.52	456.25
4	791.14	594.54	827.58	456.58
5	744.99	567.63	806.14	451.28
6	713.74	563.42	776.46	450.25
7	699.31	558.29	762.90	447.39
8	697.95	405.83	777.14	331.71
9	705.31	292.95	808.61	246.22
10	656.15	270.14	766.58	231.43
11	655.91	263.69	744.56	219.56
12	266.54	287.79	287.27	227.17
13	522.11	281.18	559.70	220.93

Table 2.2 Confusion matrix for accuracy assessment of rock units

		Ground Truth (Pixels)			Total	Accuracy
		Peridotite	Gabbro	Sediment <sup>(a)</sup>		
Class (Pixels)	Peridotite	9044	1839	75	10958	82.53% (9044/10958)
	Gabbro	170	691	254	1115	61.97% (691/1115)
	Sediments <sup>(b)</sup>	0	61	2352	2413	97.47% (2352/2413)

(a) Povungnituk group, labeled as one unit on geological map

(b) Two merged classes (sediment1 and sediment2) fall in Povungnituk group





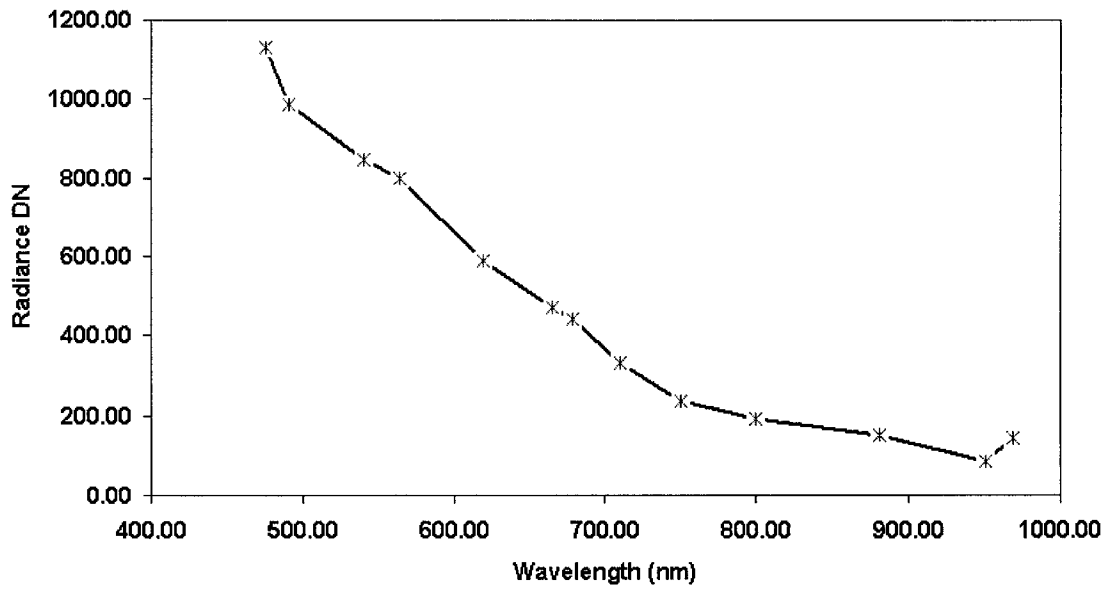


Figure 2.2 Mean surface digital number (DN) of 325 pixels from Lake Vaillant (shown on Figure 2.1) extracted from radiance CASI data.



Figure 2.3 Shaded terrain relief using the solar position at 15:25 GMT on July 27, 1995. Line A-B marks the location of a cross-ridge profile used to explore topographic effects.

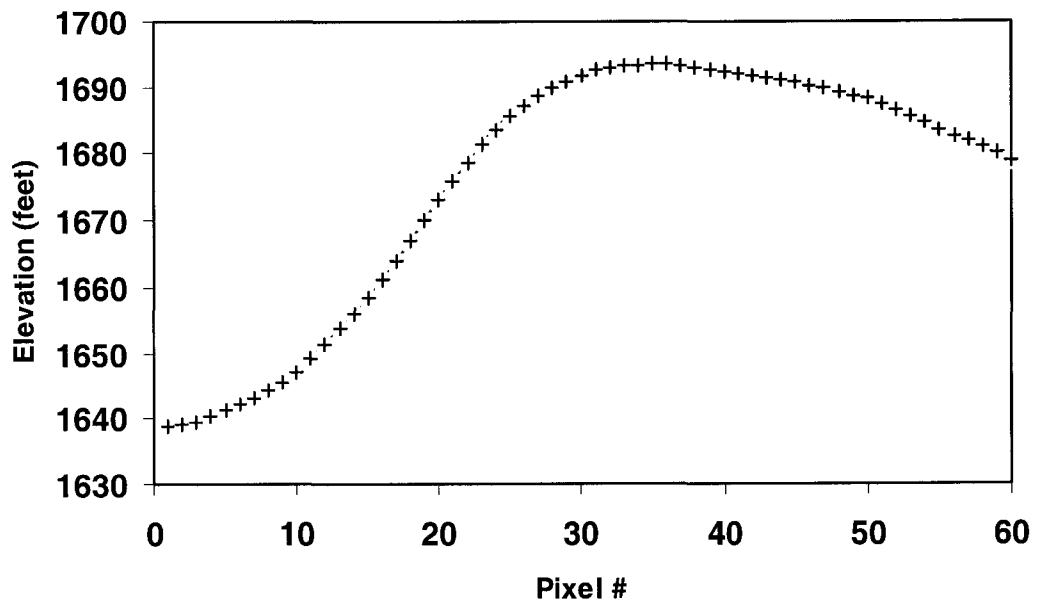


Figure 2.4 Elevation profile along transit A-B shown on Figure 2.2,

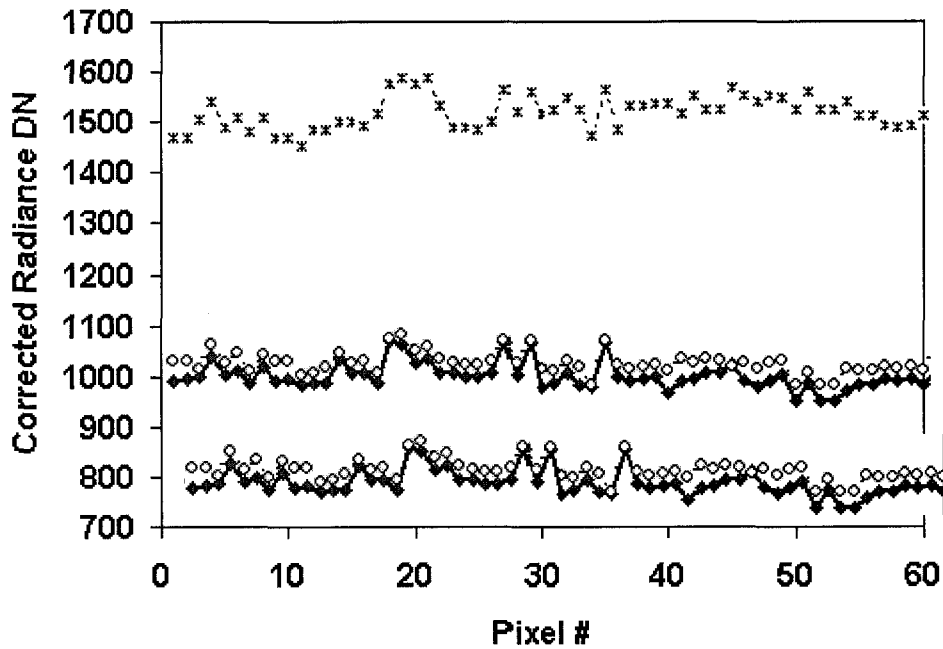
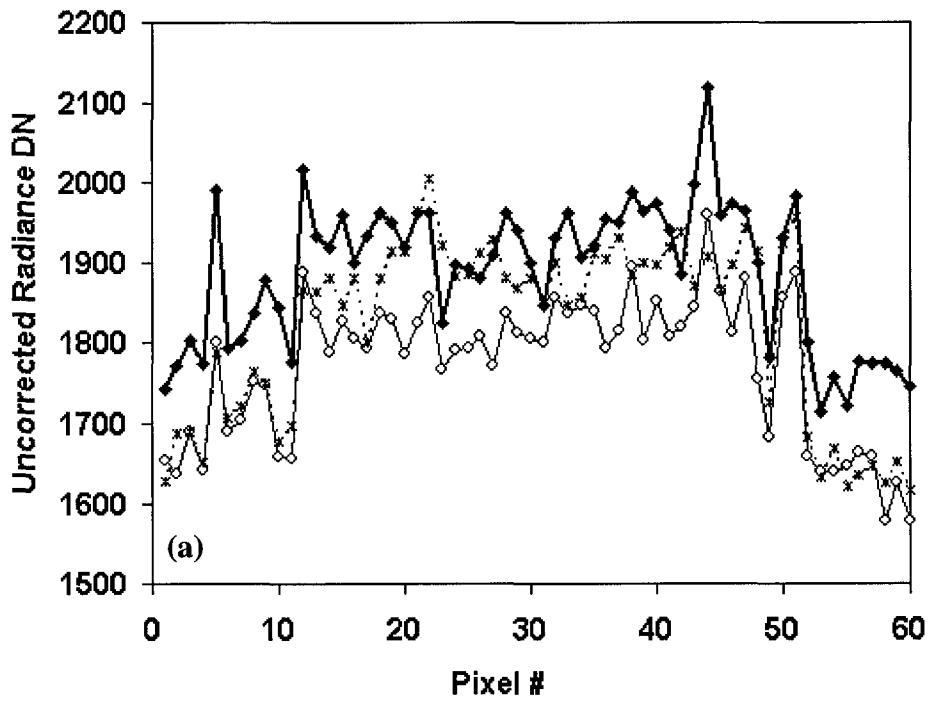


Figure 2.5 (a) upper: Uncorrected Radiance DN along profile A-B (A corresponds to pixel #1 and B to pixel #60); (b) lower: Topographically corrected radiance DN. Diamond = band 1 (475.29nm). Circle = band 2 (490.14um). Star = band 5 (619.55nm).

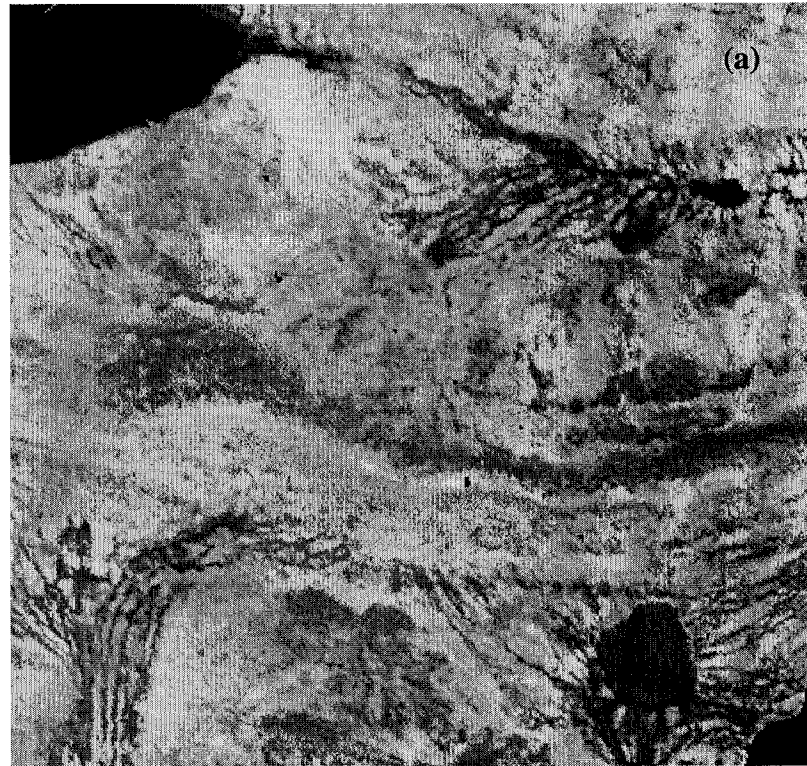


Figure 2.6 Color composite image of CASI bands, Red=band 11 (881.04nm), Green=band 7 (710.68nm), Blue=band 3(540.52nm); (a) upper: Before radiance correction, (b) Lower: After radiance correction.

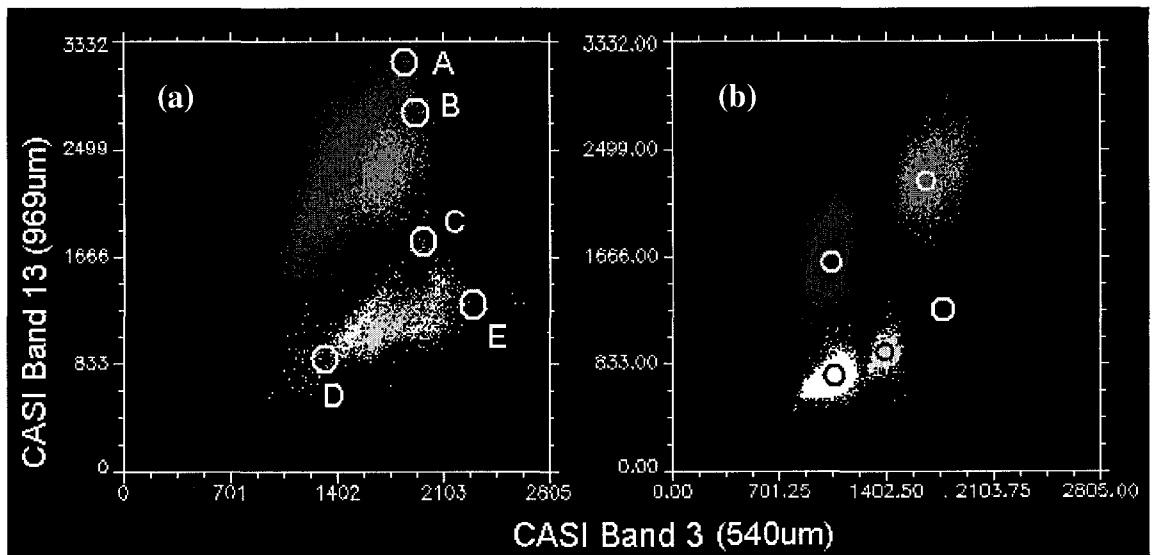


Figure 2.7 (a) left: Data clusters of the 5 classes from unsupervised classification before topographic correction. Circles mark the traditional location for selecting possible endmembers; (b) right: Cluster breakdown after correction. Circles mark the positions of confident endmembers. Blue + green : volcanoclastic sediments, Yellow : gabbro, White: peridotite. Red: vegetated alluvium.

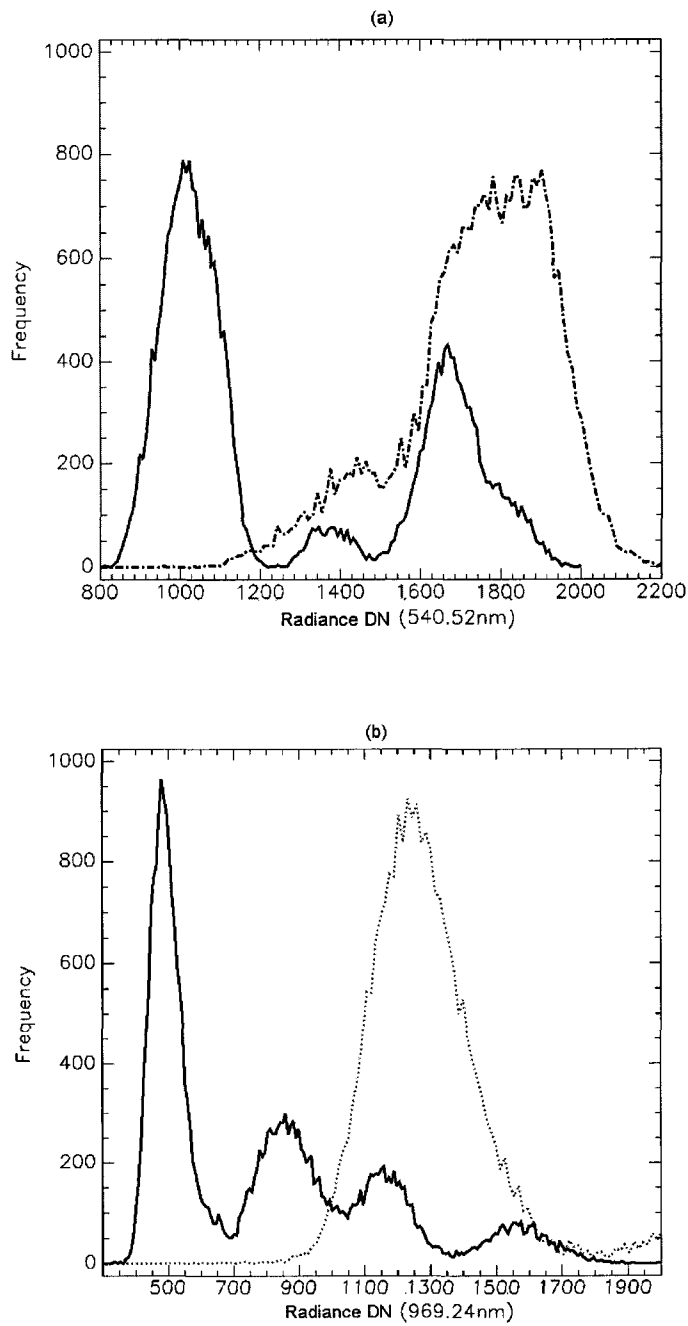


Figure 2.8 (a) Histogram of endmembers on CASI band 3 (540.52nm); (b) Histogram of endmembers on CASI band 13 (969.24nm). Solid line: histogram after topographic correction, Dash-dot and dot line: histogram before topographic correction.

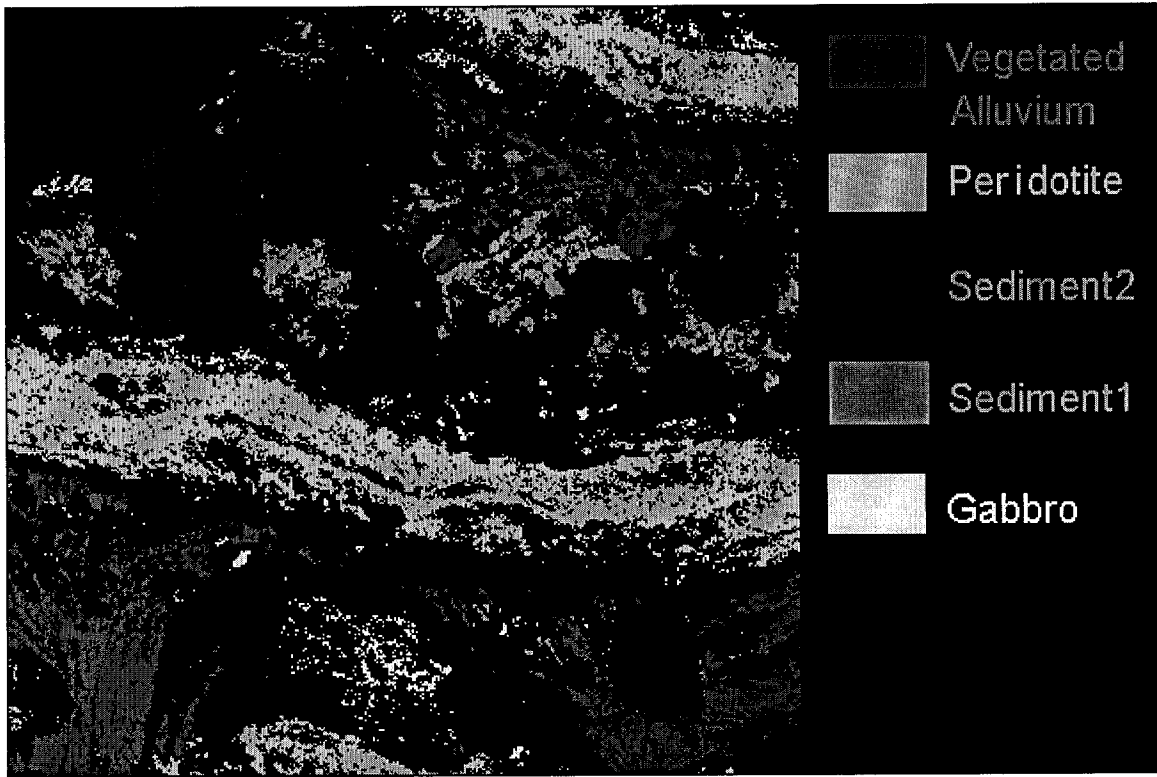


Figure 2.9 Distribution map of five classes created by applying 0.8 as the threshold to constrained spectral linear unmixing results.



## CHAPTER 3

# ROCK TYPE DISCRIMINATION IN A SIMULATED UNDERGROUND ENVIRONMENT USING 2<sup>nd</sup> ORDER DERIVATIVE THERMAL INFRARED REFLECTANCE SPECTRA

### 3.1 Introduction

Mapping of wall rock and rock cores in the underground environment is part of routine mine operations. Generally, the *in-situ* identification of lithologic units is conducted visually by geologists. This paper investigates the feasibility of using thermal infrared reflectance (TIR) spectroscopy to automate this operation with the long term aim of improving reliability and reducing operation costs.

Thermal Infrared Reflectance (TIR) spectroscopy generally refers to the traditional mid-infrared (MIR) spectral region, 3.0 to 30  $\mu\text{m}$ . Geological applications of TIR spectroscopy have been conducted for decades. Early research by Lyon (1965, 1972) revealed differences between mineral assemblages or within-mineral groups in rocks from the shape and intensity of the spectra and the presence of individual minima (or maxima). Vincent (1975) measured the hemispherical thermal reflectance of naturally weathered igneous rock surfaces. Hunt (1974, 1976), Clark (1984), Gillespie (1984), Kahle (1980, 1988), Salisbury (1991), and Christensen (1992) discussed the spectral features measured from rock powders and surfaces for a variety of rock types. These studies unveiled the key thermal infrared spectral features of rocks and minerals, especially near Restrahlen bands (reflectance peaks between  $700\text{ cm}^{-1}$  –  $1300\text{ cm}^{-1}$ ) and illustrated the possibility of using TIR for lithological mapping.

Numerous case studies have demonstrated the successful applications of visible/near-

infrared and thermal infrared multispectral and hyperspectral imaging technologies to detect the surface distribution of minerals, particularly in environments with low abundances of vegetation (Khale *et al*, 1988; Kruse *et al*, 1990; Rowan *et al*, 1995). A few studies (Gallie *et al*, 2001; Broicher 1999; Cudahy *et al*, 1997; Kruse 1996) have focused on the use of visible near-infrared (VNIR) spectroscopy to detect specific minerals in broken rock and rock cores, typical geological targets in the underground mining environment. More recently, Rivard *et al*, (2001) and Gallie *et al*, (2001) used thermal infrared reflectance (TIR) and VNIR spectroscopy for the estimation of sulfide mineral abundance (chacopyrite, pentlandite, pyrrhotite) in varying types of broken rocks for the purpose of ore grade estimation.

This study is aimed at identifying rock types using TIR spectroscopy while addressing important considerations relevant to the underground mining environment; namely, the presence of water on rock surfaces, the presence of disseminated sulfides in rocks, and the broken characteristics of freshly blasted rock which, unlike natural rock exposures, largely lack weathering minerals. The ability to map rock type in the underground environment using spectroscopy combined with ore grade estimation capability (Rivard *et al*, 2001, Gallie *et al*, 2001), would be a valuable asset to the automation of mine operations.

One of the unique challenges present in underground mining environments is that rock faces are likely to be wet or covered by thin liquid water films. In the VNIR spectral region, the presence of water results in a O-H (hydroxyl) stretch absorption feature at  $1.45\mu\text{m}$  and that combination absorption from the H-O-H bend and O-H stretch near  $1.92\mu\text{m}$  (Hunt *et al*, 1970). These water features affect the interpretation of rock spectra

for the application of VNIR spectroscopy underground because they occur at the same wavelength as hydroxyl (O-H) and H-O-H features caused by layered silicate minerals such as kaolinite and halloysite (characteristic absorptions at  $1.45\mu\text{m}$  and  $1.92\mu\text{m}$ ). However significant water features in the thermal region (near  $3450\text{ cm}^{-1}$ ,  $3200\text{ cm}^{-1}$ , and  $1640\text{ cm}^{-1}$ ) do not overlap with the  $700\text{ cm}^{-1}$  to  $1300\text{ cm}^{-1}$  region, where most silicate mineral features occur (Salisbury *et al*, 1991). Rivard *et al*, (2001) and Gallie *et al*, (2001) reported that some sulfides (chacopyrite, pentlandite, pyrrhotite) are almost featureless in this region, suggesting that it may be an appropriate spectral window for rock type analysis in the presence of disseminated sulfides. Consequently, this study focused on using TIR spectroscopy for rock type discrimination in underground environments.

### **3.2. Sample suite and experimental setup**

#### **3.2.1 Sample suite**

Laboratory experiments were undertaken to address these issues using 29 samples of 10 host rock types (Table 3.1) and 2 massive sulfides, as they would occur when freshly blasted and exposed in the underground mining environment. These samples were collected by mining geologists and represent the dominant rock types from eight mines in and around the Sudbury Basin in Ontario. The 10 rock types include quartz-rich rocks (e.g., granite, quartz diorite), mafic rocks (gabbro, diabase, amphibolite, norite) and a breccia (Sudbury breccia). The samples displayed freshly broken surfaces with grain size varying from fine (e.g greenstone) to coarse (e.g., some amphibolite). Samples of massive sulfide and disseminated sulfides in norite and quartz diorite were included in this study to explore how the presence of sulfide minerals would influence the

identification of rock types. The sulfide minerals are dominated by pentlandite ((Fe,Ni)<sub>9</sub>S<sub>8</sub>), chalcopyrite (CuFeS<sub>2</sub>), and pyrrhotite (Fe<sub>1-x</sub>S). Thin section point counting was conducted on each rock sample (Table 3.2) for mineralogical identification and rock type classification. Grain size and texture of each rock sample are also listed.

Rocks in Table 3.1 and Table 3.2 were originally named visually from hand sample by mine geologists. Rocks named as amphibolite, diabase, gabbro, greenstone, Sudbury breccia and metasediment by mine geologists are classified consistently with that determined later from the dominant minerals observed in thin section (e.g., amphibolites are rich in hornblende) or rock texture (e.g., Sudbury breccia is characterized by the presence of clasts and matrix or groundmass). Minor discrepancies occurred for naming some norite and quartz diorite samples; however, thin sections show that these samples do have similar mineral assemblages except for sp#13, which is altered and sericitized.

### **3.2.2 Measurement set-up**

Reflectance measurements were conducted with an MB102 Fourier transform InfraRed (FTIR) spectrometer equipped with a Mercury/Cadmium/Telluride (MCT) detector. A thermal light source (globar) provided illumination normally incident onto the sample surface. A globar light source was used because the underground environment acts as a blackbody cavity at a temperature similar to that of the target of interest complicating the detection of the emission properties of the rock surface (Rivard *et al*, 1995). The MCT detector was located approximately 50cm from the vertically oriented sample to perceive diffuse bi-directional reflected energy (Hapke, 1993) leaving a 15 mm x 15 mm field of view at a 35 degree phase angle. An infrared (IR) camera was used to locate the footprint of the light source on the sample because thermal infrared light is

not visible to the human eye. The detector perceives the reflected bi-directional thermal energy between  $450\text{ cm}^{-1}$  to  $6000\text{ cm}^{-1}$  at an adjustable wave number resolution. The control software provides the flexibility to co-add multiple scans of the same sample footprint to form a single spectra. A Diffuse gold panel (Infragold™) was used to normalize the radiance readings of natural samples to reflectance. The data presented in this study includes 1-4 spots (15x15mm) per sample. For samples with a heterogeneous texture, measurements were located to sample the variability. For every location measured, TIR spectra were collected for dry and wet conditions to simulate the extreme underground environment. Surfaces were wetted by applying clean water to form a water film and spectra were collected immediately.

### **3.2.3 S/N ratio and spectral resolution**

Signal to noise (S/N) was adequate, exceeding 1000 (Figure 3.1) over the entire spectral region of interest ( $700\text{-}1300\text{ cm}^{-1}$ ). It was estimated for a single scan while measuring a diffuse gold panel (Infragold™), a target of high and uniform reflectance. When measuring samples, 200 scans were averaged whenever possible to suppress noise, but a subset of the samples were measured using an average of 32 scans because of time constraints. This difference had little impact on the quality of the data in view of the high S/N of the instrument.

The MB102 FTIR provides selectable spectral resolution. Use of coarser resolution results in quicker acquisition. The diffuse gold panel was measured at a resolution of  $1\text{ cm}^{-1}$ ,  $2\text{ cm}^{-1}$ ,  $4\text{ cm}^{-1}$ ,  $8\text{ cm}^{-1}$ ,  $16\text{ cm}^{-1}$ ,  $32\text{ cm}^{-1}$  and  $64\text{ cm}^{-1}$  using 200 scans to determine an adequate resolution for this study. A set-up at  $16\text{ cm}^{-1}$  was selected for all measurements because it preserves known TIR spectral features of rocks.

Radiance spectra of the diffuse gold panel and rocks measured at  $16\text{ cm}^{-1}$  spectral resolution (Figure 3.2) display atmospheric bands caused by  $\text{H}_2\text{O}$  vapor (near  $1500\text{ cm}^{-1}$  and  $3750\text{ cm}^{-1}$ ) and  $\text{CO}_2$  (near  $680\text{ cm}^{-1}$  and  $2350\text{ cm}^{-1}$ ). These features are located outside the Restrahlen band ( $700\text{ cm}^{-1}$ - $1300\text{ cm}^{-1}$ ) of silicate minerals.

### **3.2.4 Reproducibility**

Four targets (fine-grained, coarse-grained, homogeneous and most heterogeneous) were used to assess measurement reproducibility (Table 3.3). Eight consecutive measurements were acquired for a given location on each sample within a time interval of eight minutes. Each measurement was an average of 200 scans at  $16\text{ cm}^{-1}$  spectral resolution. The root mean square (RMS) error over the entire region is between 0.15%-2.01% reflectance, absolute, with a mean value of 0.70 % (Figure 3.3). The error increases above 1.00% beyond  $4000\text{ cm}^{-1}$  (near-infrared region) due to the sensitivity fall off of the detector. These results indicate that the FTIR was very stable within the thirty-two minutes required for the acquisition of thirty-two measurements from four samples. Consequently measurement of the gold panel, required for the estimation of reflectance, was conducted approximately every thirty minutes.

## **3.3 Results and discussion**

### **3.3.1 Role of liquid water**

Water is known to have a high absorption coefficient in the infrared region (Clark, 1981). On broken rock surfaces, liquid water may form a thin film, which would substantially reduce rock reflectance. Figure 3.4a shows spectra of granite (sp#30) and amphibolite (sp#11) under both dry and wet conditions. These two samples represent mafic and felsic rocks, with clearly identifiable Restrahlen features of dominant silicate

minerals (75% hornblende in sp#11, 35% quartz in sp#30). Major features of mafic minerals tend to occur at smaller wave numbers (e.g., Hornblende feature at  $995\text{ cm}^{-1}$ ) than that of felsic minerals (e.g., Quartz feature near  $1180\text{ cm}^{-1}$ ). The combinations of spectral features from rock forming minerals provide the possibility of discriminating different rock types using spectral data. Spectra collected under wet conditions show a significant decrease in absolute reflectance from  $700\text{--}1300\text{ cm}^{-1}$ , but diagnostic features of minerals are preserved.

Figure 3.4b shows the ratio of radiance from a diffuse gold panel under wet and dry conditions. The ratio highlights the exact positions ( $3000\text{--}3900\text{ cm}^{-1}$ ,  $2100\text{ cm}^{-1}$ ,  $1670\text{ cm}^{-1}$ ) of liquid water absorption features over the thermal region. These results show a spectral region near  $980\text{--}1550\text{ cm}^{-1}$  with uniform values of the ratio indicating that liquid water may have a uniform effect on target spectra in this region. To assess whether this observation could be generalized to a variety of targets, a wetting experiment was conducted on 15 rock samples. For each sample, a series of spectra were collected at time intervals of 20 seconds after wetting. The data were collected with 32 scans to shorten the data collection time of each spectrum and sample the dynamic changes occurring during the drying process. A representative series of spectra is shown in Figure 3.5 for granite gneiss (sample #19). When samples are wetted, the average TIR reflectance is reduced (to 30% of dry amplitude near Restrahlen band on sp#19) and the spectral contrast is attenuated. During the drying process (vertical sample under ambient temperature), the overall spectral amplitude and contrast increase and approach that of the dry spectrum. Spectral features of water can overlap or mask rock features as seen for a hornblende feature ( $660\text{ cm}^{-1}$ ) in granite gneiss (Figure 3.5). Typically samples returned to a dry state

within five minutes (320 seconds for granite gneiss (#19) and 220 seconds for quartz diorite (#6)). As observed for the gold panel, the presence of water on rocks changes the rock spectra uniformly between  $980\text{ cm}^{-1}$ - $1550\text{ cm}^{-1}$  and changes the spectral amplitude and contrast without masking rock features. The  $700\text{ cm}^{-1}$ - $980\text{ cm}^{-1}$  region shows a smooth transition from a very shallow (less than 4% dry/wet ratio from center to shoulder of absorption) water absorption feature (near  $660\text{ cm}^{-1}$ ) to the  $980\text{ cm}^{-1}$ - $1550\text{ cm}^{-1}$  plateau. This observation provides an important basis for selecting spectral regions where rock features are retrievable under wet conditions.

### **3.3.2 Effect of disseminated sulfides**

Our previous research (Rivard *et al*, 2001, Gallie *et al*, 2001) on the spectroscopy of sulfide minerals (chalcopyrite, pentlandite and pyrrhotite) observed in our samples indicates that their spectra are featureless in the  $700\text{ cm}^{-1}$ - $1300\text{ cm}^{-1}$  region with the exception of a broad absorption of low amplitude for chalcopyrite centered near  $900\text{ cm}^{-1}$  (Figure 3.6a). This feature can be observed, though very weak, from the spectrum of the massive sulfide sample #9 on Figure 3.6a. The addition of these sulfides to silicate rich rocks attenuates the spectral features of silicate minerals but does not modify the relative amplitude of silicate features as was observed for the addition of surface water in the  $980$ - $1550\text{ cm}^{-1}$  region. As described below the effects of the broad chalcopyrite feature and the minor water feature over  $700\text{ cm}^{-1}$ - $980\text{ cm}^{-1}$  can be removed by using the 2<sup>nd</sup> order derivative of spectra during the process of rock type classification.

### **3.3.3 Use of 2<sup>nd</sup> order derivative spectra**

The analysis of 2<sup>nd</sup> order derivative spectra can be used to derive significant spectral parameters such as band position, band depth, band width and inflection points (Figure



3.6b) while suppressing the low frequency spectral background (continuum). It has been used for the spectral analysis of terrestrial materials (Huguenin *et al*, 1986; Farrington, 1994; Ben-Dor *et al*, 1997). In this study, the 2<sup>nd</sup> order derivative was computed for each spectrum for the 700 cm<sup>-1</sup>-1300 cm<sup>-1</sup> region to minimize the low frequency amplitude variations resulting from the presence of liquid water and disseminated sulfides. Figure 3.6b provides an illustration of the 2<sup>nd</sup> order spectra for the broken face of dry amphibolite, dry massive sulfide, dry granite, powder samples of chalcopyrite and pentlandite, and a wet/dry gold panel (shown as a ratio spectrum). For the sulfides and water, the 2<sup>nd</sup> order derivative values oscillate between -0.1 to 0.1 and converge to zero, which indicates that liquid water and sulfides do not have a significant influence on the 2<sup>nd</sup> order derivative spectra of rocks within the 700 cm<sup>-1</sup>-1300 cm<sup>-1</sup> region. These results are attributable to the lack of contrast in reflectance (absence of high frequency features) for these materials. Silicate-rich rocks display a variety of features from 700-1300 cm<sup>-1</sup> (Figure 3.6a) that result in distinct peaks and troughs after the 2<sup>nd</sup> order derivative transformation. These features are directly indicative of the mineral components within each sample with 2<sup>nd</sup> order derivative values reaching above 2.0 or below -2.0 (Figure 3.6b). Compared to 2<sup>nd</sup> order derivative values of distinctive rock features, values observed for water on gold and for sulfide rich samples are insignificant. Thus the use of 2<sup>nd</sup> order derivative spectra for rock type classification will greatly minimize the influence of water and disseminated sulfides. A disadvantage of the 2<sup>nd</sup> order derivative transformation is that it is sensitive to noise. A noise suppressing pre-processing step is generally required before calculating the 2<sup>nd</sup> order derivative. This step was not required

in this study due to the high S/N ratio of the data. The rock spectra collected in this study were transformed into 2<sup>nd</sup> order derivative spectra before classification.

### **3.3.4 Rock type discrimination**

Rock type mapping requires explicit knowledge of the representative spectral signatures of all the possible candidate rock types. In other words, a typical spectrum of each rock type, which is referred to as an endmember spectrum, must be known. However, the abundance and composition of minerals for a given rock type can be variable across localities, thus rock endmember spectra should be collected locally in order to achieve optimal mapping results. Based on rock types in Table 3.2, up to 4 spectra collected under dry conditions were selected for each rock type (Table 3.5) and averaged to create a representative endmember spectrum. Spectra for dry surfaces were selected because they demonstrate the strongest contrast. The process was guided by an unsupervised classification, which is indicative of the dominant spectra within each rock type, of the 700-1300cm<sup>-1</sup> subset from data cube. Ten endmember spectra, covering ten rock types, were created. Samples with disseminated sulfides (DIQD and DINR) were treated on the basis of the host rock type. Using the endmember spectra, the challenge is then to predict the rock type corresponding to all remaining spectra (> 67% of measurements) for dry, wet, sulfide bearing or barren samples.

As the measurements were collected from naturally broken rock surfaces to meet the original goal of this study, the micro-topography of rock surfaces must be considered because it will cause local changes in observation and illumination geometry that will modulate both the spectral amplitude and contrast of spectral features. The use of 2<sup>nd</sup> order derivative spectra will minimize variations in spectral amplitude but changes in

feature depth will not be normalized. The Spectral Angle Mapper algorithm (SAM) (Kruse *et al*, 1993) was applied to 2<sup>nd</sup> derivative spectra to classify rock type because SAM is sensitive to the shape of the spectrum and thus minimizes the effect of local surface topography. SAM is a spectral similarity mapping method based on vector analysis. The similarity index  $\alpha$  (measurement of the angle between two vectors or spectra) is determined between the rock endmember spectrum (vector  $R$ ) and an unknown

rock spectrum (another vector  $U$ ) and is given by  $\alpha = \cos^{-1} \left( \frac{\sum_{i=1}^{bands} (R_i * U_i)}{\sqrt{\sum_{i=1}^{bands} U_i^2} * \sqrt{\sum_{i=1}^{bands} R_i^2}} \right)$ . The

unknown rock spectrum that holds the smallest Angle ( $\alpha$ ) with respect to the endmember spectrum is considered to be most similar to the correspondent rock type. Because SAM uses only the relative direction of the spectra vectors and not their length (vector mode), SAM is insensitive to changes of gain factors caused by variation in illumination and viewing geometry. The rock type classification process using SAM in this study was conducted on 2<sup>nd</sup> derivative spectra using the 10 rock endmembers. For each unknown rock spectrum, 10 similarity indices (angles in radian) were calculated against 10 rock endmembers (see Figure 3.7 for an example) and the unknown rock spectra were classified to the rock type against which they held the smallest spectral angle. The results of the classification are shown in color-coded form in Figure 3.8(lower), where each color represents a rock type. Visual evaluation of the classification results shows that the general distribution of the classified rock types is close to the corresponding expected rock categories (top portion of Figure 3.8), which are listed in Table 3.2.

### 3.3.5 Assessment of rock type classification

Assessment of the classification results was conducted by examining the correctness of identification for each rock type. The correctness for each rock type (Table 3.5) was calculated from the confusion matrix (Table 3.4, Jensen, 1986) by counting the number of correctly identified spots among all the measurements for a given rock type. Highest correctness occurs for the most homogeneous (non-porphyrific, non-clastic, non-blebby and not foliated) rock types such as diabase (DIA) and gabbro (GAB) while lower correctness values occur for more heterogeneous rock types such as quartz diorite (QD, myrmekitic or foliated) and the Sudbury breccia (SBC, clastic). Grain size, water and the presence of disseminated sulfide minerals do not have obvious influences on correctness.

Most of the samples group well by rock types except for the quartz diorite (QD) where 7 out of 42 of the spots (17%) were misidentified as norite (NOR). This confusion appears to result from the similarity of the dominant mineral components in quartz diorite and norite based on thin section data. Norite and quartz diorite both contain hornblende and quartz as the dominant mineral component and biotite/plagioclase as secondary components. Because the field of view of each spot is only 15mm, local modal variations in heterogeneous rock surfaces (e.g myrmekitic or foliated quartz diorite) will bias the local identification results. The slightly weathered face of quartz diorite sp#7 was misidentified as greenstone. This is most probably due to the weathering process affecting the mineralogy though not verified by thin section data. Another low success case (44% correctness) was granite (GRA), 31% (5 spots out of 16) of which was classified as metasediment (MTSD). Thin section analysis indicates that the modal abundance of minerals in the granite samples varies significantly. K-feldspar in granite

changes from less than 5% to 60% and plagioclase varies from less than 5% to 55% in the 4 granite samples. These variations in modal proportions, combined with local modal variations due to the heterogeneous rock texture (e.g., Sp#34, granoblastic texture), will introduce uncertainty into the identification of local spots. Changes in the abundance of sulfides do not appear to affect the rock type identification of ore-bearing samples (maximum 35% total sulfide in quartz diorite sample #2). Norite samples with disseminated sulfides (DINR) were not successfully classified as norite. In the case of DINR sp#13, every spot was classified as amphibolite. Thin section observations show that it is poor in plagioclase, which is partially sericitized (5-9% sericite), compared to the norite end member, which is an average of spots from sp#3 and sp#17. The latter is richer in plagioclase.

The average correctness for all 10 silicate rock types covering felsic rock types and mafic rock types reaches 75%, whether they are wet, dry, ore bearing, or barren. Another assessment index (prediction accuracy), which is often referred to as the producer accuracy (Table 3.4), is also listed in Table 3.5 to measure the probability that a spot identified as a specific rock type is actually that type. When this index is equal or close to a higher correctness percentage listed in Table 3.2 for a given rock type (e.g., Granite gneiss and diabase), less confusion is achieved between that rock type and all other rock groups. This indicates that spectra from that rock group share common and unique features, which enable them to be easily isolated from all other classes, as their endmember. The average prediction accuracy reaches 80%.

### **3.4 Conclusions**

This research demonstrated that TIR spectroscopy at  $700\text{ cm}^{-1}$  -  $1300\text{ cm}^{-1}$  contains

diagnostic spectral information for silicate rocks and can be used to identify silicate rock types. A combination of derivative analysis and SAM is efficient in minimizing the effect of liquid water, of rock surface micro-topography and disseminated sulfides on spectral amplitude. The experiments also suggested that a spectral resolution of  $16\text{cm}^{-1}$  for TIR measurement provides enough spectral information to differentiate silicate rocks. A limited array of sulfide minerals was included in this study (chacopyrite, pentlandite and pyrrhotite) and additional work is required to extrapolate the results of this study to additional sulfide minerals. There are a few spectra in the literature for pyrite (Ferraro, 1982; Salisbury *et al*, 1991) indicating a high TIR and a lack of diagnostic spectral features within the  $700\text{-}1300\text{ cm}^{-1}$  region. Thus pyrite is not expected to have an obvious effect on the 2<sup>nd</sup> derivative spectra of rocks in accordance with the sulfide minerals included in this study.

Because the spectra were measured in a controlled laboratory environment with 50cm separating the sample and the spectrometer, atmospheric attenuation on the measured radiance was not significant. One factor that was not examined in this study is dust in the underground environment that may partially cover broken rock surfaces. The impact of dust on the spectra of rocks deserves further research before testing in an operational scenario.

A significant issue raised from this study is how to select proper rock endmembers representative of rock category or sub-category. For example, in the four granite samples, K-feldspar varies from 10% to 60% in modal abundance and plagioclase varies from less than 5% to 51%. These significant variations will obviously result in rock spectra distinct from the defined endmember, no matter how the endmember spectrum is selected. A

systematic study is required to group various rocks into sub-categories that carry unique spectral features suitable for hyperspectral analysis and consistent with lithological principles (Richard *et al*, 1979) widely accepted by geologists.

### **Acknowledgements**

The research was jointly funded by Inco Ltd and the European Space Agency (ESA). Access to a MB102 FTIR was provided by Bomem Inc.. The assistance of Brian Thompson, Greg Greenough and Wayne Garland, all from Inco Ltd., was invaluable in obtaining the samples.

### **REFERENCES**

- Ben-Dor, E., Inbar, Y. and Chen, Y., 1997, The reflectance spectra of organic matter in visible near-infrared and short wave infrared region (400-2500nm) during a controlled decomposition process. *Remote Sens. of Environ.*, **61**,1-15.
- Broicher, H.F., 1999, Ore and waste identification and quality control by means of laser induced fluoresce. *CIMM Bulletin*, **92**,59-63.
- Christensen, P.R., 1992, Thermal emission spectrometer experiment: The mars observation mission. *J. Geophys. Res.*, **97**,7719-7734.
- Clark, R.N., 1981, The Spectral Reflectance of Water-Mineral Mixtures at Low Temperatures. *J. Geophys. Res.*, **86**, 3074-3086.
- Clark, R.N. and Roush, T.L., 1984, Reflectance spectroscopy: Quantitative analysis techniques for remote sensing applications, *J. Geophys. Res.*, **89(B7)**, 6329-6340.
- Cudahy, T.J. and Ramanaidou E.R., 1997, Measurement of the hematite: goethite ratio

- using field visible near-infrared reflectance spectrometer in channel iron deposits, West Australia. *Australian J. of Earth Sciences*, **44**, 411-420.
- Farrington, G.A., 1994, Understanding spectra derivatives of water reflectance from high resolution airborne imagery. Proceedings of the 1<sup>st</sup> international airborne remote sensing conference and exhibition, France, **3**, 46-55
- Ferraro, J.R., 1982, *The Stadler infrared handbook of minerals and clays*: Stadler Research Laboratories, Philadelphia, 476.
- Gallie, E.A., Mcardle S., Rivard B. and Francis H., 2001, Estimating sulfide ore grade in broken rock using visible/infrared hyperspectral reflectance spectra. *Int. J. of Remote Sensing*, **11**, 2229-2246.
- Gillespie, A.R., Kahle, A.B. and Palluconi, F.D., 1984, Mapping alluvial fans in death Valley, California, using multichannel thermal infrared images. *J. Geophys. Res.*, **11**, 1152-1156.
- Hapke, B. 1993, Theory of reflectance and emittance spectroscopy *in* Arvidson, R., and Rycroft, M. J., Eds. *Topics in remote sensing*, Cambridge University Press.
- Huguenin, R.L. and Jones, J.L., 1986, Intelligent information extraction from reflectance spectra: absorption band positions. *J. Geophys. Res.*, **91**, 9585-9598.
- Hunt, G.R. and Salisbury, J.W., 1974, Mid-infrared spectral behavior of igneous rocks. Environmental Research Paper **496**-AFCRL-TR-74-062, Hanscom Air Force Base, Air Force Cambridge Research Laboraroies, U.S.A.
- Hunt, G.R. and Salisbury, J.W., 1976, Mid-infrared spectral behavior of metamorphic rocks. Environmental Research Paper **543**-AFCRL-TR-76-0003, Hanscom Air Force



- Base, Air Force Cambridge Research Laboratories, U.S.A.
- Jensen, J.R., 1986, *Introductory Digital Image Processing*, Prentice-Hall, Englewood Cliffs, New Jersey, 379.
- Kahle, A.B., Gillespie, E.A., Abbott, M.J., Walker, R.E. and Hoover, G., 1988, Relative dating of Hawaiian lava flows using multispectral thermal infrared images: a new tool for geologic mapping of young volcanic terranes. *J. Geophys. Res.*, **93**, 15239-15251.
- Kahle, A.B., Madura, D.P. and Soha, J.M., 1980, Middle infrared multispectral aircraft scanner data: analysis for geological applications. *Appl. Opt.* **19**, 2279-2290.
- Kruse, F.A., 1996, Identification and mapping of minerals in drill core using hyperspectral image analysis of infrared spectra. *Int. J. of Remote Sensing*, **17**, 1623-1632.
- Kruse, F.A. Kierein-Yong, K.S. and Boardman, J.W., 1990, Mineral mapping at Caprite, Nevada with a 63-channel imaging spectrometer. *Photogrammetric Engineering & Remote sensing*, **56(1)**, 83-92.
- Kruse, F. A., Lefkoff, A. B. and Dietz J. B., 1993. Expert system-based mineral mapping in Northern Death Valley, California/Nevada, using the airborne visible/infrared imaging spectrometer (AVRIS). *Remote Sens. of Environ.*, **44**, 309-336.
- Lyon, R.J.P., 1965, Analysis of rocks by spectral infrared emission (8-25  $\mu\text{m}$ ): *Econ. Geol.*, **60**, 715-736.
- Lyon, R.J.P. and Burns, E.A., 1963, Analysis of rocks and minerals by reflected infrared radiation. *Econ. Geol.*, **58**, 274-284.
- Richard V.D. and Brian, J.S., 1979, *Rocks and rock minerals*: John Willey & Sons, New York, U.S.A. 117.

- Rivard, B., Feng, J., Gallie, A. and Francis, h, 2001, Ore detection and grade estimation in Sudbury mines using thermal infrared spectroscopy, *Geophysics*, **66**, 1691-1698.
- Rivard, B., Thomas, P. and Giroux, J. 1995. Precise emissivity of rock samples: *Remote Sens. of Environ.*, **54**, 161-167.
- Rowan, L.C., Bowers, T.L., Crowley, J.K., Anto-Pacheco, C., Gumiel, P. and Kingston, M.J., 1995, Analysis of Airborne Visible-infrared Imaging Spectrometer (AVIS) data of the Iron Hill, Colorado, carbonatite-alkalic igneous complex. *Econ. Geol.*, **90**, 1966-1982.
- Salisbury, J.W., 1993, Thermal infrared (2.5-13.5  $\mu\text{m}$ ) spectroscopy: Laboratory data, Chapter 4, *in* Pieters, C., and Englert, P., Eds., *Remote Geochemical Analysis: Elemental and Mineralogical Composition*: Cambridge University Press.
- Salisbury, J.W. and Eastes, J.W., 1985, The effect of particle size and porosity on spectral contrast in the mid-infrared. *Icarus*, **64**, 586-588.
- Salisbury, J.W., Walter, L.S., Vergo, N. and D'Aria, D.M., 1991, *Infrared (2.1-25  $\mu\text{m}$ ) spectra of minerals*: Johns Hopkins University Press.
- Vincent, R.K., Rowan, L.C., Gillespie, R.E. and Knapp, C., 1975, Thermal infrared spectra and chemical analysis of 26 igneous rock samples. *Remote Sensing of Environ.*, **4**, 199-209.
- Walter, L.S. and Salisbury J.W., 1989, Spectral characterization of igneous rocks in the 8- to 12- $\mu\text{m}$  region. *J. Geophys. Res.*, **94(B7)**, 9203-9212.

Table 3.1 List of rock samples included in the experiment

Rock Type (Abbreviation)	Column <sup>f</sup> Position	Sample ID	# Dry <sup>c</sup>	# Wet <sup>c</sup>	Sulfide % (Cp <sup>d</sup> /PnPo <sup>d</sup> )
Amphibolite (AMPH)	1	10	3	3	0/0
	2	11	3	3	0/0
	3	16	3	3	0/0
Diabase (DIA)	4	21	3	3	0/0
	5	31	2	2	0/0
	6	38	4	4	0/0
DIQD <sup>a</sup>	7	2	3	3	3/32
	8	4	3	3	12/8
	9	26	3	3	2/11
	10	27	3	3	2/21
Gabbro (GAB)	11	32	3	3	0/0
	12	39	4	4	0/0
Granite gneiss (GRGN)	13	19	3	3	0/0
Granite (GRA)	14	18	1	1	0/0
	15	30	4	4	0/0
	16	34	2	2	0/0
	17	37	1	1	0/0
Greenstone (GRST)	18	12	4	4	0/0
	19	15	3	3	0/0
	20	22	4	4	0/0
Metasediment (MTSD)	21	5	3	3	0/0
	22	20	3	3	0/0
	23	25	3	3	0/0
Norite (NOR)	24	3 <sup>e</sup>	3	3	0/0
	25	3	3	3	0/0
	26	17	3	3	0/0
	27	24	3	3	0/0
DINR <sup>b</sup>	28	13	3	3	0/9
	29	23	3	3	0/25
Quartz Diorite (QD)	30	6	3	3	0/0
	31	7	3	3	0/0
	32	7 <sup>e</sup>	3	3	0/0
	33	33	3	3	0/0
Sudbury Breccia (SBC)	34	28	3	3	0/0
	35	29	3	3	0/0
	36	35	3	3	0/0
	37	36	3	3	7/2

<sup>a</sup> Sulfide Disseminated in Quartz Diorite; <sup>b</sup> Sulfide Disseminated in Norite; <sup>c</sup> Number of individual dry and wet measurements on each sample; <sup>d</sup> Sulfide contents from thin section point counts where Cp = chalcopyrite, PnPo= pentlandite and pyrrhotite; <sup>e</sup> Slightly weathered broken face of sample; <sup>f</sup> Refers to column number on Figure 3.8.

Table 3.2 Major mineral components from thin section analysis of rock samples

Rock Type <sup>a</sup>	Sample ID	Quartz / K-Spar <sup>b</sup> (%)	Hornblende <sup>c</sup> / Biotite (%)	Plagioclase / Pyroxene <sup>d</sup> (%)	Chlorite (%)	Olivine / Sericite (%)	Grain Size <sup>h</sup>	Texture
AMPH	10	25/-- <sup>e</sup>	70-75/--	1/--	AC <sup>f</sup>	--/--	M-C	Porphyritic
	11	15/--	80-85/--	<5/--	--	--/--	F	Porphyritic
	16	<5/--	60-65/<5	25-30/--	--	--/<3	F-M	Massive
DIA	21 <sup>g</sup>							
	31	--/--	--/AC	70/10-15	AC	10/AC	F-M	Granular
	38	--/--	--/<1	55-60/15-20	--	15/--	F-M	Inequigranular
DIQD	2	10-15/--	10-15/5-10	30-35/--	<5	--/<5	F-M	Equigranular
	4	4-8/12	28-32/20	12/--	5	--/--	F-M	Massive, incl <sup>i</sup>
	26	13-17/--	33/12	20-26/--	<4	--/--	F-M	Equigranular, blebby
	27	3-7/--	36/11-15	7-15/--	--	--/<7	F-M	Poikilitic, blebby
GAB	32	3/--	--/1	35/60	--	--/--	F-M	Inequigranular
	39	AC/--	--/--	45/--	50	--/AC	F-M	Equigranular
GRGN	19	65/--	<5/--	30/--	<5	1/--	M	Granoblastic
GRA	18	30/60	<1/10	<5/--	--	--/AC	F-M	Granoblastic, foliated
	30	30-35/40-45	--/5-10	5-10/--	AC	--/AC	C	Inequigranular
	34	37/10	--/<1	51/--	<3	--/AC	M	Granoblastic
	37	45/24	10/10	11/--	--	--/--	F-M	Inequigranular
GRST	12	45-50/--	30-40/15-20	AC/--	--	--/--	F	Foliated
	15	30/--	40/20	--/--	10	--/--	F	Foliated
	22	20-30/--	50-60/--	<5/--	5-10	--/<5	F	Porphyroblastic
MTSD	5	60-65/--	--/30-35	--/--	1	--/--	F	Foliated; clastic
	20	50/--	--/20-25	AC/--	20-25	--/--	F	Foliated
	25	80/<5	--/10	<5/--	--	--/--	F	Equigranular
NOR	3	10/--	55/5	25/--	--	--/AC	F-M	Massive
	17	15/<5	30-35/20-25	25/--	--	--/--	F-M	Massive
	24	35-40/1	30/5-10	20/--	--	--/--	F	Foliated
DINR	13	5-9/--	45-54/9	14-18/--	--	--/5-9	F	Equigranular
	23	12-15/--	23/15	23/--	--	--/AC	F-M	Equigranular
QD	6	20/5	45/10	15-20/--	--	--/--	F	Foliated
	7	15/--	45/5	35/--	--	--/--	F	Myrmekitic
	7 <sup>k</sup>							
	33	10-15/<5	45/10	30/--	--	--/--	F-M	Inequigranular
SBC	28	50-60/AC	--/<2	15-20/--	15-20	--/--	F-M	Clastic
	29	60-64/--	--/<5	--/--	8-12	--/--	F-M	Clastic
	35	60-65/--	11-13/--	14-16/--	--	--/--	M-C	Multi-clastic
	36	20/--	20/--	30/15-20	--	--/--	F-M	Minerals oriented

<sup>a</sup> Refer to Table 1 for rock name abbreviation; <sup>b</sup> K-Feldspar; <sup>c</sup> Including hornblende and Actinolite; <sup>d</sup> Including Pyroxene and Augite; <sup>e</sup> Not observed; <sup>f</sup> Occurred as accessory minerals; <sup>g</sup> No thin section available; <sup>h</sup> F=fine grained; M=medium grained; C=coarse grained; <sup>i</sup> with inclusions; <sup>k</sup> Refer to Table 1;

Table 3.3 List of samples used to assess reproducibility

<b>Property</b>	<b>Target type</b>	<b>Sample ID</b>
Homogeneous	Infragold™ standard panel	--
Coarse-grained	Granite	18
Homogeneous	Quartz Diorite	33
Heterogeneous	Sulfide Disseminated Norite	23 (40% Ore blebs)

Table 3.4 Confusion matrix of tock type classification assessment

		Ground Truth (classification by geologist)										Total spots
		AMPH	DIA	GAB	GRA	GRST	NOR&DINR	GRGN	QD&DIQD	MTSD	SBC	
Classes	AMPH	17	0	0	2	0	<i>6/0<sup>a</sup></i>	0	0	2	2	29/23
	DIA	0	18	0	0	1	0	0	0	0	0	19
	GAB	1	0	14	0	0	0	0	2	0	0	17
	GRA	0	0	0	7	0	0	0	0	0	0	7
	GRST	0	0	0	0	16	0	0	0	1	0	17
	NOR&DINR	0	0	0	0	2	20	0	7	0	4	33
	GRGN	0	0	0	0	0	0	5	0	0	0	5
	QD&DIQD	0	0	0	1	1	5	0	27	2	0	36
	MTSD	0	0	0	5	2	4	1	<i>6/0</i>	13	2	33/27
	SBC	0	0	0	1	0	0	0	0	0	14	15
Total spots		18	18	14	16	22	35/29	6	42/36	18	22	151 <sup>b</sup>

<sup>a</sup> Numbers in italic are excluding spots from weathered surfaces or with observed alteration. <sup>b</sup> Total number of correctly classified spots of all rock types.

Table 3.5 Endmember/classification statistics

Rock type	Total spots (dry/wet)	# selected <sup>a</sup> (dry/wet)	% EM <sup>b</sup>	Correctness <sup>c</sup>	Prediction accuracy <sup>d</sup>
AMPH	9 / 9	3 / 0	17%	94% (17/18)	56% (17/29) 74% (17/23) <sup>e</sup>
DIA	9 / 9	4 / 0	22%	100% (18/18)	95% (18/19)
GAB	6 / 6	3 / 0	25%	100% (14/14)	82% (14/17)
GRA	8 / 8	4 / 0	25%	44% (7/16)	100% (7/7)
GRST	11 / 11	3 / 0	14%	73% (16/22)	94% (16/17)
NOR & DINR	18 / 18	3 / 0	10%	57% (20/35)	61% (20/33)
GRGN	3 / 3	2 / 0	33%	83% (5/6)	100% (5/5)
QD & DIQD	24 / 24	4 / 0	8%	64% (27/42) 75% (27/36) <sup>f</sup>	79% (27/36)
MTSD	9 / 9	4 / 0	22%	72% (13/18)	39% (13/33) 48% (13/27) <sup>g</sup>
SBC	11 / 11	4 / 0	18%	64% (14/22)	93% (14/15)
<b>Average</b>				<b>75% / 77%</b>	<b>80% / 82%</b>

<sup>a</sup> Number of dry/wet spots selected for the calculation of the endmember in each rock category; <sup>b</sup> Percentage of endmember spots from total measured spots both dry and wet; <sup>c</sup> Calculated by counting the percentage of correctly identified spots out of total measured spots in each rock category. <sup>d</sup> Calculated by counting the percentage of correctly identified spots out of all spots classified as a given rock category. <sup>e</sup> Excluding sp#13. <sup>f</sup> excluding the spots on slightly weathered surface. <sup>g</sup> See discussion in text.

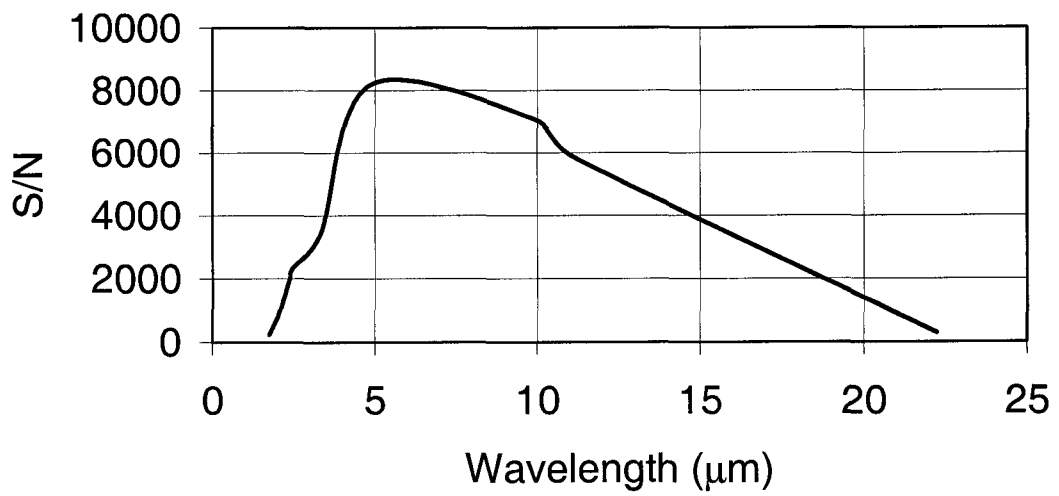


Figure 3.1 Averaged single scan signal-to-noise ratio (S/N) measured over five days using the MB102 FTIR and a 100% reflectance Infragold panel and global illumination.



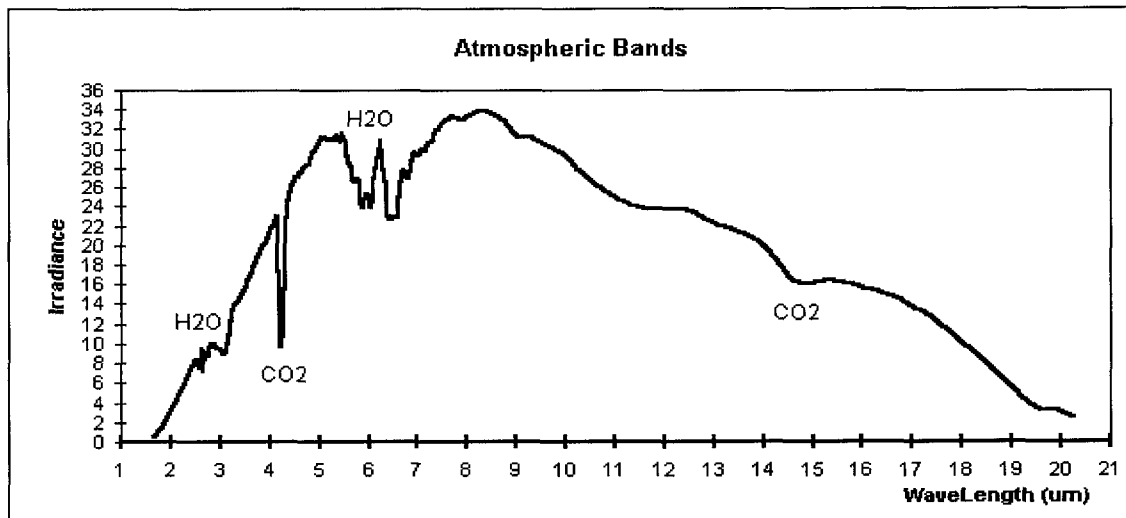


Figure 3.2 Important atmospheric bands ( $\text{CO}_2$  and  $\text{H}_2\text{O}$ ) seen in the radiance spectra of the diffuse gold panel measured at  $16 \text{ cm}^{-1}$  spectral resolution.

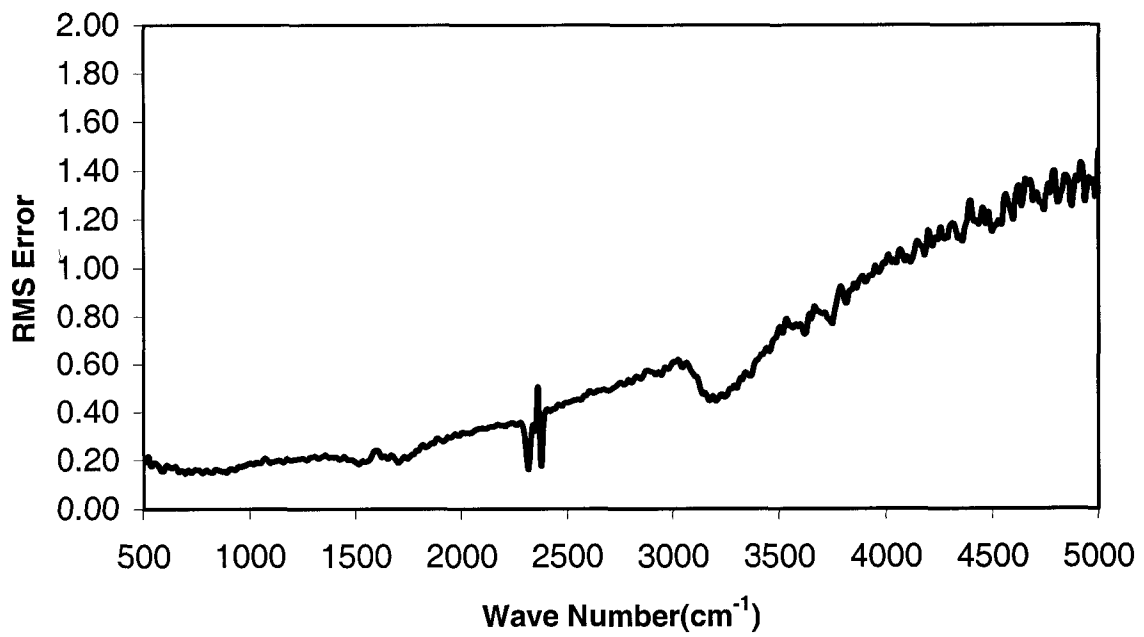


Figure 3.3 Average RMS deviation in % reflectance from 4 four samples measured during the reproducibility test.

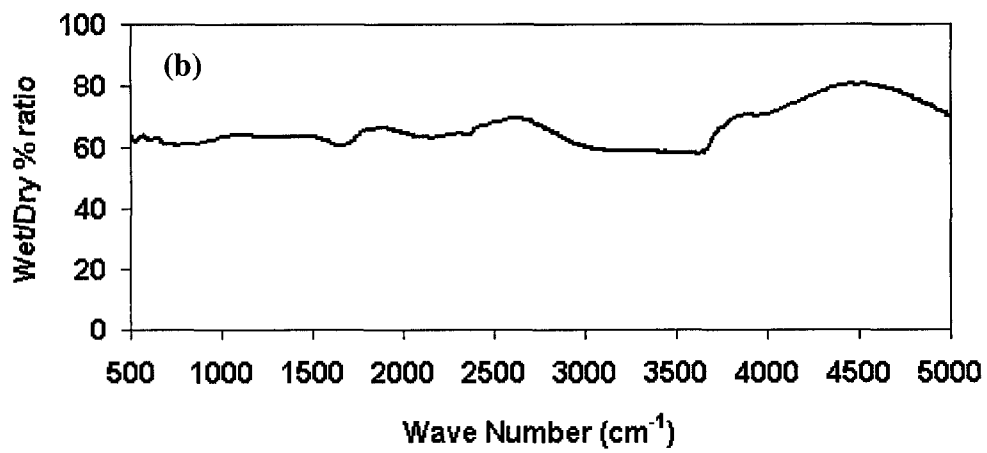
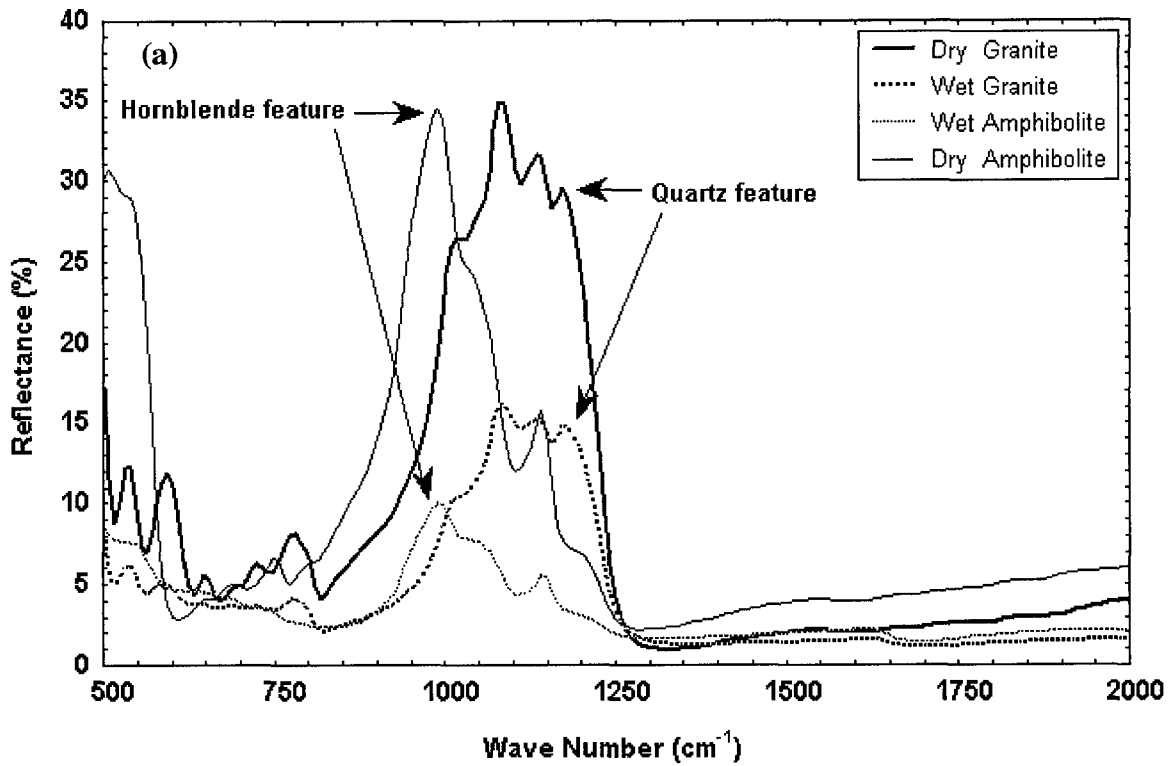


Figure 3.4 Effect of water on reflectance spectra: (a) upper: Spectra of granite and amphibolite under dry and wet conditions; (b) lower: %Ratio of radiance for the diffuse gold panel under wet and dry conditions .

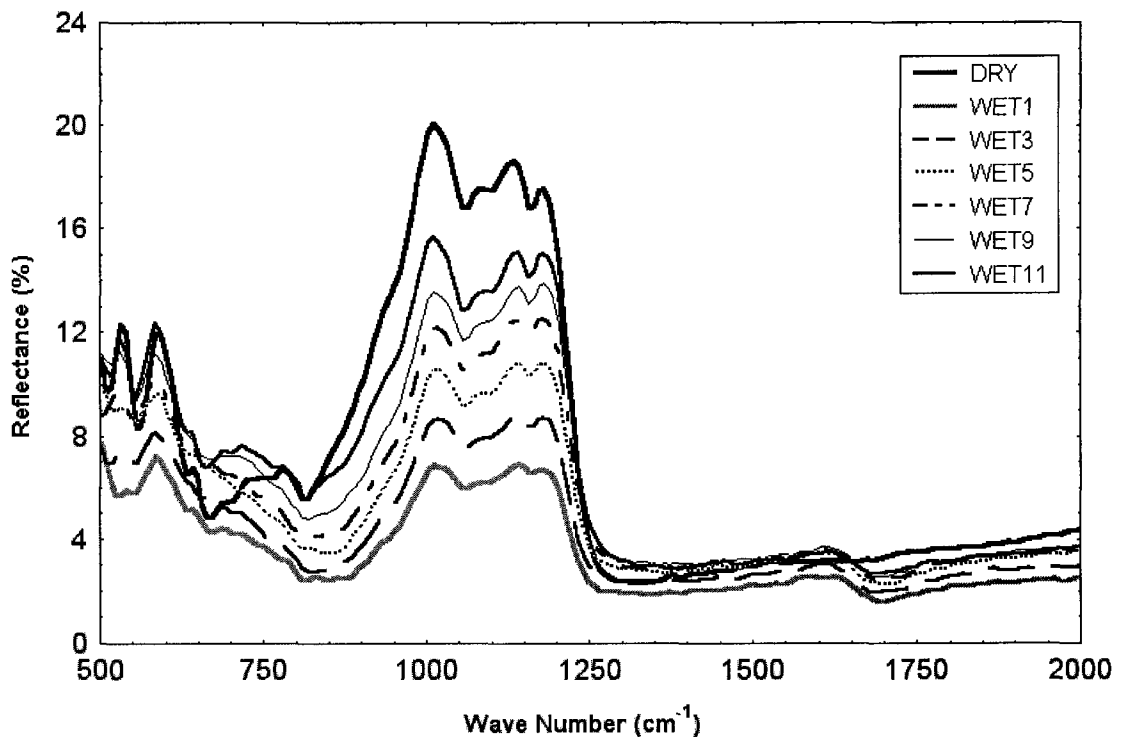


Figure 3.5 Spectra of granite gneiss (sample #19) collected during the drying process. Six of the eleven spectra collected are displayed. The time interval between each acquisition was 20 seconds.

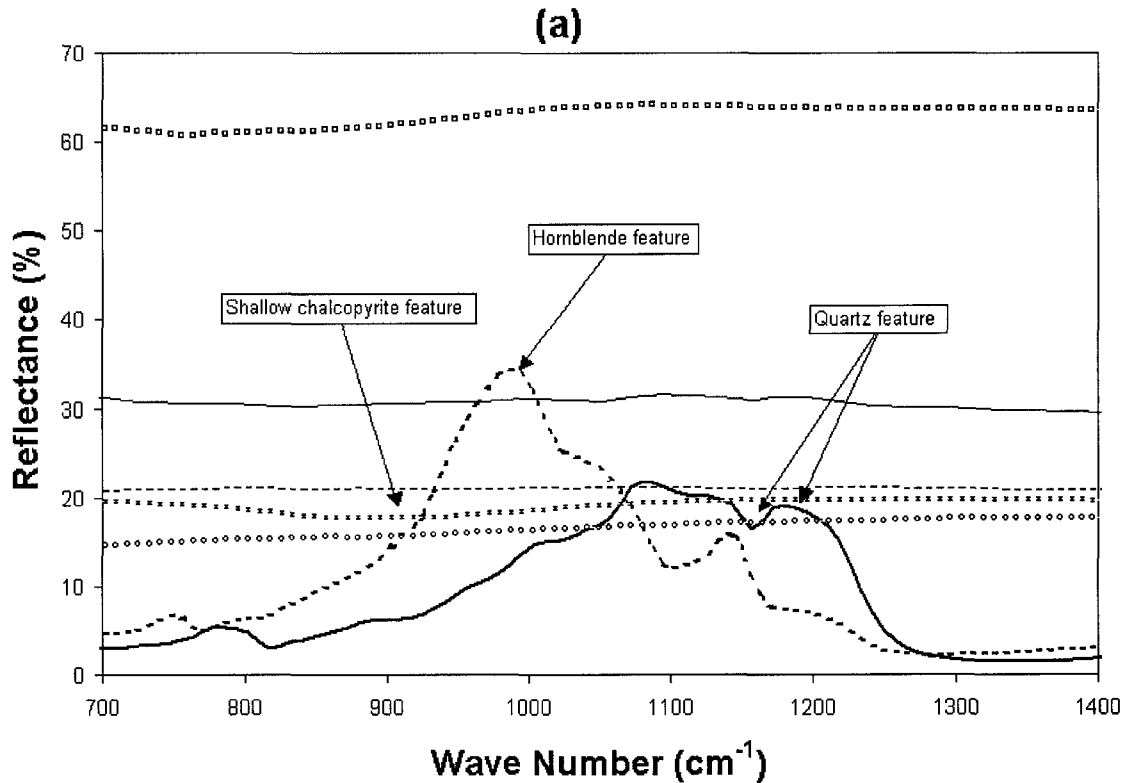


Figure 3.6a Reflectance spectra of sulfide mineral powders and broken rock surfaces. The spectra of sulfide powder (212-600 nm grain size) were measured in bi-directional reflectance mode at RELAB, Brown University. The powders were created from massive sulfide samples of the same Sudbury locality. Bold solid line = Granite sample #30; bold dash line = amphibolite sample #10; thin solid line = massive sulfide sample #9, 26%Cp, 63%PnPp; thin dash line = massive sulfide sample #1, 80%Cp, 15PnPp; stars = chalcopyrite powder spectra; circles = pentlandite powder spectra; black squares = wet/dry ratio spectra of diffuse gold panel.

(b)

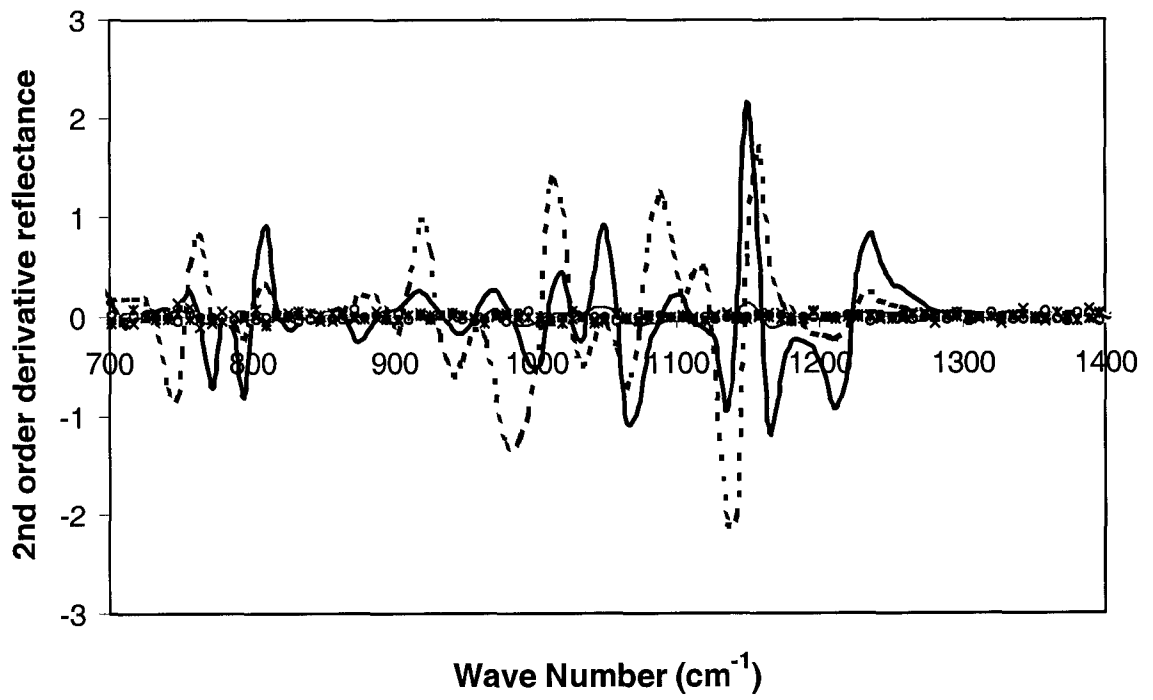


Figure 3.6b 2<sup>nd</sup> order derivatives of the spectra shown in Figure 3.6a. Refer to Figure 3.6a for legends.

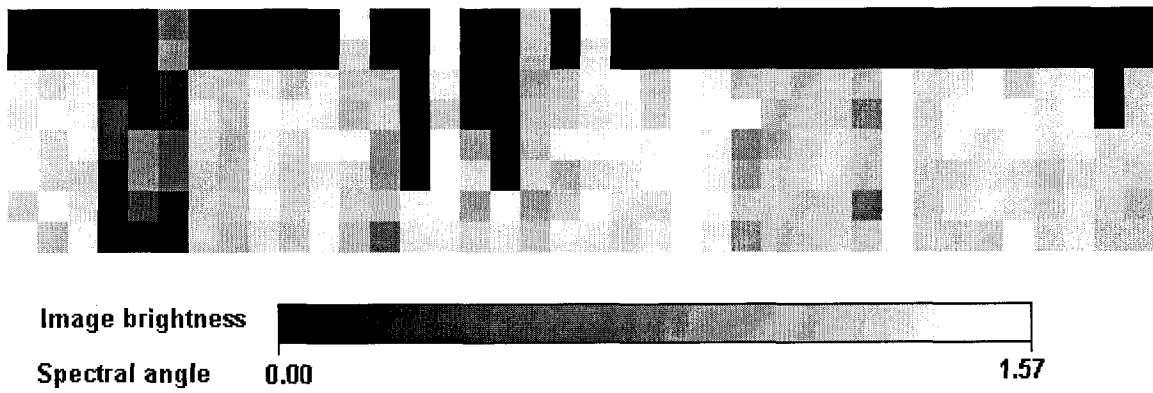


Figure 3.7 Spectral angle (in radian) map for the diabase endmember. Darker spots represent smaller angle values indicating a higher similarity to the diabase endmember spectrum. Refer to Figure 3.8 for the locations of the diabase (DIA) spots.

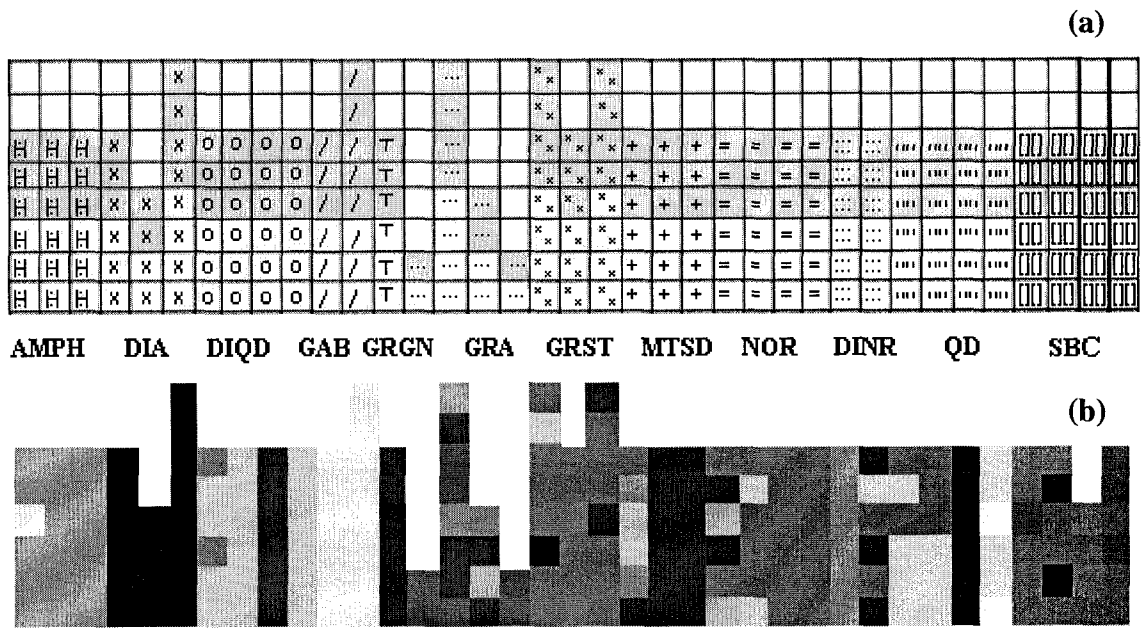


Figure 3.8 Results of the rock type classification. (a) upper: Schematic representation of the image construct. Each square represents one spot/measurement; each column of squares includes all spectral measurements for one sample, and each pattern groups spectra from one rock type. The lighter coloured squares at the bottom of each column correspond to measurements from dry surfaces, while darker shades represent measurements from wet surfaces. There are no spectra in areas occupied by white squares. Rock acronyms are detailed in Table 3.1; (b) lower: Color-coded classification results using SAM applied to the 2<sup>nd</sup> order derivative spectra.



## CHAPTER 4

# ORE DETECTION AND GRADE ESTIMATION IN SUDBURY MINES USING THERMAL INFRARED SPECTROSCOPY

### 4.1 Introduction

Reflectance spectroscopy involves the measurement of light reflected from a solid, liquid or gas at varying wavelengths, for the extraction of compositional information. The variations in material composition often cause shifts in the shape and position of features in the spectrum. With the vast chemical variety typically encountered in the world, spectral signatures can often be complex. However, an increased knowledge of the natural variation of spectral features and a better understanding of the causes of the observed shifts, combined with rapidly improving computing resources, allow us to probe in increasing detail the chemistry of terrestrial materials. By analysing the spectral features, and thus specific chemical bonds in materials, one can map where those bonds occur, and thus map materials. For geological purposes the identity and relative proportions of optically-active minerals can often be deduced from the shape of the reflectance curve. The data might be for a rock measured in the laboratory, in the field or from an aircraft, or of a whole planet from a spacecraft or Earth-based telescope.

Thermal Infrared Reflectance (TIR) spectroscopy generally refers to the traditional mid-infrared (MIR) spectral region, 3.0 to 30  $\mu\text{m}$ . Geological applications of TIR spectroscopy have been conducted for decades. Early research by Lyon (1965, 1972) revealed differences between mineral assemblages or within-mineral groups in rocks from the shape and intensity of the spectra and the presence of individual minima (or maxima). In the laboratory, TIR is measured by shining sufficient thermal energy on a

sample and then measuring its reflectance. Salisbury *et al.*, (1991) presented laboratory spectra for minerals and rocks that demonstrate the systematic absorption troughs and reflection peaks resulting from vibrational motions of bonds within crystalline materials. The TIR spectral features of silicate minerals are related to the vibration of molecules and bonds such as Si-O, Al-O, H-O, and Si-Al-O (Lyon and Burns, 1963; Vincent and Hunt, 1968; Nash and Salisbury, 1991; Wenrich and Christensen, 1996). The strength of absorption/reflection features and their position vary with mineral composition and crystal structure and provide a possible means to determine mineral composition and rock type remotely. TIR hyperspectral sensors (hundreds of wavelengths), mounted in airplanes, have been successfully used to produce mineral maps of the earth's surface, which complement other forms of geological mapping (Kahle *et al.*, 1980; Gillespie *et al.*, 1984; Kahle *et al.*, 1988; Cudahy *et al.*, 1999). The Thermal Emission Spectrometer on board the Mars Global Surveyor planetary probe is currently used for investigating the geological nature of the surface of Mars (Christensen *et al.*, 1998).

A potentially new application of TIR spectroscopy is in the underground mining environment. Numerous forms of geosensing are presently being investigated in support of the automation of routine mine production. One form of geosensing being considered in this study is the delineation of sulfide-rich ore zones from their host rock and the estimation of ore grade using TIR reflectance spectroscopy. There are several key differences, though, in the past use of this technology for mapping and that intended for underground work. First, the intent is to map underground rock faces, which means that a source of illumination must be supplied. The choice of measurement of reflected energy rather than emitted energy is dictated by the difficulty of detecting the emission

properties of the rock surface in an environment which acts as a blackbody cavity at a temperature similar to that of the target of interest (Rivard *et al*, 1995). Second, the rocks exposed will be broken with little or no weathering. Third, the rocks are likely to be wet and water has a very high absorption coefficient in the infrared. Thus even a thin film of water would substantially reduce reflectance, which could make diagnostic absorption features of minerals hard to measure. Finally, the TIR spectral signature of sulfides has not been well documented compared to silicate minerals. There are a few spectra in the literature for pyrite and pyrrhotite (Ferraro, 1982; Salisbury *et al*, 1991), which indicate high reflectance in the TIR with a lack of diagnostic spectral features below 27  $\mu\text{m}$ . No spectra for chalcopyrite have been reported.

Laboratory measurements were undertaken to address these issues using samples of massive and disseminated ores and barren host rocks found in and around the Sudbury Basin, as they would occur when freshly exposed in the underground environment. The intent was to test the feasibility of using TIR geosensing to distinguish ore-bearing rocks from their host, to estimate ore grade under dry and wet conditions, and to elaborate a rationale and the methods to achieve these objectives using reproducible measurements. The more practical aspects of feasibility will be investigated during further studies.

## **4.2 Materials and methods**

### **4.2.1 Sample suite**

A total of twenty-six samples were collected from eight mines around the Sudbury Basin in Ontario. All samples were collected underground except one barren rock sample, which was collected from a surface outcrop. The samples selected had reasonably flat, freshly-broken clean faces, large enough to make non-overlapping

measurements, and displayed a reasonably homogeneous mineralogical texture. The latter point is important because the backside of each sample was cut to generate thin sections, from which modal point counts were extracted and then used to guide the ore grade estimation from the TIR spectra. Two thin sections were examined for the most heterogeneous samples. The samples (Table 4.1) are from two rock types, span a variety of grain sizes, and include massive and disseminated ores. The twenty massive and disseminated ore-bearing samples contain chalcopyrite (Cp), pyrrhotite (Po) and pentlandite (Pn) as the major ore-forming minerals. Pyrite occurs as an accessory phase.

#### **4.2.2 Instrumentation and set-up**

Analyses were carried out using a Bomem MB102 Fourier Transform InfraRed (FTIR) spectrometer equipped with a Mercury/Cadmium/Telluride (MCT) detector. The MCT detector measured reflected thermal energy at wave numbers ranging from 450 to 6000  $\text{cm}^{-1}$  (1.67-22.0  $\mu\text{m}$ ). The light source was a globar. An infra-red camera was used to image the footprint of the light source (not visible to the eye) on the sample. The light source was normally incident to the sample surface, and the viewing angle was at 35 degrees providing a diffuse bidirectional reflectance measurement (Hapke, 1993). Samples were about 50 cm away from the viewing sensor. Reflectance spectra were obtained from the ratio of each measurement to that of an illuminated diffuse gold panel of known reflectance. The data presented in this study includes two sets acquired with the same illumination and viewing geometry. One set is characterized by a field of view of approximately 15 by 15 mm for which three to six measurements per sample were acquired (Table 4.1). The second set is characterized by a smaller field of view of 4 by 4 mm in which case 9 to 20 measurements were acquired. For every location measured,

spectra were collected for dry and wet conditions to simulate extreme underground conditions. Surfaces were wetted using clean water to form a water film. These conditions were ephemeral and required immediate acquisition following wetting of the surface.

### **4.2.3 Experimental work**

#### *Signal to noise and spectral resolution*

Signal to noise (S/N) was adequate, exceeding 1000 (Figure 4.1) over the entire spectral region detected (1.67-22.0  $\mu\text{m}$ ). It was estimated for a single scan while measuring a diffuse gold panel (Infragold<sup>TM</sup>), a target of high and uniform reflectance. When measuring samples, 200 scans were averaged whenever possible to suppress noise, but a subset of the samples were measured using an average of 8 scans because of time constraints. This difference had little impact on the quality of the data in view of the high S/N of the instrument.

The MB102 FTIR provides selectable spectral resolution. Use of coarser resolution results in quicker acquisition. The diffuse gold panel was measured at a resolution of 1  $\text{cm}^{-1}$ , 2  $\text{cm}^{-1}$ , 4  $\text{cm}^{-1}$ , 8  $\text{cm}^{-1}$ , 16  $\text{cm}^{-1}$ , 32  $\text{cm}^{-1}$  and 64  $\text{cm}^{-1}$  using 200 scans to determine an adequate resolution for this study. A set-up at 16  $\text{cm}^{-1}$  was selected for all sample measurements because it preserves known TIR spectral features.

#### *Reproducibility*

Four targets (fine-grained, coarse-grained, homogeneous and most heterogeneous) were used to assess measurement reproducibility (Table 4.2). Eight consecutive measurements were acquired for a given location on each sample within a time interval of eight minutes. Each measurement was an average of 200 scans at 16  $\text{cm}^{-1}$  spectral

resolution. The root mean square (RMS) error over the entire region is between 0.15-2.01 % reflectance, absolute, with a mean value of 0.70 % (Figure 4.2). The error increases above 1.00 % beyond 4000  $\text{cm}^{-1}$  (near-infrared region) due to the sensitivity fall off of the detector. These results indicate that the FTIR was very stable within the thirty-two minutes required for the acquisition of thirty-two measurements from four samples. Consequently measurement of the gold panel, required for the estimation of reflectance, was conducted approximately every thirty minutes.

### **4.3 Results and discussion**

#### **4.3.1 Spectral statistics**

In some samples, the sulfides occur as blebs or aggregates, which can vary in grain size and which are not always uniformly distributed. Such textural and compositional heterogeneity is difficult to sample adequately, either for mineralogy with a few thin sections, or for reflectance with limited spectral measurements. The latter issue was of particular concern for samples sp50-59, which were examined with a small field of view (4x4 mm).

We conducted an expectation test (Richard, 1979) for the 1319  $\text{cm}^{-1}$  spectral range to assess if a sufficient number of measurements had been acquired to adequately represent the overall reflectance of each sample. In this test, an adequate number of measurements is judged to have been taken when the average reflectance approaches a constant value as more measurements are included (Figures 4.3-4.6). The test was run for samples sp50-59 and all passed the test whether wet or dry.

#### **4.3.2 Spectral characteristics of ores and silicate-rich rocks**

Figure 4.7 displays two representative spectra of typical host rocks for the ore (sp17

norite, sp33 quartz-diorite) and two spectra of massive sulfide (total sulfide abundance  $\geq$  90%). These show spectral features between 700 – 1300  $\text{cm}^{-1}$  and 2000 – 3300  $\text{cm}^{-1}$  where silicate minerals (quartz, feldspar, hornblende, biotite, etc.) play an important control on the overall shape and magnitude of rock reflectance spectra. The spectral features include pronounced reflection peaks (Reststrahlen Bands), which can be diagnostic of specific minerals (e.g., 1180  $\text{cm}^{-1}$  reflectance peak of quartz) (Salisbury *et al*, 1991; Salisbury, 1993). There is a shift toward smaller wave numbers (longer wavelengths) in the Christensen Frequency, represented by a local minima around 1300  $\text{cm}^{-1}$ , and reflectance peaks as the sample composition changes from quartz-rich (felsic) to quartz-poor (mafic) (Vincent *et al*, 1975; Nash and Salisbury, 1991).

Sulfide minerals (chalcopyrite, pyrrhotite, pentlandite) do not show diagnostic features in these two spectral regions (Figure 4.7) and display generally flat spectra. The massive sulfides display distinctly higher reflectance over the entire thermal region (average reflectance  $>20\%$ ) while the silicate rocks show low reflectance (average reflectance  $< 10\%$ ). The largest difference in reflectance between massive sulfides and silicate rich rocks is observed in the 1300 – 1400  $\text{cm}^{-1}$  spectral region, located just beyond the Reststrahlen band (700-1300  $\text{cm}^{-1}$ ) of silicate minerals. In this region the spectra of silicate minerals converge to a common low reflectance value related to the Christiansen frequency.

Solving for the abundance of sulfides would require modeling silicate-sulfide mineral mixtures and an explicit knowledge of the spectra for all mineral constituents of the rocks, a task difficult to complete in many field measurement scenarios. An important finding of this research is that in the 1300 – 1400  $\text{cm}^{-1}$  region, most known silicate

minerals converge to a common reflectance minima of less than 1.5%, eliminating the requirement for the spectra of each silicate mineral constituent. Moreover, because silicates do not contribute significantly to reflectance in this region, it is possible to relate the spectra from silicate-sulfide mixtures directly to sulfide concentration. This information was used to develop a method for the estimation of ore abundance.

#### **4.3.3 Identification of ore-bearing rocks**

The first step in developing a method for identifying ore-bearing rocks was to address issues related to the geometry of the spectral measurements. Many common geological surfaces exhibit only quasi-Lambertian behaviour when viewed at nadir for incidence angles up to 40° (Mustard and Sunshine, 1999). In addition, illumination intensity is affected by the angle of a surface. Thus the magnitude of the reflectance spectra (albedo), though not the shape, will be affected by small variations in the geometry of observation and illumination induced by irregularities of the surface. The problem is especially acute when using naturally-broken rock faces. Continuum removal can be used to remove the albedo effect by normalizing the reflectance curves by ratioing them to the convex hull fitted over the spectrum (Clark and Roush, 1984). After continuum removal for a wide spectral range (Figure 4.8), the spectra show a systematic increase of the continuum removed reflectance (CRR) in the 1300-1400  $\text{cm}^{-1}$  region with an increase of total sulfide content in the samples. The correction does not remove any wavelength dependent anisotropy resulting from small variations in the geometry of observation and illumination induced by irregularities of the surface. These variations are embedded in the uncertainty of our results. The magnitude of wavelength dependent anisotropy has been investigated for soils (Becker *et al*, 1985; Nerry *et al*, 1991; Narayanan *et al*, 1992;



Kologo and Stoll, 1996) but has not yet been assessed for the broken surfaces of this study.

The presence of water on the Infragold panel introduces structure to the spectra of a wet surface (Figure 4.7). Similarly, when sulfide samples with flat spectra are wetted, new spectral features are introduced. For continuum removal over large spectral regions (e.g., 500-5000  $\text{cm}^{-1}$ ), these water features significantly affect the CRR near 1300  $\text{cm}^{-1}$ . However, between 1080-1504  $\text{cm}^{-1}$  the spectra of water on Infragold<sup>TM</sup> is featureless or flat, i.e. water simply makes reflectance lower. Consequently, continuum removal over this limited spectral range should be relatively insensitive to the presence of water and should facilitate the identification of ore whether the surface is dry or wet.

Using the CRR at 1319  $\text{cm}^{-1}$  for all samples with 15x15 mm FOV, an artificial image was constructed to visualise the results of the spectral analysis (Figure 4.9). The massive sulfide samples and samples with more than approximately 20% sulfides exhibit higher TIR reflectance at 1319  $\text{cm}^{-1}$  compared with samples of the barren host rocks. In contrast, samples sp26 and sp13, which have less than 20% sulfides, are more difficult to separate from the host rocks (Figure 4.9b). Measurements of wet ores (>20% sulfides), whether massive or disseminated, are also distinctively bright. Thus it appears that the CRR at 1319  $\text{cm}^{-1}$  when calculated from 1080-1504  $\text{cm}^{-1}$  is relatively insensitive to the presence of liquid water.

To mask the barren samples, a threshold at 0.475 CRR was applied to Figure 4.9b, resulting in an image, which shows a large subset of the ore occurrences (Figure 4.9c). Table 4.3 documents the percentage of ore-bearing pixels successfully identified for each sample and shows that correctness is greater than 83% for samples exceeding 20% total

sulfides. Correctness systematically increases with increasing sulfide concentration. This tool would be useful to assess the location of high sulfide wall rock (>20% ore) in an underground environment.

#### **4.3.4 Correlation between reflectance and sulfide concentration**

The variation in CRR value at  $1319\text{ cm}^{-1}$  as a function of sulfide concentration (Figures 4.10-4.12) was examined empirically. In addition to the 20 sulfide-bearing samples, two data points were included, one for barren norite and one for barren quartz diorite. These points are the average CRR value for the three samples of each rock type. The points were included to add a constraint to the regression in the absence of data with sulfide concentrations between 0 and 7%.

The regression between the CRR value and sulfide concentration gives a coefficient of determination value ( $R^2$ ) of 0.93 for both the dry (Figure 4.10) and wet (Figure 4.11) measurements. In fact, the form of the dry and wet regression equations is so similar that it suggests that the data could be pooled with little loss in prediction accuracy or precision. This was achieved by averaging all wet and dry measurements for a sample, and then fitting a new regression through the wet-dry average data (Figure 4.12). The regression line for the wet-dry average also has an  $R^2$  value of 0.93. The regression line reaches 0% sulfide (i.e. crosses the x-axis) at a CRR value of 0.02, which is close to the lowest CRR value (0.06) observed from barren samples. More than 85% of the residuals (observed minus predicted) are within 10% absolute of the true total sulfide concentration (Figure 4.13). Because of the shape of the equation, errors in CRR measurements would induce larger absolute errors at high concentrations of sulfides than low.

The total sulfide concentration for each sample was estimated from a single thin

section. Since a thin section is unlikely to perfectly represent the face of the rock, especially for blebby heterogeneous disseminated sulphides, we expected that the relationship might appear quite noisy. In addition, grain size is variable for all minerals in the sample suite, and the sulfides occur in clusters, further increasing the range in effective grain size. Grain size is known to affect reflectance properties (Salisbury and Eastes, 1985). Yet the regression is excellent, suggesting that the method is robust. The finding that a single regression equation can be used for either wet or dry samples, further enhances the potential of the approach.

The relationship demonstrates the capability to estimate total sulfide concentration using TIR reflectance data. However, not all sulfide minerals contain metals such as nickel or copper, and minerals such as pyrrhotite do not contribute to the true grade of ore. The TIR approach described here is not capable of differentiating between types of sulfide minerals. In some cases, this is not problematic because the true ore minerals form a fairly constant proportion of the total sulfide content. In other situations, some method to estimate the mineral mix would be advantageous. A parallel study using visible and shortwave-infrared wavelengths has shown that it is possible to differentiate between chalcopyrite vs pentlandite and pyrrhotite if the concentration of total sulfides is known (Gallie *et al*, 2000). Thus, use of the two wavelength ranges together holds significant potential for development of a useful and practical ore grading system for the operational mining environment.

#### **4.4 Conclusions**

This study focused on the use of thermal infrared reflectance spectroscopy for the discrimination of sulfide-bearing rock from barren host rocks, and ore grade estimation.

Wet and dry rock/ore samples were measured for the analysis of their spectral characteristics. The following are key findings for this research:

- In the region of  $1319\text{ cm}^{-1}$ , near the Christiansen Frequency, most known silicate minerals converge to a common reflectance minima (less than 1.5%) but massive and disseminated sulfide ores have distinctly higher reflectance.
- When sulfides are disseminated in the host rock, the average reflectance of the rock increases but the correlation with abundance is not systematic due to surface geometry effects. When this is overcome by using continuum removal, the correlation between the continuum removed reflectance (CRR) at  $1319\text{ cm}^{-1}$  versus sulfide concentration gives an  $R^2$  value of 0.93 for dry and wet surfaces when averaged.
- More than 80% of the residuals (observed minus predicted) are within 10% total sulfide, absolute.
- A simple threshold applied to the CRR at  $1319\text{ cm}^{-1}$  to separate ore-bearing samples from barren host rocks is very effective for sulfide concentrations exceeding 20%.

Different ore forming minerals (chalcopyrite, pentlandite, etc.) were not identified using TIR reflectance spectroscopy because discriminating features are absent in the portion of the spectrum investigated. However, the use of shorter wavelengths, in combination with TIR, may hold the potential both to estimate total sulfides and to provide a breakdown of the mineral mix.

## **Acknowledgements**

The project was jointly funded by Inco Ltd and the European Space Agency (ESA), Harsh Environments Initiative. Access to a MB102 FTIR was provided by Bomem Inc. The assistance of Brian Thompson, Greg Greenough and Wayne Garland, all from Inco Ltd, was invaluable in obtaining and identifying the samples.

## **REFERENCES**

- Becker, F., Ramanantsizehena, P. and Stoll, M.P, 1985, Angular variation of the bi-directional reflectance of bare soils in the thermal infrared band. *Appl. Opt.*, **24**, 365-375.
- Christensen, P. R. , Anderson, D. L., Chase, S. C., Clancy, R. T., Clark, R. N. , Conrath, B. J., Kieffer, H. H., Kuzmin, R. O., Malin, M. C., Pearl, J. C. , Roush, T. L. and Smith, M. D., 1998, Results from the Mars Global Surveyor Thermal Emission Spectrometer. *Science*, **279**, 1692-1698.
- Clark, R.N. and Roush, T.L., 1984, Reflectance spectroscopy: Quantitative analysis techniques for remote sensing applications. *J. Geophys. Res.*, **89**, No B7, 6329-6340.
- Cudahy, T.J., Whitbourn, L.B., Connor, P.M., Mason, P. and Phillips, R.N. 1999, Mapping surface mineralogy and scattering behavior using backscattered reflectance from a hyperspectral midinfrared airborne CO<sub>2</sub> laser system (MIRACO<sub>2</sub>LAS). *IEEE Trans. Geosci. Remote Sensing*, **37**, 2019-2034.
- Ferraro, J.R., 1982, *The Stadler infrared handbook of minerals and clays*. Stadler Research Laboratories, Philadelphia, 476 p.
- Gallie, A., McArdle, S., Rivard, B. and Francis, H., 2000, Estimating sulfide ore grade in

- broken rock using visible/infrared hyperspectral reflectance spectra. Submitted to Remote Sens. of Environm.
- Gillespie, A.R., Kahle, A.B. and Palluconi, F.D., 1984, Mapping alluvial fans in death Valley, California, using multichannel thermal infrared images. *J. Geophys. Res.* , **11**, 1152-1156.
- Hapke, B. 1993, Theory of reflectance and emittance spectroscopy in Arvidson, R., and Rycroft, M. J., Eds., Topics in remote sensing, Cambridge University Press.
- Kahle, A.B., Gillespie, E.A., Abbott, M.J., Walker, R.E. and Hoover, G., 1988, Relative dating of Hawaiian lava flows using multispectral thermal infrared images: a new tool for geologic mapping of young volcanic terranes. *J. Geophys. Res.*, **93**, 15239-15251.
- Kahle, A.B., Madura, D.P. and Soha, J.M., 1980, Middle infrared multispectral aircraft scanner data: analysis for geological applications. *Appl. Opt.*, **19**, 2279-2290.
- Kologo, N., and Stoll, M., 1996, CO<sub>2</sub> laser light scattering by bare soils for emissivity measurements: absolute calibration and correlation with backscattering and composition. *IEEE Trans. Geosc. Remote Sensing*, **34**, 936-945.
- Lyon, R.J.P., 1965, Analysis of rocks by spectral infrared emission (8-25  $\mu$ m). *Econ. Geol.*, **60**, 715-736.
- Lyon, R.J.P., 1972, Infrared spectral emittance in geology mapping: Airborne spectrometer data from Pisgash Crater, Calif. *Sciences*, **175**, 983-986.
- Lyon, R.J.P. and Burns, E.A., 1963, Analysis of rocks and minerals by reflected infrared radiation. *Econ. Geol.*, **58**, 274-284.
- Mustard, J. and Sunshine, J. 1999, Spectral analysis for earth science investigations using

- remote sensing data, Chapter 5, *in* Rencz, A., Ed., *Manual of Remote Sensing: Remote sensing for the earth sciences*, Third edition, Vol. 3: John Wiley and Sons.
- Naranayan, R., Green, S.E. and Alexander, D.R., 1992, Mid-infrared backscatter characteristics of various benchmark soils. *IEEE Trans. Geosc. Remote Sensing*, **30**, 516-529.
- Nash, D.B. and Salisbury, J.W., 1991, Infrared reflectance spectra of plagioclase feldspar. *J. Geophys. Res.*, **18**, 1151-1154.
- Nerry, F., Stoll, M.P. and Kologo, N., 1991, Scattering of a CO<sub>2</sub> laser beam at 10.6  $\mu\text{m}$  by bare soils: experimental study of the polarized bi-directional scattering coefficient; model and comparison with directional emissivity measurements. *Appl. Opt.*, **30**, 3984-3995.
- Richard, A.G., 1979, *An introduction to probability and statistics using BASIC*, Marcel Dekker INC.
- Rivard, B., Thomas, P. and Giroux, J., 1995. Precise emissivity of rock samples. *Remote Sens. of Environ.* **54**, 161-167.
- Salisbury, J.W., 1993, Thermal infrared (2.5-13.5  $\mu\text{m}$ ) spectroscopy: Laboratory data, Chapter 4, *in* Pieters, C., and Englert, P., Eds., *Remote Geochemical Analysis: Elemental and Mineralogical Composition*, Cambridge University Press.
- Salisbury, J.W. and Eastes, J.W., 1985, The effect of particle size and porosity on spectral contrast in the mid-infrared. *Icarus*, **64**, 586-588.
- Salisbury, J.W., Walter, L.S., Vergo, N. and D'Aria, D.M., 1991, *Infrared (2.1-25  $\mu\text{m}$ ) spectra of minerals*, Johns Hopkins University Press.

Vincent, R.K. and Hunt, G.R., 1968, Infrared reflectance from mat surfaces. *Appl. Opt.*, **7**, 53-59.

Vincent, R.K., Rowan, L.C., Gillespie, R.E. and Knapp, C., 1975, Thermal infrared spectra and chemical analysis of 26 igneous rock samples. *Remote Sens.of Environ.*, **4**, 199-209.

Wenrick, M. L., and Christensen, P. R., 1996, Optical constants of minerals derived from emission spectroscopy: application to quartz. *J. Geophys. Res.*, **101**, 15921-15931.



Table 4.1 List of rock samples

Rock type	Sample #	Measured area (mm)	# scans <sup>d</sup>	# Dry <sup>e</sup>	# Wet <sup>e</sup>	% Cp <sup>f</sup>	% Po <sup>f</sup>	% Pn <sup>f</sup>	% Total sulfide
Norite	3	15x15	200	3	3	--	--	--	--
	17	15x15	200	3	3	--	--	--	--
	24	15x15	200	3	3	--	--	--	--
Quartz Diorite	6	15x15	200	3	3	--	--	--	--
	7	15x15	200	6	6	--	--	--	--
	33	15x15	200	3	3	--	--	--	--
DINR <sup>a</sup>	13	15x15	200	3	3	0	8	1	9
	23	15x15	200	3	3	0	21	4	25
DIQD <sup>b</sup>	2	15x15	200	3	3	3	27	5	35
	4	15x15	200	3	3	12	6	2	20
	26	15x15	200	3	3	2	9	2	13
	27	15x15	200	3	3	2	19	2	23
	50	4x4	8	15	15	6	8	1	15
	51	4x4	8	15	15	1	5	1	7
	52	4x4	8	15	15	6	8	1	15
	53	4x4	8	18	18	2	15	3	20
	54	4x4	8	24	24	1	7	3	11
	55	4x4	8	15	15	10	2	1	13
	56	4x4	8	9	9	2	9	1	12
	57	4x4	8	12	12	1	5	1	7
	58	4x4	8	15	15	4	12	2	18
	59	4x4	8	15	15	1	11	3	15
MASU <sup>c</sup>	1	15x15	200	3	3	80	10	5	95
	8	15x15	200	4	4	4	44	7	55
	9	15x15	200	3	3	27	41	22	90
	14	15x15	200	3	3	0	68	22	90

<sup>a</sup>Disseminated in Norite; <sup>b</sup>Disseminated in Quartz Diorite; <sup>c</sup>Massive Sulfide; <sup>d</sup> # of individual scans for each measurement; <sup>e</sup> # of individual dry/wet measurements on each sample; <sup>f</sup>from thin section point counts where Cp = chalcopyrite, Po = pyrrhotite, and Pn = pentlandite.

Table 4.2 List of samples used to assess reproducibility

<b>Property</b>	<b>Target type</b>	<b>Sample #</b>
Homogeneous	Infragold™ standard panel	--
Coarse-grained	Granite	18
Homogeneous	Quartz Diorite	33
Heterogeneous	Disseminated in Norite	23 (40% Ore blebs)

Table 4.3 Correctly identified ore-bearing samples at 1319cm<sup>-1</sup> using CRR values.

Sample	Rock type	Dry CRR	Wet CRR	AVG CCR*	% Total Sulfide	Correctness**
Sp1	MASU	0.996	0.995	0.995	95	100%
Sp9	MASU	0.944	0.938	0.941	90	100%
Sp14	MASU	0.985	0.993	0.989	90	100%
Sp8	MASU	0.980	0.987	0.984	55	100%
Sp2	DIQD	0.744	0.792	0.769	35	100%
Sp23	DINR	0.754	0.837	0.796	25	100%
Sp27	DIQD	0.473	0.658	0.567	23	83%
Sp4	DIQD	0.461	0.543	0.503	20	50%
Sp26	DIQD	0.208	0.422	0.317	13	17%
Sp13	DINR	0.348	0.697	0.526	9	50%

\*AVG CRR = Dry CRR/2.0 + Wet CRR/2.0. \*\* Correctness is calculated by counting the percentage of dry and wet measurements above the threshold CRR value.

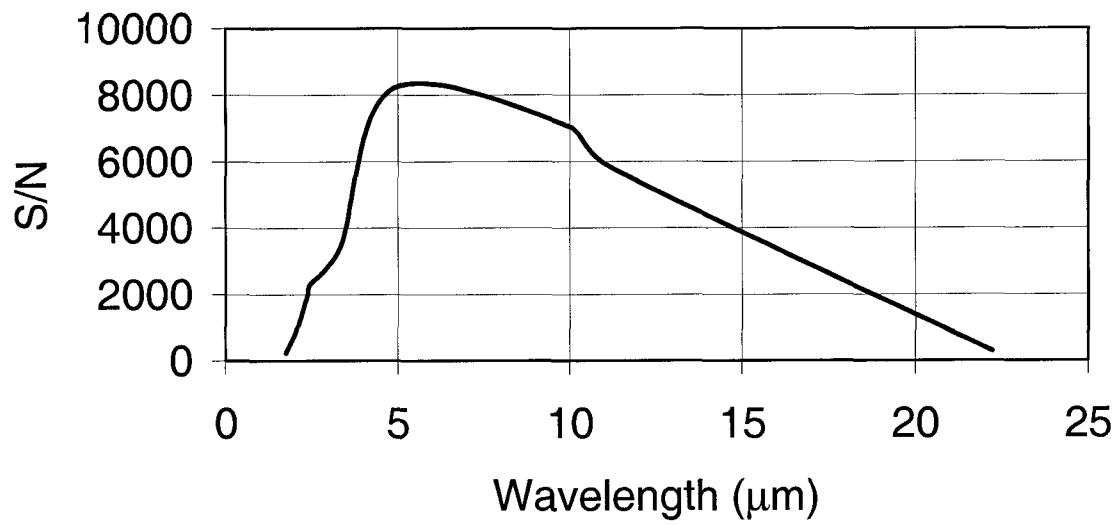


Figure 4.1 Averaged single scan signal-to-noise ratio (S/N) measured over five days using the MB102 FTIR and a 100% reflectance Infragold panel and globar illumination.

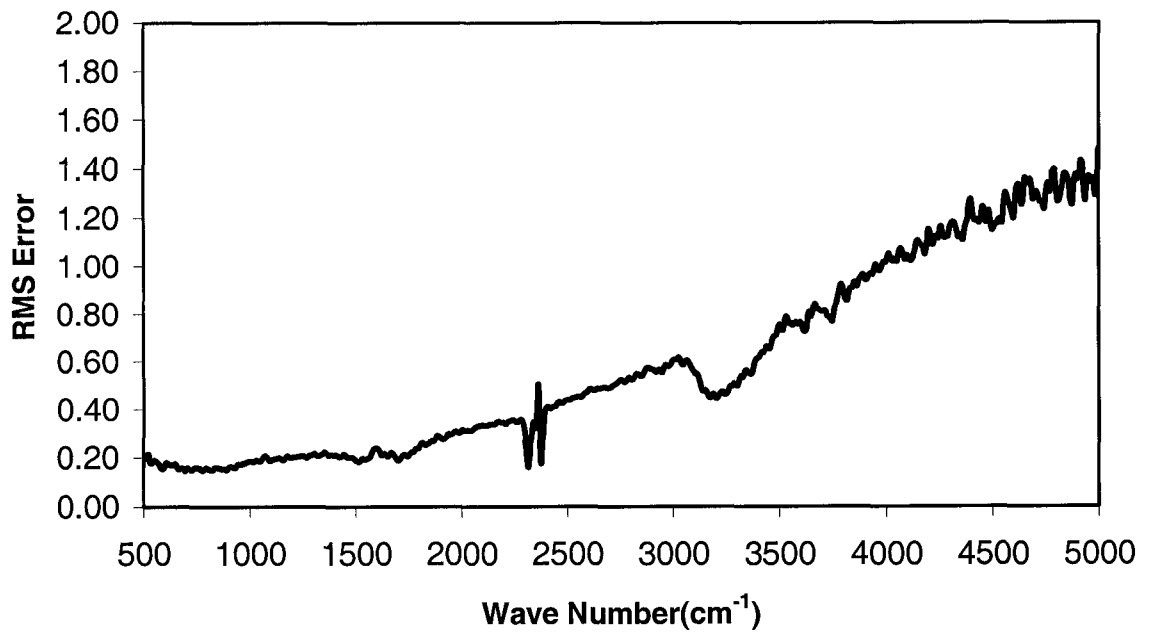


Figure 4.2 RMS error in % reflectance averaged for 32 measurements from four samples during the reproducibility test.

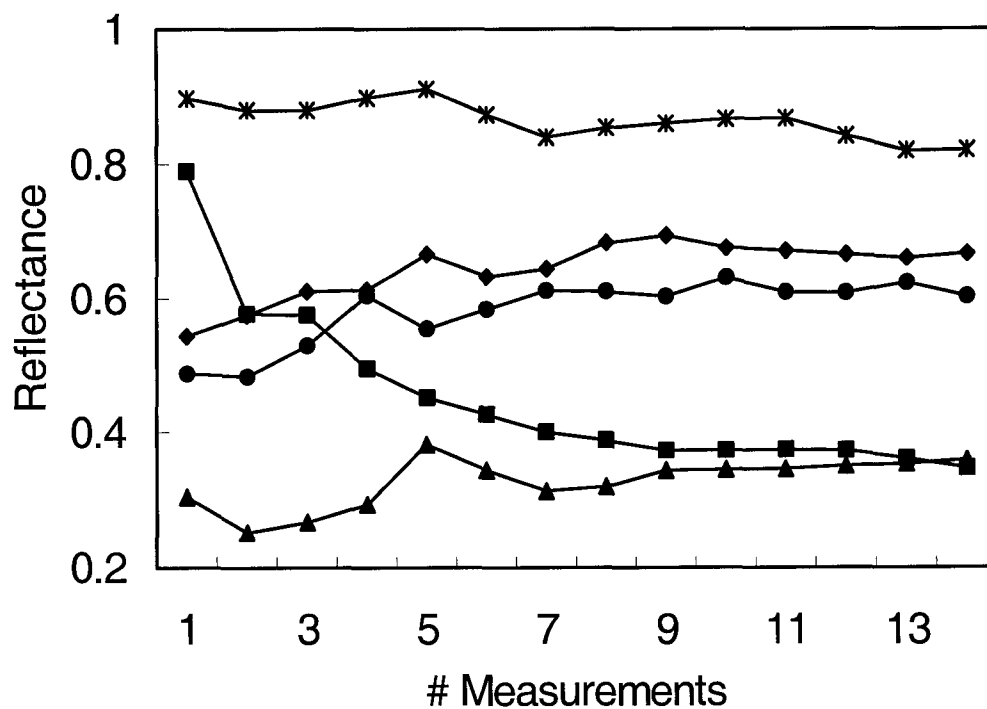


Figure 4.3 Average reflectance at  $1319\text{ cm}^{-1}$  for dry locations of sp50 (diamonds), 51 (squares), 52 (triangles), 55 (circles), and 59 (stars) as a function of the number of measurements for these samples. Results show that these samples exhibit a stabilized average at the end of the experiment. All results shown are for samples with measurement areas of  $4 \times 4\text{ mm}$ .

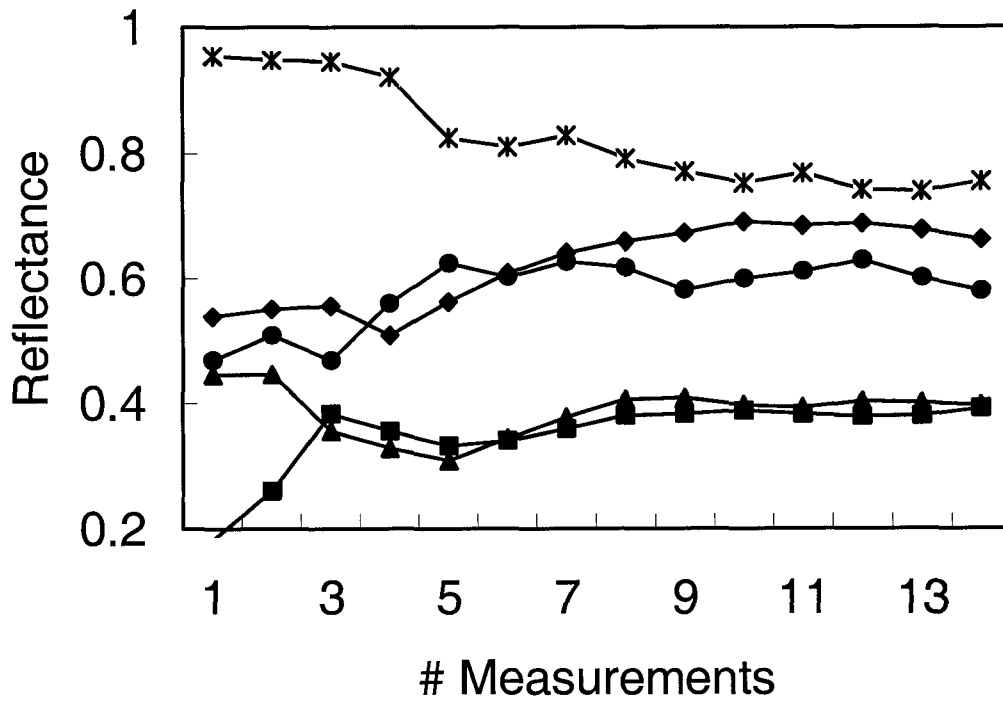


Figure 4.4 Average reflectance at  $1319\text{ cm}^{-1}$  for wet locations of sp50, 51, 52, 55, and 59 as a function of the number of measurements for a these sample. Results show that these samples exhibit a stabilized average at the end of the experiment. Symbols as shown on Figure 4.3.

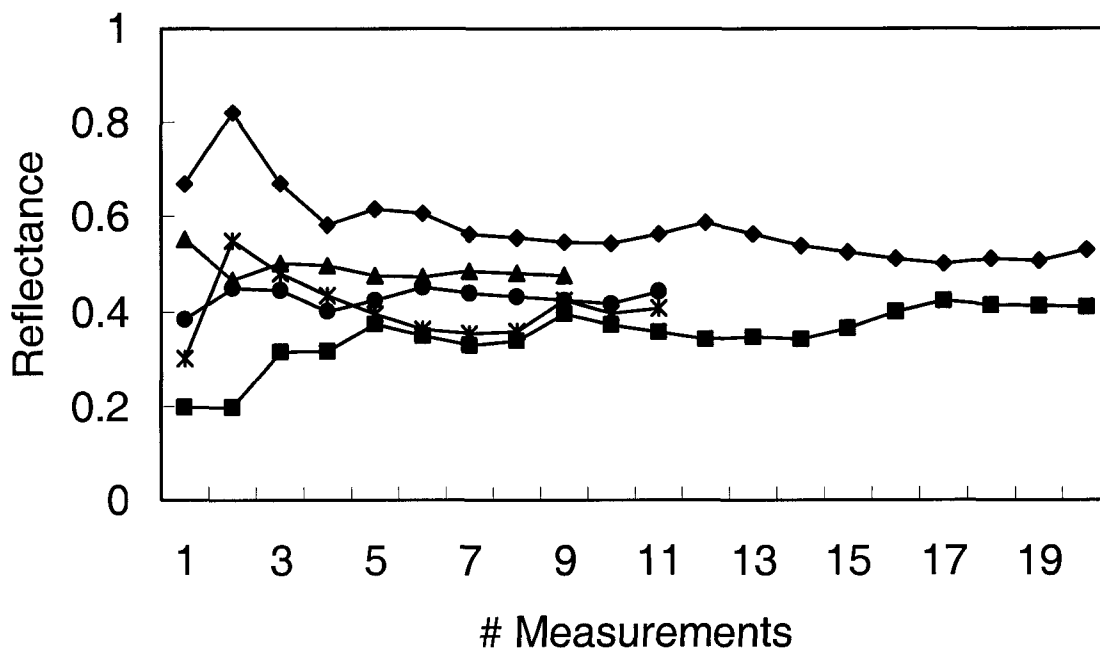


Figure 4.5 Average reflectance at  $1319\text{ cm}^{-1}$  for dry locations of sp53 (diamonds), 54 (squares), 56 (triangles), 57(circles), and 58(stars) as a function of the number of measurements for a these sample. Results show that these samples exhibit a stabilized average at the end of the experiment.



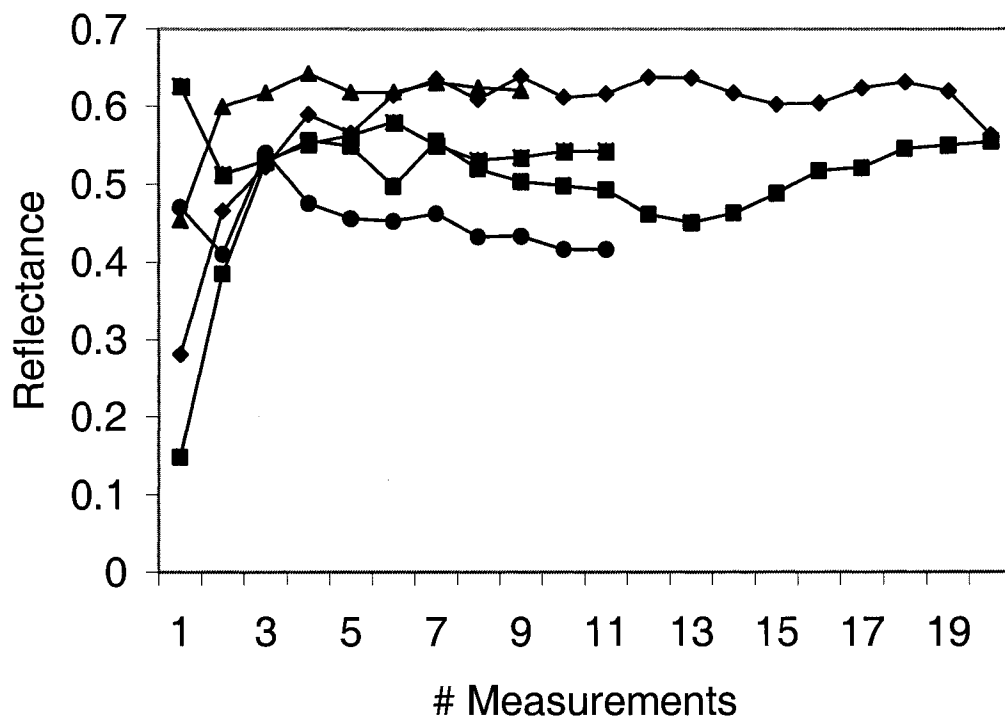


Figure 4.6 Average reflectance at  $1319\text{ cm}^{-1}$  for wet locations of sp53, 54, 56, 57, and 58 as a function of the number of measurements for a these sample. Results show that these samples exhibit a stabilized average at the end of the experiment. Symbols as shown on Figure 4.5.

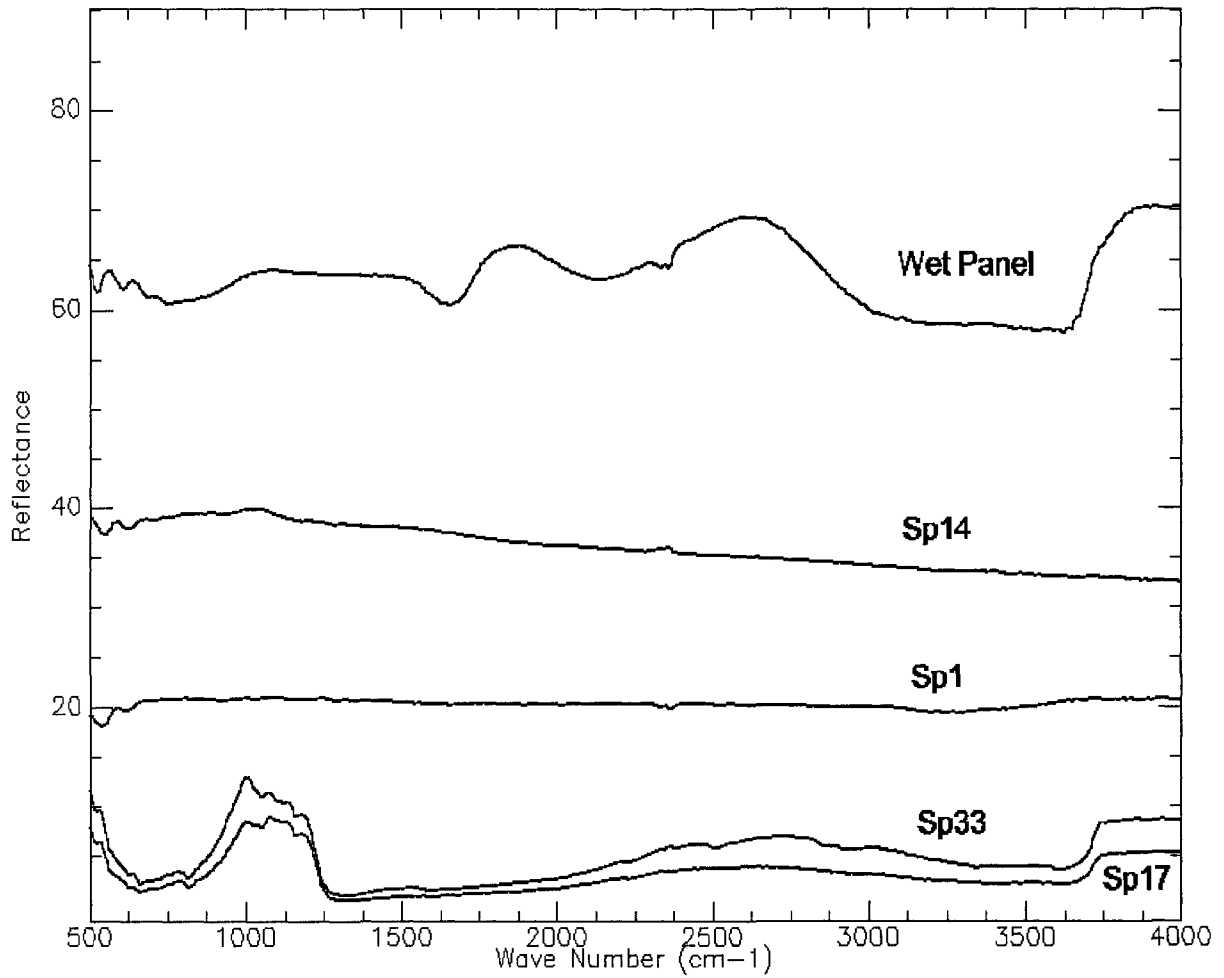


Figure 4.7 Comparison of spectra for typical dry ore-free rocks (sp33, sp17) and massive sulfides (sp1, sp14). The spectra labeled "wet panel" was acquired for the wetted Infragold panel. (By definition, the dry Infragold panel has a perfectly flat spectra with a reflectance of 100%.)

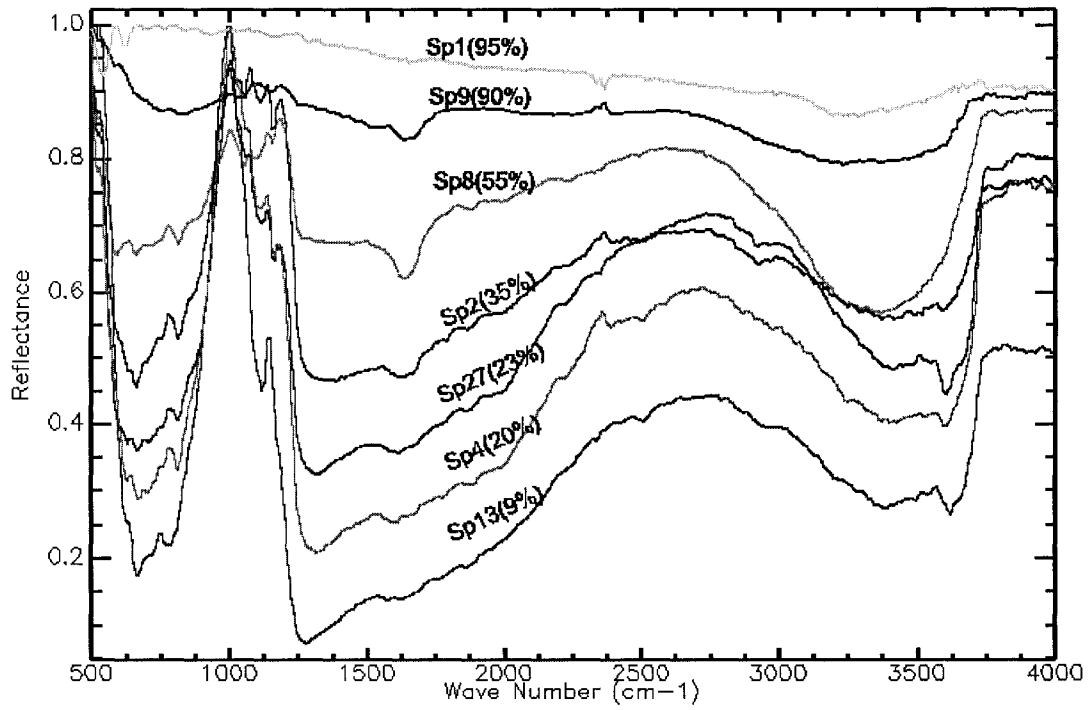


Figure 4.8 Continuum removed reflectance spectra of single measurements of dry, ore-bearing samples. The total sulfide % is shown in parenthesis for each sample. The continuum was calculated for the 500-4000  $\text{cm}^{-1}$  spectral range.

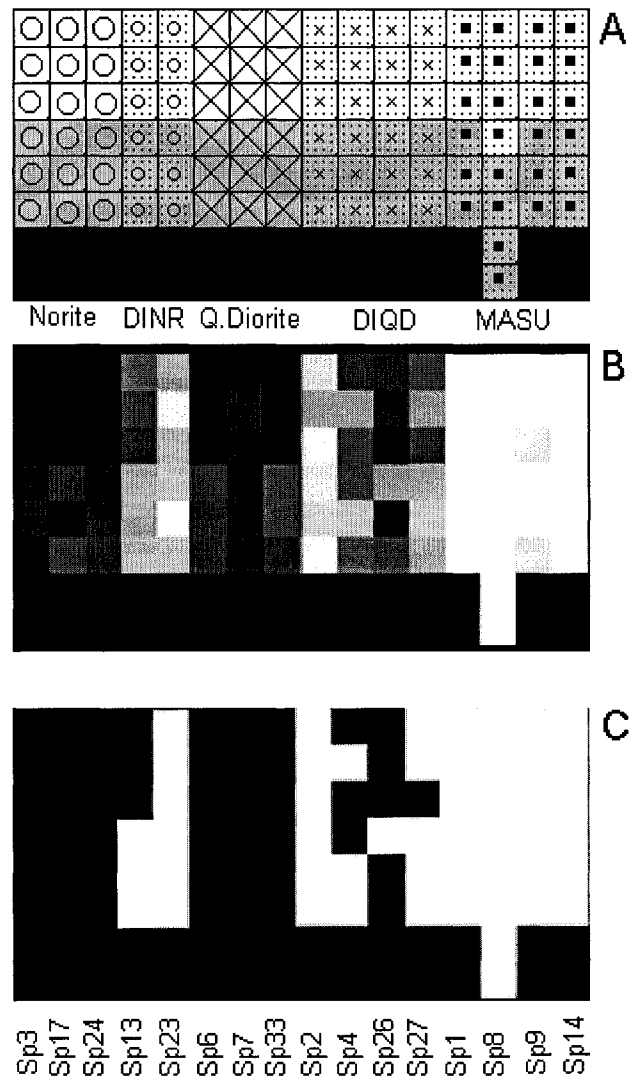


Figure 4.9 (a) Schematic representation of the artificial images displayed in b and c. Each square represents one spectral measurement, each column of squares includes all spectral measurements for one sample, and each pattern groups spectra from one rock type. The lighter coloured squares at the top of each column correspond to measurements from dry surfaces, while darker shades represent measurements from wet surfaces. There are no spectra in areas occupied by black squares; (b) continuum removed reflectance at  $1319\text{cm}^{-1}$  calculated from  $1080\text{-}1504\text{ cm}^{-1}$ ; (c) image shown in b with a threshold corresponding to  $>20\%$  total sulfide concentration.

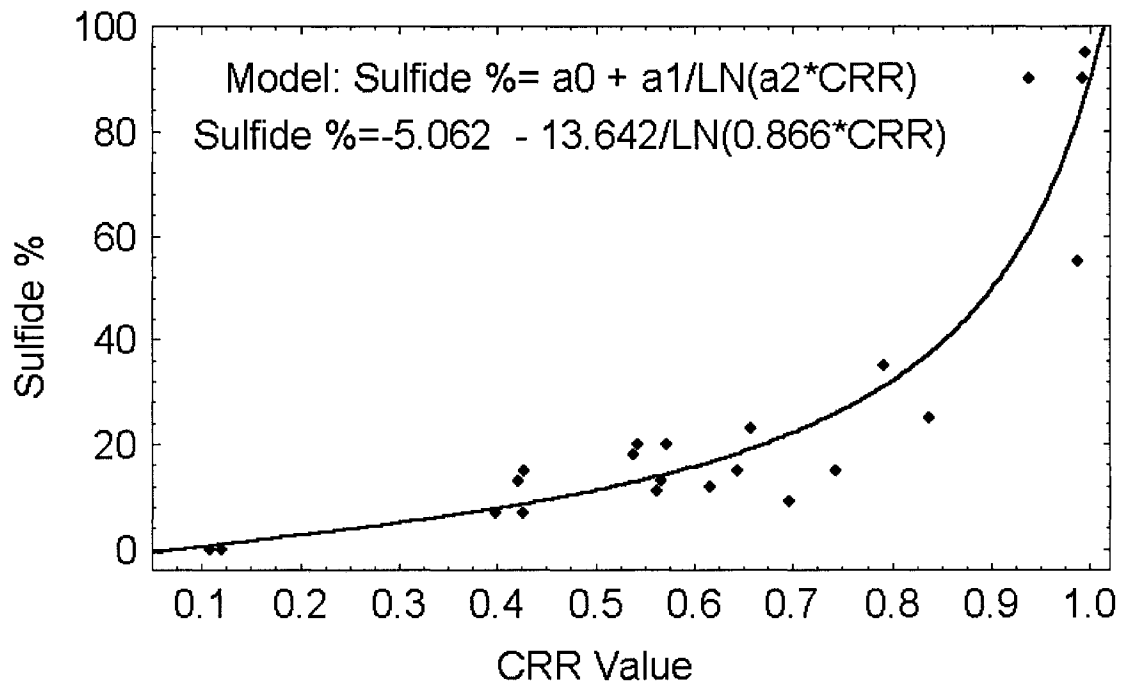


Figure 4.10 Regression between total sulfide and CRR values at 1319  $\text{cm}^{-1}$  for the average of dry locations for a given sample. Continuum removal was carried out from 1080-1504  $\text{cm}^{-1}$ . Total sulfide concentration was estimated via thin section point counting.

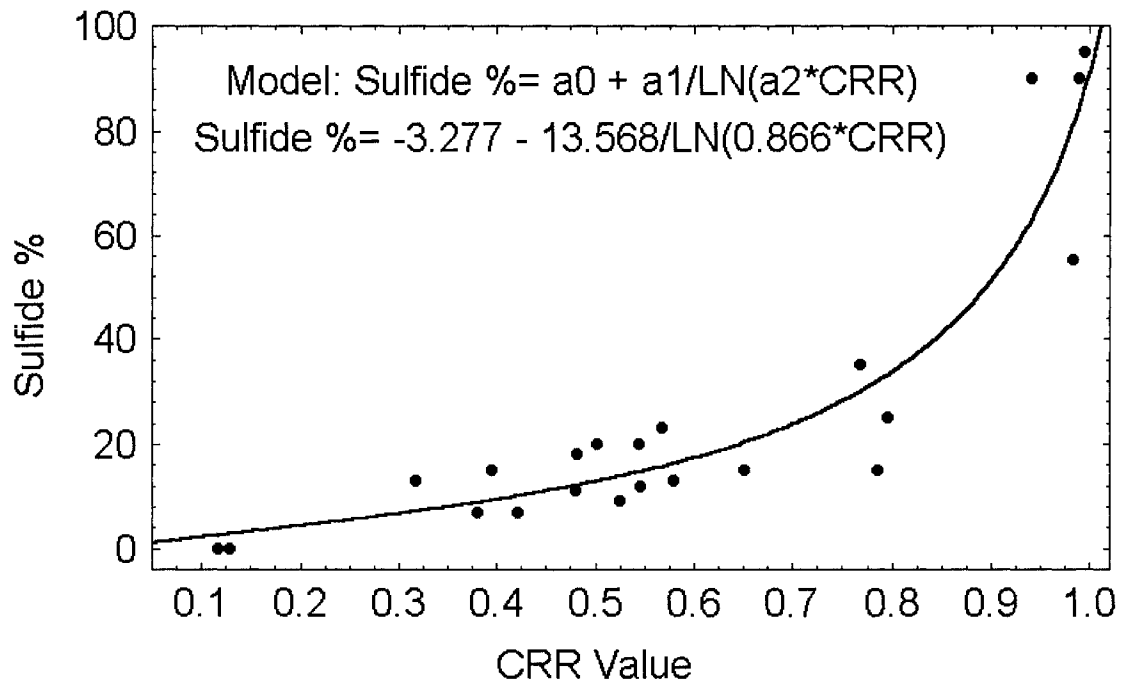


Figure 4.11 Regression between total sulfide and CRR values at 1319 cm<sup>-1</sup> for the average of wet locations for a given sample. See Figure 4.10 for additional details.

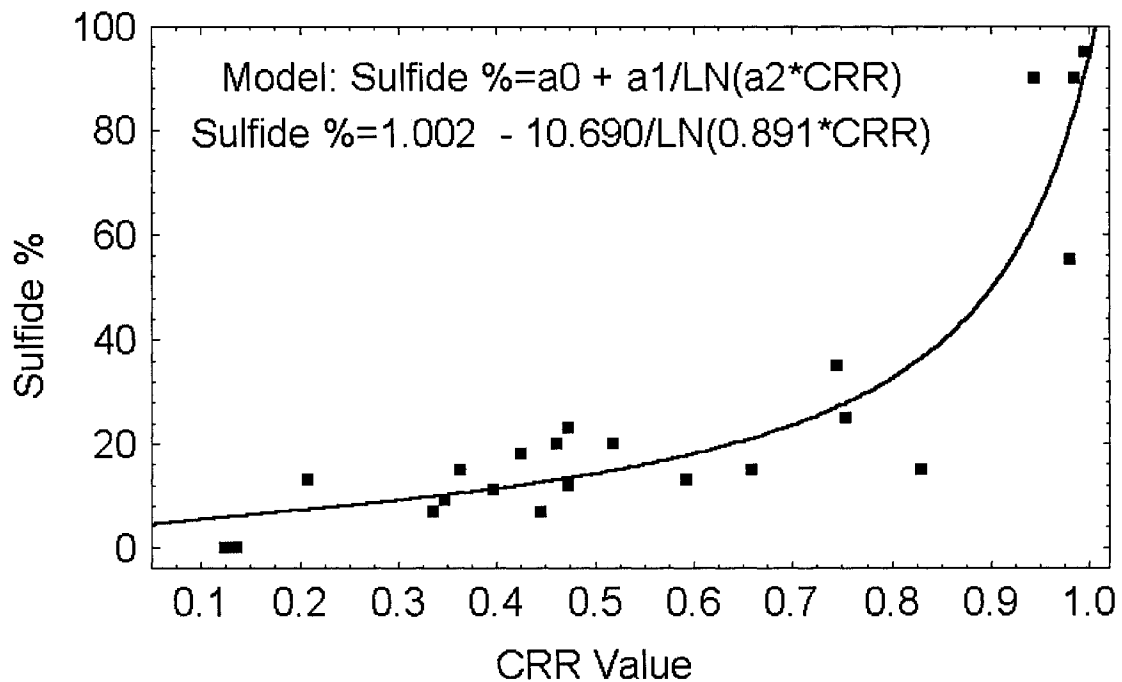


Figure 4.12. Regression between total sulfide and average CRR values at  $1319\text{ cm}^{-1}$ . The mean CRR values were calculated from all available dry and wet measurements for a given sample. See Figure 4.10 for additional details.

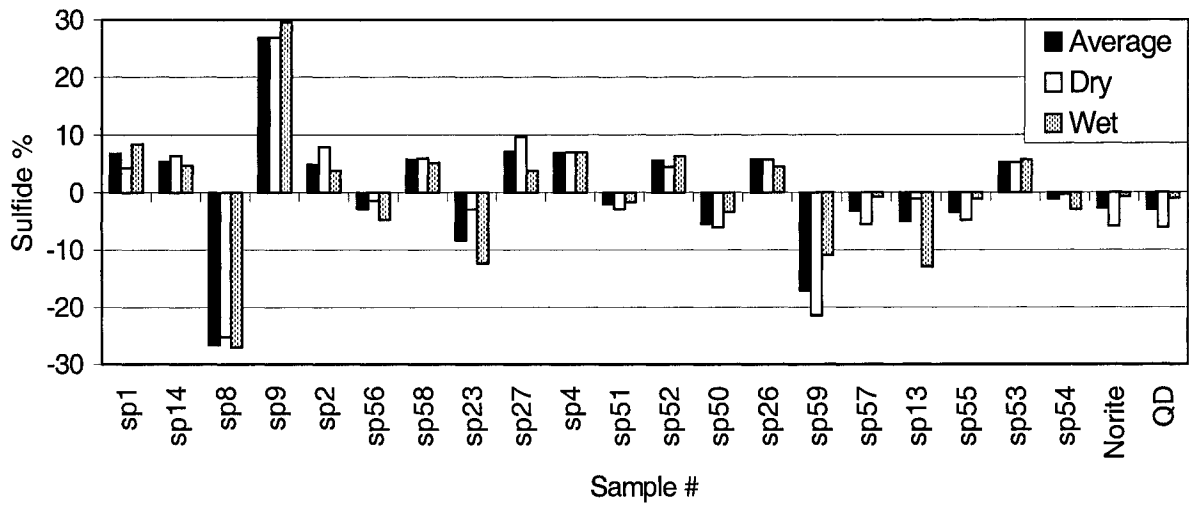


Figure 4.13 Observed minus predicted sulfide concentration for each ore bearing sample, the average norrite, and the average quartz diorite. Positive values indicate an underprediction. Negative values indicate an overprediction. Predicted values were calculated using the regressions shown on Figure 4.10-4.12.



## CHAPTER 5

### TOTAL SULFIDE ESTIMATION OF CORES AND CUT ROCK SURFACES BY THERMAL INFRARED REFLECTANCE

#### 5.1 Introduction

The identification of ore zones and estimation of ore content in rock cores is a labor-intensive routine for the mining industry. This process of core logging is generally conducted visually by geologists. Kruse (1996) used hyperspectral technologies with split cores to identify different silicate alteration minerals from near-infrared spectra, giving encouraging results towards the automation of core logging. No research has been reported on the detection of sulfide minerals in cores using spectroscopy. The detection of sulfide minerals is directly related to the extraction of many base metals such as Ni (nickel), Cu (copper), and Au (Gold). Thus, detecting the presence of sulfide minerals and quantitatively grading the sulfide ore content in cores is of particular importance for the mining industry. This study targets the delineation of sulfide-rich ore zones from their host rock and the direct estimation of sulfide ore grade on cut rock faces (e.g., cores) using Thermal Infrared Reflectance (TIR) spectroscopy.

Thermal Infrared Reflectance spectroscopy over the 3.0 to 30 $\mu$ m region has been conducted for decades to identify the compositional variations within different rocks (Lyon, 1965, 1972; Walter *et al*, 1989; Nash *et al*, 1991). Hundreds of typical TIR spectra of rocks and rock forming minerals have been collected in ideal laboratory conditions by Hunt (1974, 1976) and Salisbury (1993), providing a wealth of spectral references of polished rocks and rock powders of different particle size. There are a few

sulfide TIR spectra in the literature for pyrite, chalcopyrite and pyrrhotite (Farmer, 1974; Ferraro, 1982; Salisbury *et al*, 1991; Rivard *et al*, 2001), which indicate high reflectance in the TIR and a lack of diagnostic spectral features below 27 $\mu\text{m}$ . Recent research (Rivard *et al*, 2001) on naturally broken rock faces demonstrated that 1319 $\text{cm}^{-1}$  (7.58 $\mu\text{m}$ ) is a sensitive spectral position for identifying sulfide ores and the continuum removed reflectance (over 500 to 5000  $\text{cm}^{-1}$ ) at 1319  $\text{cm}^{-1}$  is exponentially related to ore grade. Cut rock surfaces differ from that of broken rock surfaces most notably because of the reduced surface micro-topography that changes the local viewing geometry of spectral measurements and thus affects the intensity of energy received (Hapke, 1981, 1993; Mustard *et al*, 1989). Published work (Rivard *et al*, 2001) shows that sulfide ore detection using continuum removed spectra (Clark *et al*, 1984) minimizes the micro-topographic variations on broken rock surfaces. The removal of a continuum may not be necessary for spectral readings from core and cut rocks and would reduce computational requirements for a real-time core-logging scenario. This indicates that sulfide ore detection from TIR spectroscopy must be re-assessed if it is to be applied to cut rock faces. In addition, ore grading of cores requires quantitative models adaptable for different drilling scenarios (e.g., on cores with different diameters). This requirement points to the need to easily calibrate the model relating TIR signatures and ore grades.

This research was conducted with a view towards the future automation of underground mine operations, especially towards core logging and sulfide ore grading, using TIR hyperspectral devices. The immediate objective was to assess whether sulfide-bearing cores and cut rocks could be discriminated from barren cores and whether their ore grade (%) could be estimated using TIR spectral information. A suite of samples

(cores and cut rocks) was collected from mines of the Sudbury basin, Ontario, Canada. Reflectance properties of sulfide ores in the thermal region and the nature of the quantitative relationship between TIR and total sulfide content (TSC) was explored for cut rock surfaces. Multiple samples of various rock types and different sulfide ore grades were used to validate the quantitative models and address issues of statistical confidence.

## **5.2 Materials and methods**

### **5.2.1 Sample description**

A total of 31 samples (Table 5.1), including 17 core sections and 14 rocks, were collected from mines of the Sudbury basin. Core sections (with various diameters larger than 30 mm) cover the majority of the local rock types, including a structurally deformed breccia, varying granites, granite gneiss, meta sandstone, quartz diorite, amphibolite, olivine diabase, metagabbro and gabbro. The rock samples are all ore bearing rocks with different ore grades. Sulfide ores are disseminated in 12 quartz diorites (DIQD) and 1 norite (DINR). A sample of massive sulfide (MASU) is also included in the sample suite. Sample sp#8 was used for quantitative modeling of the TIR vs. TSC relation and all other samples were used for model validation. Sp#8 is a quartz diorite cut on both sides to form a rock slab approximately 60 mm x 95 mm x 10 mm in physical dimensions. Sulfide minerals in sp#8 form patches of about 10 mm x 10 mm in size. Sulfides are also observed (less than 5% but visually noticeable) in the silicate matrix (dominated by hornblende, plagioclase, quartz), which is fined grained and homogeneous.

For each sample the major ore-forming minerals were identified and estimated by point counting of thin sections. The TSC (%) of each sample was estimated by summing the modal abundance of chalcopyrite ( $\text{CuFeS}_2$ ), pyrrhotite ( $\text{Fe}_{1-x}\text{S}$ ) and pentlandite

((Fe,Ni)<sub>9</sub>S<sub>8</sub>). The TSC of the sample suite spans from 0% (barren host rock) to 95% (massive sulfide).

### 5.2.2 Laboratory setup and experiment

The laboratory environment was set up with an MB102 Fourier transform interferometer (FTIR) using a Mercury/Cadmium/Telluride (MCT) detector to make diffuse bidirectional reflectance measurements (Hapke, 1993). The detector perceives the reflected thermal energy over the 500 cm<sup>-1</sup> to 6000 cm<sup>-1</sup> (1.67 um-20.00 um) range. An Infra-gold<sup>TM</sup> panel was used to normalize the detected energy to thermal infrared reflectance. The spectra recorded for each surface location consist of eight scans at 16 cm<sup>-1</sup> spectral resolution averaged to minimize noise. For cut rock samples, the detector was aligned at a 35 degrees phase angle with nadir illumination from an internal thermal light source. The instrumental field of view (FOV) is adjustable and was setup to 5 mm x 5 mm. Setup for cores was a little different with a 4 mm x 4 mm FOV to minimize the influence of surface curvature. In addition the incidence angle of illumination and viewing angle of detection were equal to 17.5 degrees (near specular mode) to increase the reflected energy and compensate for the smaller FOV. The cores were aligned parallel to the principal plane. An infrared video camera was mounted to visualize the illuminated area and guide the selection of the measured locations. A flexible platform was used to hold and transpose both core and rock samples to preserve the viewing geometry for all measurements. The positioning error for a sample was less than 0.5 mm. The signal to noise ratio (S/N) of the instrument, which was tested each day, was above 1000 within the 500 cm<sup>-1</sup> to 5000 cm<sup>-1</sup> thermal infrared region. A previous reproducibility test (Rivard *et al*, 2001) has shown the instrument to be stable for at least 32 minutes. The

above setup ( $16 \text{ cm}^{-1}$  resolution and 8 scans) allows the completion of measurements for each sample (average 30 spots on each sample) within 30 minutes.

### **5.2.3 Sampling strategy and data arrangement**

The sampling strategy differed for the rock slab (sp#8), cores (sp#76 to sp#92) and other cut rocks (sp#1, sp#4, sp#23, sp#50 to sp#59). The rock slab was scanned intensively following a regular grid, thus sampling the local sulfide abundance variations and was used to acquire a dense data set to model the link between TIR and TSC. Core samples were measured along the core length to simulate an operational core logging process while minimizing curvature of the core faces in the FOV. For cut rocks other than sp#8 multiple representative regions were measured to sample the overall heterogeneity. The sampling strategy for the cores and cut rocks focused on making measurements on spots that best represent the overall sample surface because both cores and cut rocks were used in this research to test the sulfide prediction models derived from the rock slab (sp#8) using ore grades estimated from spectra and from thin section modal counts.

Rock slab sp#8 is a quartz diorite with a sulfide content of 55% based on the analysis of a thin section. Measurement of this sample was conducted on a regular grid (Figure 5.1a, one spot measured in each 5 mm x 5 mm grid cell). The sulfide content within each grid cells was estimated by point counting from a high quality digital photograph of the sample. Each cell and corresponding spectrum include an array of 16 by 16 pixels in the digital photo from which the sulfide point count was conducted.

For each core section, spectra were collected from 21 to 43 adjacent spots along the core length (Figure 5.2), depending on the physical length of the core. This suite of samples includes different silicate host rocks and was used to explore the spectral

signatures of samples free of ore and validate the correctness of sulfide grade estimation for the 0% TSC scenario.

The 13 cut rock samples are all ore bearing with at least one side cut. For each sample, 12 to 25 spots were measured within rectangular grids (Figure 5.3) over multiple regions of the cut surfaces in an attempt to sample the local variations in ore content. This suite of samples displays TSC contents varying from 7% to 95% and was used to validate the correctness of the sulfide estimation model.

### **5.3 Data modeling for the rock slab**

More than 200 spectra were collected for the slab (sp#8) surface (Figure 5.1a). The spectra vary significantly from spot to spot because some of the grid positions were almost fully occupied by sulfide while some were mainly filled with the silicate-rich matrix. Spectra from grid cells at and near the slab edge were rejected to avoid edge effects. A subset of 144 spots (8 x 18 grids that are equivalent to a 40 mm x 90 mm area) within a rectangular region was selected for data modeling. Because the thin section modal analysis only provides an overall TSC estimation for this sample, a high-resolution digital photo (300dpi) was used to provide an estimate of the sulfide content at each spot. The digital photo was taken when the rock slab was wet to enhance the visible contrast between sulfides (shown as bright colors in Figure 5.1a) and silicate-rich matrix (shown as dark black in Figure 5.1a). The photo was co-registered to the spectral cube and re-sampled to the same spatial coverage (16 by 16 pixels for each spot). The co-registration error between the digital photo and the data cube is less than 3 pixels (0.93 mm).

#### **5.3.1 Calculation of local TSC (%) from the digital photo**

On the washed cut surface of slab sp#8, sulfide minerals are light bronze or bright

yellow in color while the silicate matrix is black. To highlight this difference, a supervised maximum likelihood classification (Addington, 1975) was performed on the digital photo based on two training classes: sulfide rich clusters and the silicate matrix. The classification results (Figure 5.1b) clearly separate the slab surface into sulfide pixels and matrix pixels. The classification statistics (Table 5.2) show that 34917 pixels (47.90%) out of 72898 (total pixels) are sulfide and 37981 pixels (52.10%) are matrix. The thin section analysis shows that 55% sulfide minerals are present in this sample. The 7.10% difference between the thin section result and the classification result of the slab does not necessarily indicate that the classification result is biased because the thin section, which was cut off from a portion of the sample, can not cover the same area as the digital photo. The classification result from the digital photo is thought to be more reliable than that of the thin section because the photo covers a large part of the sample.

The abundance of sulfide within each TIR measurement grid cell was calculated using the classification results of the photo (Figure 5.1b), and used as the “true” local TSC percentage for TSC-TIR modeling. Previous research (Bartholomew *et al*, 1989) suggests that the detected radiance within 7-13  $\mu\text{m}$  ( $770\text{--}1430\text{ cm}^{-1}$ ) is dominated by surface reflections as opposed to volume scattering. This suggests that the estimated abundance of sulfide and silicate matrix for each grid cell will represent the major contributors of spectral information measured for that cell.

### **5.3.2 Relationship between TSC and TIR signatures**

As discussed in a previous paper (Rivard *et al*, 2001) the continuum removed thermal infrared reflectance at  $1319\text{ cm}^{-1}$  is sensitive to the concentrations of sulfides in naturally broken rocks. In this study the relationship between sulfide content and TIR was

examined without removal of a continuum. Four spectra from different locations on slab sp#8 are displayed on Figure 5.4. These indicate that an increase in TSC increases the reflectance near 1319 cm<sup>-1</sup> while silicate features from 700 cm<sup>-1</sup> to 1300 cm<sup>-1</sup> are depressed. The spot with 97% TSC (the top spectrum on Figure 5. 4) shows greater than 31.59% reflectance near 1319 cm<sup>-1</sup>. Spectra of spots with no sulfide minerals tend to converge to a reflectance value below 2% near 1319 cm<sup>-1</sup> and display much stronger spectral features from 700 cm<sup>-1</sup>-1300 cm<sup>-1</sup>. This observation is consistent with previous hyperspectral research on sulfides (Rivard *et al*, 2001) showing that sulfide minerals have higher reflectance in the thermal band than silicates and are almost featureless within the 700 cm<sup>-1</sup>-1400 cm<sup>-1</sup> region. Spots filled with both sulfides and silicate minerals create spectral mixtures whose spectra have moderate contrast. Two spectral indices were used for modeling sulfide concentrations. One is the absolute reflectance at 1319 cm<sup>-1</sup> ( $TIR_{1319}$ ). The other is a composite band ratio ( $TIR_{ratio}$ ), which is defined as

$$TIR_{ratio} = 0.5 * \left( \frac{TIR_{995}}{TIR_{1319}} + \frac{TIR_{1180}}{TIR_{1319}} \right)$$

that was used to explore the possibility of improving the

precision of ore estimation by including multiple bands. Published spectra (Salisbury *et al*, 1991) of rock forming minerals indicate that the strongest thermal infrared reflectance peaks of mafic silicate minerals occur near smaller wave number regions than that of felsic silicate minerals. The first ratio term (reflectance at 995 cm<sup>-1</sup> over 1319 cm<sup>-1</sup>) in the above equation increases with the abundance of mafic silicate minerals (augite, hornblende, biotite) and the second term (reflectance at 1180 cm<sup>-1</sup> over 1319 cm<sup>-1</sup>) with the abundance of felsic silicate minerals (quartz, orthoclase, microcline). When the sulfide proportion increases in a given spot, the  $TIR_{ratio}$  will decrease and approach 1.0.  $TIR_{ratio}$  tends to increase when the relative proportion of silicate minerals increases. The



above two indices were calculated for each spot on the rock slab. A visual assessment suggests that the distribution of these two indices (Figure 5.5b, 5.5c) is clearly correlated to the distribution of local TSC (Figure 5.5a). A statistical analysis shows that TSC is linearly correlated to  $TIR_{1319}$  (Figure 5.6a) and exponentially correlated to  $TIR_{ratio}$  (Figure 5.6b).  $R^2$  reaches 0.90 and 0.87 respectively and both estimations are considered non-biased with normally distributed residuals (Figure 5.7a, 5.7b). Cross-validation (Herzberg, 1969) shows that 83% (for  $TIR_{1319}$ ) and 82% (for  $TIR_{ratio}$ ) of the 144 spots on rock sp#8 are properly estimated with less than 10% absolute errors (or residuals) (calculated from counted TSC% minus TSC% predicted by models). The regression line for the TSC vs.  $TIR_{1319}$  relation (Figure 5.6a) predicts a reflectance of 1.05% for a TSC of 0% which is consistent with the published reflectance of silicate rocks near the Christensen frequency (Christensen, 1992). The exponential estimation curve on Figure 5.6b tends to lose sensitivity when TSC is below 10% largely due to the influence of various silicate minerals whose spectral contribution to the mixed spots can not be fully represented by the above band ratio. However a benefit of the spectral ratio is that it is insensitive to minor changes of spectral amplitude caused by uncontrolled factors, thus it was integrated with  $TIR_{1319}$  to form a combined index ( $TIR_{index}$ ), which is represented as,

$$SCP \% = 0.91 + 2.05 * TIR_{1319} + 5.66 * EXP(4.30 - 2.43 * TIR_{ratio})$$

The parameters above were estimated from the 144 spots using a non-linear parameter estimation (Andrew, 1999). Cross validation indicates that this combined index gives a better TSC prediction with  $R^2=0.91$ . 87% of the 144 spots were estimated with less than 10% absolute error and the estimation was robust with normally distributed residuals (Figure 5.7c).

The basic finding outlined in the above empirical modeling is that the total sulfide abundance of cut rock surfaces can be linearly related to thermal infrared reflectance at  $1319\text{ cm}^{-1}$  and exponentially related to the average TIR ratio of  $995\text{ cm}^{-1}$  over  $1319\text{ cm}^{-1}$  and  $1180\text{ cm}^{-1}$  over  $1319\text{ cm}^{-1}$ . However, these models were based on 144 measurements on one rock slab (sp#8), a quartz diorite with 4% chalcopyrite, 7% pyrrhotite and 44% pentlandite. Below, the applicability of these models is evaluated on more rock types with a variety of sulfide contents.

#### **5.4 Model validation on cores and cut rock faces**

The 17 cores and 13 cut rocks (excluding sp#8) listed in Table 5.1 were used for model validation. At least one thin section was analyzed per sample to determine the total sulfide content (chalcopyrite + pyrrhotite + pentlandite). When multiple thin sections were analyzed an average total sulfide content was calculated. Thin section observations shows that the type of sulfide minerals and their contents vary amongst samples. For example, sample sp#1 (massive sulfide) is rich in chalcopyrite (80% modal) while sample sp#23 (norite) is free of chalcopyrite. To validate the models derived from sp#8 using TIR data from different rock types with varying sulfide minerals, two assumptions were made: First the curvature of core faces does not introduce a significant TIR bias. The smallest core diameter is 30mm while the field of view is 4mm x 4mm; consequently, the maximum curvature within a FOV is 1.9 degrees. The total effect of curvature within a FOV is an integration (from 0 degrees to 1.9 degrees) of effects from local facets. The curvature effect was assumed negligible during the model validation and cut rocks and cores were treated as one sample suite. Secondly it is assumed that ore grade determined from thin section analysis and that observed at the sample surface are equivalent. This

assumption is valid for homogeneous samples, for which the percentage of sulfides on the rock surface is equivalent to the volume abundance of sulfides. As seen below the ore grades estimated from the different models was compared to ore grades estimated from thin sections (30 mm x 50 mm in size) taken as the “ground truth”. Whether or not a sample is considered “homogenous” is dependant on the measurement or view scale. For multiple measurements with a footprint less than 5 mm x 5 mm, this assumption was evaluated through the following spectral statistics.

#### **5.4.1 Spectral statistics**

Depending on the physical dimensions of the samples, 12 to 45 spots were measured. In some samples, sulfides occur as blebs or aggregates, which can vary in size and create local textural and compositional heterogeneities at a scale less than 5 mm, though the sample was visually assessed as homogeneous and included in the test. To appraise if the number of measurements conducted on each sample is sufficient to statistically represent the sample, an expectation test (Richard, 1979) was conducted using the measured reflectance near  $1319\text{ cm}^{-1}$ . In this test, an adequate number of measurements is judged to have been taken when the average reflectance approaches a constant value as additional measurements are included. Figure 5.8 shows the results of an expectation test for four samples (sp#23, sp#57, sp#84, sp#86), for which the number of measurements conducted appears sufficient to represent the core section or rock. Additional measurements are not required for samples like these. Figure 5.8 also illustrates one sample (sp#1), which was not considered to have passed the test because a stabilized plateau for the average reflectance was not observed. An expectation test was conducted for all samples and 26 samples passed the test while 4 samples listed in Table 5.3 did not. All host rock samples

passed the test. The average reflectance near  $1319\text{ cm}^{-1}$  of sulfide free samples (e.g., sp#84, sp#86 displayed on Figure 5.8) displays a stable value between 0.40% and 1.50%, close to the predicted value (1.05%) derived from the  $TIR_{1319}$  model.

A stable plateau of average reflectance could not be confidently determined for four samples (#sp1, #sp52, #sp81, and #sp83) indicating that current numbers of measurements are not sufficient to represent the local compositional or textural variations for these samples. Sp#1 is a massive sulfide with 95% sulfide ore. The other three are quartz diorites with disseminated sulfides at lower concentrations (sp#52: 8%, sp#83:15% and sp#81:15%). Due to limitation of physical dimensions of these samples, more measurements could not be conducted. However, the trends of the spectral averages of these samples are clearly identifiable indicating that they are approaching a stable value. This observation suggests that the ore grade for these samples will be either overestimated or underestimated in a predictable way if the current spectral average is used for the sulfide prediction models. During the model validation described in the next section, average spectra, which represent their expectation, were used for all 26 samples that passed the expectation test. For the 4 suspicious samples, because no clear expectation plateau can be observed, a virtual expectation was set at the mathematical average of the points on the expectation curve for each sample. For sp#1, the expected average reflectance at  $1319\text{ cm}^{-1}$  was set as 32.17%. The expectation test helps to determine how representative the TIR measurements are. The ore prediction models were evaluated both with and without these 4 samples. The assessment without these samples helped to define the estimation using ideal measurements. Including these 4 samples in the assessment helps to understand the behaviors of models under more practical and less

rigid conditions when the representativeness of measurements is unknown.

#### 5.4.2 Qualitative assessment of models

During the validation, sulfide estimation using  $TIR_{1319}$  and  $TIR_{index}$ , in which  $TIR_{ratio}$  is integrated, was assessed (Table 5.4). The results were compared with the sulfide abundance estimated from thin section analysis. The criteria used to evaluate the predictions are,

- (a) Absolute error ( $e$ ) (Table 5.4), which is defined as the observed total sulfide (% from thin section analysis) minus the predicted TSC (% from each model).  $e$  outlines the envelope of maximum absolute prediction error. For all samples, the first three maximum error values are -11.64%(sp#83), -8.38%(sp#81) and -7.50%(sp#1). All are for suspicious samples that did not pass the expectation test indicating that the spectral measurements are not fully representative of the whole sample. In all cases the predictions tend to overestimate the TSC as expected (Table 5.3) based on the expectation test. The predictions for all remaining samples show absolute errors less than 7.22% (Table 5.4) and less than 3.67% for the ore free samples.
- (b) Mean ( $m$ ) of absolute error ( $e$ ) (Table 5.5), which is calculated from the statistical distribution of the absolute errors.  $m$  should be zero for a non-biased estimation. The maximum  $m$  value (-2.65% absolute) occurred while using the  $TIR_{index}$  on ore free samples indicating an overestimation.
- (c) Standard deviation of absolute error ( $stdev$ ), which delineates the variation of absolute errors within a stated confidence level.  $stdev$  is less than 4.86% for ore containing samples and less than 0.91% for sulfide free samples (Table 5.5).

Excluding the suspicious samples from the ore containing samples improves the *stdev* of estimation error for the  $TIR_{index}$  indicating that it is less robust than  $TIR_{1319}$  at low ore grades that characterize the suspicious samples. *Stdev* is higher on ore bearing samples than on ore free samples for both estimators even when suspicious samples are excluded. This is most probably due to errors during thin section analysis because the TSC can be confidently set to 0% for sulfide free samples while the TSC of ore bearing samples are subject to counting errors using thin sections, particularly for samples of low ore content and for samples with non-uniformly distributed sulfides.

- (d) The correlation coefficient  $R^2$  of observed ore grade (from thin section) vs. predicted ore grade (from models) (Table 5.5) and the slope ( $k$ ) of the regression line (Figure 5.9). These two parameters are indicative of the degree of the above correlation and the degree of systematic estimation bias over the entire ore grade range (0% to 100%). All 30 sample points are located near the  $k=1.0$  line and both models have  $R^2$  values bigger than 0.96 indicating that the predicted TSC% represents well the true TSC%. The  $k$  values (1.07 and 1.09) indicate a small overestimation. Excluding the 4 suspicious samples does not significantly improve  $k$  and  $R^2$  indicating that the current number of measurements for these samples, though not considered sufficient based on the expectation test, did not introduce a bias for ore estimation over the entire ore grade range. This suggests that their current average spectra are approaching their normal expectations.

The 14 sulfide free rocks have an average reflectance at  $1319\text{ cm}^{-1}$  of 0.85% (maximum 1.35% and minimum 0.47%). On a scatter plot of predicted versus observed

total sulfide (Figure 5.9), ore free silicate rocks cluster near the (0,0) point and are distinct from sulfide bearing rocks. The lowest ore grade for the ore bearing samples is 7% (sp#51). To setup the statistical confidence and theoretical threshold for discriminating ore free hosts from ore bearing rocks using the existing 30 validation samples, 14 ore free samples and 16 ore bearing samples were considered as two separate categories. When the statistical confidence level (Yamane, 1967) was set at 70% ( $1.03*stdev$ ) and 90% ( $1.64*stdev$ ) for ideal non-biased estimations, the probability distribution of ore prediction errors within each group will be 15% to 85% at 70% confidence and 5% to 95% at 90% confidence (Figure 5.10). Table 5.6 lists the absolute ore grade errors for the two categories if predicted at 70% and 90% confidence using the the  $TIR_{I319}$  and  $TIR_{index}$  models. As indicated by Figure 5.10, the mean and deviation of the errors are different for the two classes. Discriminant analysis (Klecka, 1980) suggests that when the true ore grade is higher than 4.82% (threshold in Table 5.6) it can be estimated using  $TIR_{I319}$  with an absolute error of  $\pm 3.89\%$  at a 70% confidence level. At a 90% confidence level, ore grade (when higher than 7.68%) can be predicted with an absolute error of  $\pm 6.19\%$  using  $TIR_{I319}$ . When the true ore grade in a specific sample is lower than the thresholds listed in Table 5.6, there is a higher possibility of misidentifying the sample as ore free.  $TIR_{index}$  does not perform as well as  $TIR_{I319}$  under this ideal assumption (estimation error is assumed to be normally distributed with zero mean) but the difference is not significant. In a practical scenario, the mean of the estimation error may not be zero (as in Table 5.5), indicating that there is a necessity for calibrating the models to remove a systematic estimation bias, which is well represented by the mean of estimation errors.

The validation is subject to estimation errors embedded in thin section data, which was collected by visual point counting on thin sections cut from one or two small portions of the core or rock samples. How well the thin sections represent the entire cores or rocks is questionable and difficult to evaluate.

## **5.5 Discussion on practical issues**

The successful application of these models to cores requires further examination of factors that will possibly affect sulfide estimation results. Factors such as the curvature of the core surface and the dimensions of the instrument FOV have been identified and will be discussed in the appendix or investigated in later studies. Two issues, namely the calibration of models and the effect of the continuum removal on the models, will be explored in this section. The calibration of models was explored to provide further guidance towards the development of practical applications. The removal of the continuum is a common spectral processing method and the discussion will focus on its influence on the prediction of TSC% illustrating the necessity of using raw thermal infrared reflectance spectra rather than continuum removed spectra for ore grading on cores and cut rocks.

### **5.5.1 Effect of spectral continuum removal**

Raw reflectance spectra rather than continuum removed spectra were used to predict total TSC in this study. The continuum is the overall spectral amplitude or "background" onto which mineral spectral features are superimposed. The continuum is subject to changes in the geometry of measurements and thus its removal can minimize variations in the geometry of the measured surface (e.g., micro-topography). The removal of the continuum has been extensively used (Kruse *et al*, 1985, 1993; Clark *et al*, 1984, 1987)



as a useful tool to highlight spectral features, particularly to delineate local minima and maxima of spectra, which are usually indicative of specific mineralogical information. However, the removal of a sloping continuum is known to cause apparent shifts (Clark *et al.*, 1987) in the position of reflectance minima such as that at  $1319\text{ cm}^{-1}$ , which in this case is a key parameter for the estimation of TSC. TIR spectra of silicate rocks converge to a local minima near  $1319\text{cm}^{-1}$  and the local continuum of rock spectra is tilted. A test was conducted using the 144 spectra from sp#8 by removing the spectral continuum over two spectral ranges. The relationship between “true” TSC and the continuum removed reflectance at  $1319\text{ cm}^{-1}$  (Figure 5.11) is non-linear as opposed to that using the original reflectance which is linear. The degree of non-linearity is dependant on the spectral range over which the spectral continuum was removed. This effect will propagate into the  $TIR_{ratio}$  model, in which the  $TIR_{1319}$  component is embedded. Another reason for using raw reflectance for ore grading is that the spectral continuum not only changes over different spectral regions, but also varies for different host rock types, which may have various spectral tilting or envelopes. The dependency on host rock type introduces uncertainty for the estimation of sulfides from continuum removed spectra. Therefore, it is recommended that raw reflectance be used to predict total sulfide content for cut rocks and cores when the effect from curvature or local surface topography is not significant.

### **5.5.2 Model calibration**

In operational scenarios, the instrument setup and viewing geometry may differ from that of the laboratory experiment in this study. In addition the roughness of the core surface may also be different depending on the drilling process. These two factors will affect the reflectance measurements in the thermal region. For example, the  $TIR_{1319}$

model estimates ore grade from the reflectance at  $1319\text{ cm}^{-1}$  and the reflectance is dependant on the viewing geometry and surface scattering properties at a specific setup (Sandmeier *et al*, 1998). The calibration of models allows the prediction models to be adapted to a given measurement scenario by optimizing the model parameters and minimizing systematic errors while preserving the basic TIR-TSC relation. By measuring a few samples of known ore grades, the parameters for model  $TIR_{1319}$  and  $TIR_{index}$  can be estimated for any setup. A minimum of two samples is required for the model  $TIR_{1319}$  though additional calibration samples would improve the calibration. A calibration should involve at least one sample with low ore grade and one with high ore grade to avoid local estimation biases and a poor calibration beyond the ore grade range displayed by the calibration samples. A minimum of three samples is required for  $TIR_{index}$  calibration due to the exponential term.

Though none of the two models showed a significant advantage over the other during the validation process, each has its own merits in terms of possible application scenarios.  $TIR_{index}$  requires one more sample for calibration than  $TIR_{1319}$  does, but due to the integration of the band ratio component,  $TIR_{index}$  is less sensitive to minor spectral amplitude variations caused by uncontrolled factors between calibrations.  $TIR_{1319}$  would be well suited for real-time sulfide estimation and can be easily calibrated. Because it requires only one TIR band, a customized instrument design using  $TIR_{1319}$  to estimate ore grade would be less costly than that using  $TIR_{index}$ , which requires three thermal bands.

## 5.6 Conclusions

This study explored the possibility of using Thermal Infrared Reflectance to delineate sulfide ore zones and estimate ore content in cut rock samples. Experiments were

conducted in the laboratory on cut rock faces and rock cores targeted for core logging. An empirical relationship between the total sulfide content (chalcopyrite + pyrrhotite + pentlandite) and the thermal infrared reflectance was established. The major conclusions from this research are,

- (1) The thermal infrared reflectance at  $1319\text{ cm}^{-1}$  of sulfide disseminated silicate rock is linearly related to the total sulfide content of the samples. The average of the spectral ratios of  $995\text{ cm}^{-1}$  over  $1319\text{ cm}^{-1}$  and  $1180\text{ cm}^{-1}$  over  $1319\text{ cm}^{-1}$  is exponentially related to the total sulfide content of the samples. The correlation coefficient exceeds 0.9 for both relationships.
- (2) The total sulfide content of the samples can be estimated using spectral indices ( $TIR_{1319}$  or  $TIR_{index}$ ) with a maximum mean error of 2.65% and standard deviation of 4.86% with respect to the ore grade calculated from the analysis of thin sections.
- (3) Sulfide bearing samples can be confidently (greater than 90% correctness) separated from host rocks when the total sulfide content exceeds 7.68% and that their sulfide content can be predicted with a standard deviation of 6.19% from the true content if the mean error is removed using a calibration.
- (4) For operational core logging scenarios, a minimum of two and three samples are required respectively for the calibration of the  $TIR_{1319}$  and  $TIR_{index}$  models.
- (5) The removal of the continuum from spectra renders the TSC-TIR relationship non-linear. The use of raw TIR data is recommended for total sulfide estimation on cut rocks and cores.

The “true” sulfide content of samples was calculated from thin section analysis, in

which a subjective bias exists in the identification of mineral and in the location of the thin section on the sample. More rigorous ore grade measurement methods should be used to calibrate the models in operational scenarios to avoid systematic prediction biases.

### **Acknowledgements**

The project was jointly funded by Inco Ltd and the European Space Agency (ESA). Access to a MB102 FTIR was provided by Bomem Inc. The assistance of Brian Thompson, Greg Greenough and Wayne Garland, all from Inco Ltd, was invaluable in obtaining and identifying the samples.

### **REFERENCES**

- Addington, J.D., 1975, A hybrid maximum likelihood classifier using the parallelepiped and bayesian techniques. 50<sup>th</sup> annual meeting of the American society of photogrammetry, **2**, 772-784.
- Andrew, W., 1999, Statistical pattern recognition, Chapter 5, Oxford University Press, Arnold, New York , USA.
- Bartholomew, M.J., Kahle, A. B. and Hoover, G., 1989, Infrared spectroscopy (2.3-20um) for geological interpretation of remotely sensed multispectral thermal infrared data. *Int. J. Remote Sensing*, **10**, 529-544.
- Boardman J.W., 1990, Inversion of high spectral resolution data. *Proc. SPIE Tech. Symposium*,**1298**: 222-233.

- Boardman J.W., 1993, Automated spectral unmixing of AVIRIS data using convex geometry concepts. Summaries of the 4<sup>th</sup> annual JPL airborne geoscience workshop, 11-14.
- Clark, R.N., King, T. V.V. and Gorelick, N. S., 1987, Automatic continuum analysis of reflectance spectra. Proceedings of the 3<sup>rd</sup> airborne imaging spectrometer data analysis workshop, JPL publication 77-30, Jet Propulsion Laboratory, California Institute of Technology, Pasadena, Calif., USA, 138-142.
- Clark, R.N. and Roush, T.L., 1984, Reflectance spectroscopy: Quantitative analysis techniques for remote sensing applications. J. Geophys. Res., **89**, 6329- 6340.
- Christensen, P.R., 1992, Thermal emission spectrometer experiment: The mars observation mission. J. Geophys. Res., **97**, 7719-7734.
- Farmer, V.C., 1974, The infrared spectra of minerals, Bartholomew press, Dorking, Surrey, 117.
- Ferraro, J.R., 1982, The Stadler infrared handbook of minerals and clays. Stadler Research Laboratories, Philadelphia, 476.
- Hapke, B., 1981, Bidirectional reflectance spectroscopy 1: Theory. J. Geophys. Res., **86**, 3039-3054.
- Hapke, B. 1993, Theory of reflectance and emittance spectroscopy *in* Arvidson, R., and Rycroft, M. J., Eds., Topics in remote sensing, Cambridge University Press.
- Herzberg, P.A., 1969, The parameters of cross-validation. Chapter 3, New York, The Psychometric Society, USA.
- Hunt, G.R. and Salisbury, J.W., 1974, Mid-infrared spectral behavior of igneous rocks.

- Environmental Research Paper **496-AFCRL-TR-74-0625**, Hanscom Air Force Base, Air Force Cambridge Research Laboratories, U.S.A.
- Hunt, G.R. and Salisbury, J.W., 1976, Mid-infrared spectral behavior of metamorphic rocks. Environmental Research Paper 543-AFCRL-TR-76-0003, Hanscom Air Force Base, Air Force Cambridge Research Laboratories, U.S.A.
- Klecka, W., 1980, Discriminant Analysis. University Paper Series on Quantitative Applications in the Social Sciences. Newbury Park, CA, U.S.A.
- Kruse, F.A., 1996, Identification of minerals in drill core using hyperspectral image analysis of infrared reflectance spectra. *Int. J. of Remote Sensing*, **9**, 1623-1632.
- Kruse, F.A., Lefkoff, A. B. and Dietz, J. B., 1993, Expert System-Based Mineral Mapping in northern Death Valley, California/Nevada using the Airborne Visible/Infrared Imaging Spectrometer (AVIRIS). *Remote Sensing of Environ.*, Special issue on AVIRIS, May-June 1993, **44**, 309 - 336.
- Kruse, F.A., Raines, G. L. and Watson, K., 1985, Analytical techniques for extracting geologic information from multichannel airborne spectroradiometer and airborne imaging spectrometer data: in Proceedings, International Symposium on Remote Sensing of Environment, Thematic Conference on Remote Sensing for Exploration Geology, 4th, Environmental Research Institute of Michigan, Ann Arbor, 309-324.
- Lyon, R.J.P., 1965, Analysis of rocks by spectral infrared emission (8-25  $\mu\text{m}$ ). *Econ. Geol.*, **60**, 715-736.
- Lyon, R.J.P., 1972, Infrared spectral emittance in geology mapping: Airborne spectrometer data from Pigsash Crater, Calif. *Sciences*, **175**, 983-986.

- Mustard, J. F. and Pieters, C. M., 1989, Photometric phase functions of common geologic minerals and applications to quantitative analysis of mineral mixture reflectance spectra, *J. Geophys. Res.*, **94**, 13,619-13634.
- Nash, D.B. and Salisbury, J.W., 1991, Infrared reflectance spectra of plagioclase feldspar. *J. Geophys. Res.*, **18**, 1151-1154.
- Richard V.D. and Brian, J.S., 1979, *Rocks and rock minerals*: John Wiley & Sons, New York, U.S.A.
- Rivard, B., Feng, J., Gallie, A. and Francis, H., 2001, Ore detection and grade estimation in Sudbury mines using thermal infrared spectroscopy. *Geophysics*, **66(6)**, 1691-1698.
- Rivard, B., Thomas, P. and Giroux, J. 1995. Precise emissivity of rock samples. *Remote Sens. of Environ.*, **54**, 161-167.
- Salisbury, J.W., 1993, Thermal infrared (2.5-13.5  $\mu\text{m}$ ) spectroscopy: Laboratory data, Chapter 4, *in* Pieters, C., and Englert, P., Eds., *Remote Geochemical Analysis: Elemental and Mineralogical Composition*, Cambridge University Press
- Salisbury, J.W. and Eastes, J.W., 1985, The effect of particle size and porosity on spectral contrast in the mid-infrared. *Icarus*, **64**,586-588.
- Salisbury, J.W., Walter, L.S., Vergo, N. and D'Aria, D.M., 1991, *Infrared (2.1-25  $\mu\text{m}$ ) spectra of minerals*. Johns Hopkins University Press.
- Sandmeier, S., Muller, C., Hosgood, B. and Andreoli, G., 1998, Sensitivity analysis and quality assessment of laboratory BRDF data. *Remote Sens. Environ.*, **64**, 176-191.
- Walter, L.S., and Salisbury J.W. 1989, Spectral characterization of igneous rocks in the

8- to 12- $\mu\text{m}$  region. J. Geophys. Res., **94(B7)**, 9203-9212.

Yamane, T., 1967, Elementary sampling theory, Prentice-Hall, Inc., Englewood Cliffs,  
N.J.48-64.



Table 5.1 List of core and cut rock samples

Sample type	Rock type	Sample ID	FOV (mm)	# scans <sup>d</sup>	# spots <sup>e</sup>	% Cp <sup>f</sup>	% Po <sup>f</sup>	% Pn <sup>f</sup>	% Total sulfide
Core	Breccia	90	4x4	8	42	--	--	--	--
	Granite	76	4x4	8	36	--	--	--	--
		84	4x4	8	38	--	--	--	--
	Granite gneiss	91	4x4	8	39	--	--	--	--
		92	4x4	8	38	--	--	--	--
	Metasediment	86	4x4	8	34	--	--	--	--
	Quartz diorite	87	4x4	8	22	--	--	--	--
		80	4x4	8	36	--	--	--	--
		79	4x4	8	43	--	--	--	--
	Amphibolite	78	4x4	8	32	--	--	--	--
	Olivine diabase	77	4x4	8	40	--	--	--	--
	Metagabbro	85	4x4	8	36	--	--	--	--
	Gabbro	88	4x4	8	40	--	--	--	--
		89	4x4	8	40	--	--	--	--
DIQD <sup>a</sup>	82	4x4	8	30	6	8	1	15	
	81	4x4	8	40	3	10	2	15	
	83	4x4	8	21	1	10	1	12	
Rock	DIQD	51	5x5	8	33	1	5	1	7
		57	5x5	8	36	1	5	1	7
		52	5x5	8	45	3	4	1	8
		54	5x5	8	40	1	7	3	11
		56	5x5	8	23	2	9	1	12
		55	5x5	8	36	10	2	1	13
		59	5x5	8	34	1	11	3	15
		50	5x5	8	32	6	8	1	15
		58	5x5	8	40	4	12	2	18
		53	5x5	8	40	2	15	3	20
	4	5x5	8	19	12	6	2	20	
	DINR <sup>b</sup>	23	5x5	8	35	0	21	4	25
	MASU <sup>c</sup>	1	5x5	8	12	80	10	5	95
Slab	DIQD	8	5x5	8	144	4	7	44	55

<sup>a</sup> Disseminated in Quartz Diorite; <sup>b</sup> Disseminated in Norite; <sup>c</sup> Massive Sulfide <sup>d</sup> # of co-add scans for each measurement; <sup>e</sup> # of measurements on each sample; <sup>f</sup> from thin section point counts where Cp = chalcopyrite, Po = pyrrhotite, and Pn = pentlandite.

Table 5.2 Classification results of the digital photo for rock slab sp#8

<b>Digital Number</b>	<b># pixels</b>	<b>Area %</b>	<b>Area % Accumulated</b>	<b># pixels Accumulated</b>
0 (matrix)	37981	52.10%	52.10%	37981
1 (sulfide)	34917	47.90%	100.00%	72898

Table 5.3 Suspicious samples resulting from the expectation test and the expected ore prediction bias

	Cut rocks		Cores	
Sample ID	Sp#52	Sp#1	Sp#81	Sp#83
Effect <sup>(a)</sup>	- <sup>(b)</sup>	+ <sup>(b)</sup>	+	+

<sup>(a)</sup> Predicted effect on the estimation of total sulfide using the current and insufficient number of spectra. <sup>(b)</sup> The average of all available measurements tends to overestimate (+) or underestimate (-) the true sulfide content.

Table 5.4 TSC predicted from  $TIR_{1319}$  and  $TIR_{index}$

Sample #	TSC% from thin section	Predicted TSC%		% <i>e</i>	
		$TIR_{1319}$	$TIR_{index}$	$TIR_{1319}$	$TIR_{index}$
90	0.00	0.18	3.17	-0.18	-3.17
76	0.00	-1.87	1.87	1.87	-1.87
84	0.00	-1.59	2.05	1.59	-2.05
91	0.00	-1.20	2.29	1.2	-2.29
92	0.00	-1.44	2.14	1.44	-2.14
86	0.00	0.45	3.35	-0.45	-3.35
87	0.00	-1.86	1.87	1.86	-1.87
80	0.00	-1.18	2.30	1.18	-2.30
79	0.00	-0.78	2.56	0.78	-2.56
78	0.00	0.96	3.67	-0.96	-3.67
77	0.00	0.07	3.10	-0.07	-3.10
85	0.00	-0.58	2.69	0.58	-2.69
88	0.00	0.13	3.14	-0.13	-3.14
89	0.00	-0.14	2.97	0.14	-2.97
51	7.00	12.79	11.21	-5.79	-4.21
57	7.00	14.22	12.11	-7.22	-5.11
52*	8.00	3.98	5.60	4.02	2.40
54	11.00	11.80	10.58	-0.8	0.42
56	12.00	6.13	6.96	5.87	5.04
83*	12.00	15.01	23.64	-3.01	-11.64
55	13.00	13.17	11.47	-0.17	1.53
59	15.00	14.39	13.09	0.61	1.91
50	15.00	20.44	17.82	-5.44	-2.82
82	15.00	15.47	21.06	-0.47	-6.06
81*	15.00	15.60	23.38	-0.6	-8.38
58	18.00	24.63	18.89	-6.63	-0.89
53	20.00	19.22	15.30	0.78	4.70
4	20.00	23.38	22.54	-3.38	-2.54
23	25.00	29.68	23.79	-4.68	1.21
1*	95.00	99.90	102.50	-4.9	-7.50

\* Samples that did not successfully pass the expectation test. Absolute error (*e*), is the observed total sulfide (% from thin section analysis) minus the predicted TSC (% from each model).

Table 5.5 Statistics of total sulfide predictions

Sample number	Model	Ore-free samples		Ore-containing samples		All samples	
		<i>m</i> (%)	<i>stdev</i> (%)	<i>m</i> (%)	<i>stdev</i> (%)	$R^2$	Slop ( <i>k</i> )
30(26) <sup>(*)</sup>	$TIR_{1319}$	0.63	0.91	-1.98(-2.27)	3.78(3.89)	0.98(0.92)	1.07(1.11)
	$TIR_{index}$	-2.65	0.58	-1.99(-0.56)	4.86(3.65)	0.96(0.82)	1.09(0.99)

(\*) Data in brackets are from 26 samples excluding suspicious samples. Data outside brackets are from all 30 samples including the suspicious samples.

Table 5.6 Error in TSC as a function of the model and confidence level

Models	<b>1.03*stdev (70% confidence)</b>			<b>1.64*stdev (90% confidence)</b>		
	Ore-free	Ore-bearing	Threshold <sup>a</sup>	Ore-free	Ore-bearing	Threshold <sup>a</sup>
<b><i>TIR</i><sub>1319</sub></b>	0.93%	3.89%	4.82%	1.49%	6.19%	7.68%
<b><i>TIR</i><sub>index</sub></b>	0.59%	5.00%	5.59%	0.95%	7.97%	8.92%

<sup>a</sup> Thresholds above which the ore content can be predicted with corresponding confidence level. For example, at a 70 confidence level ore bearing samples with greater than 4.82% TSC will show a predicted TSC with an error of 3.89% using the *TIR*<sub>1319</sub> model.

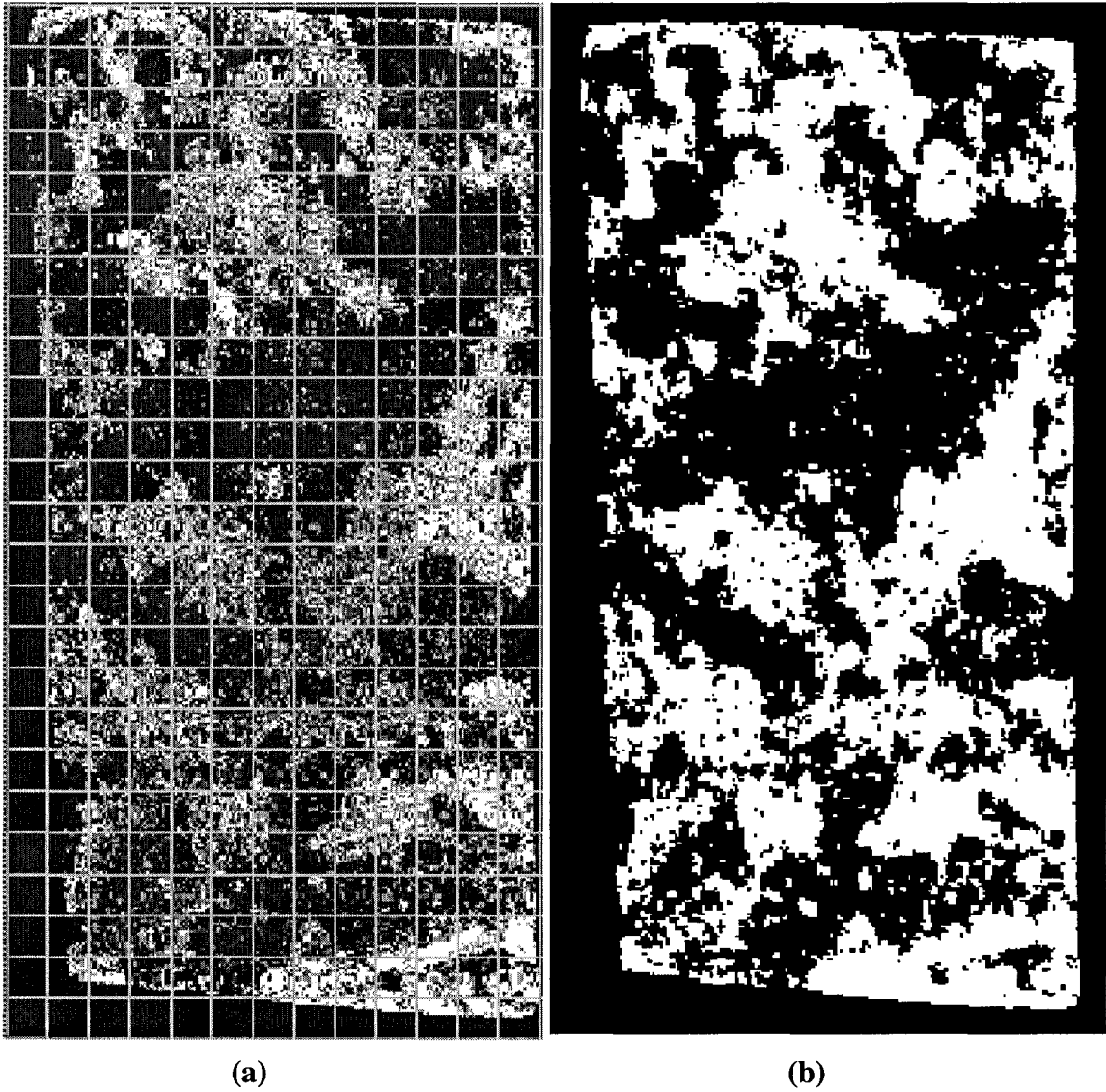


Figure 5.1 (a) left: Digital photograph of rock slab (Sp#8) and the grid system (5 mm x 5 mm) showing each cell measured; (b) right: Supervised classification result showing white pixels as sulfide locations and black pixels as silicate matrix.

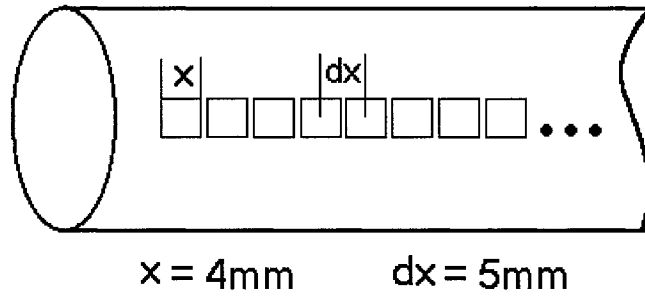


Figure 5.2 Schematic diagram of general layout of spots measured on cores



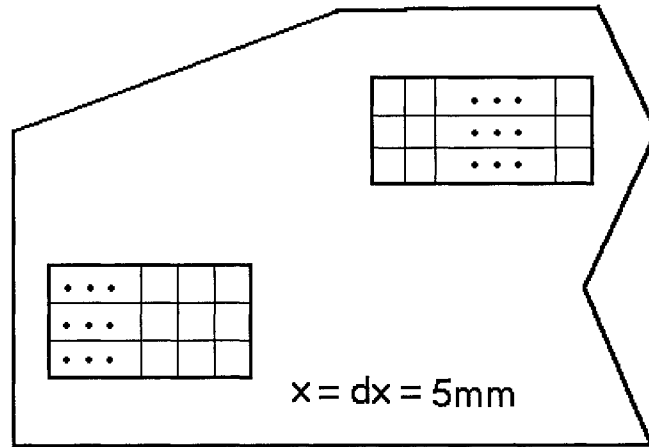


Figure 5.3 Schematic diagram of general layout of spots measured on cut rock faces

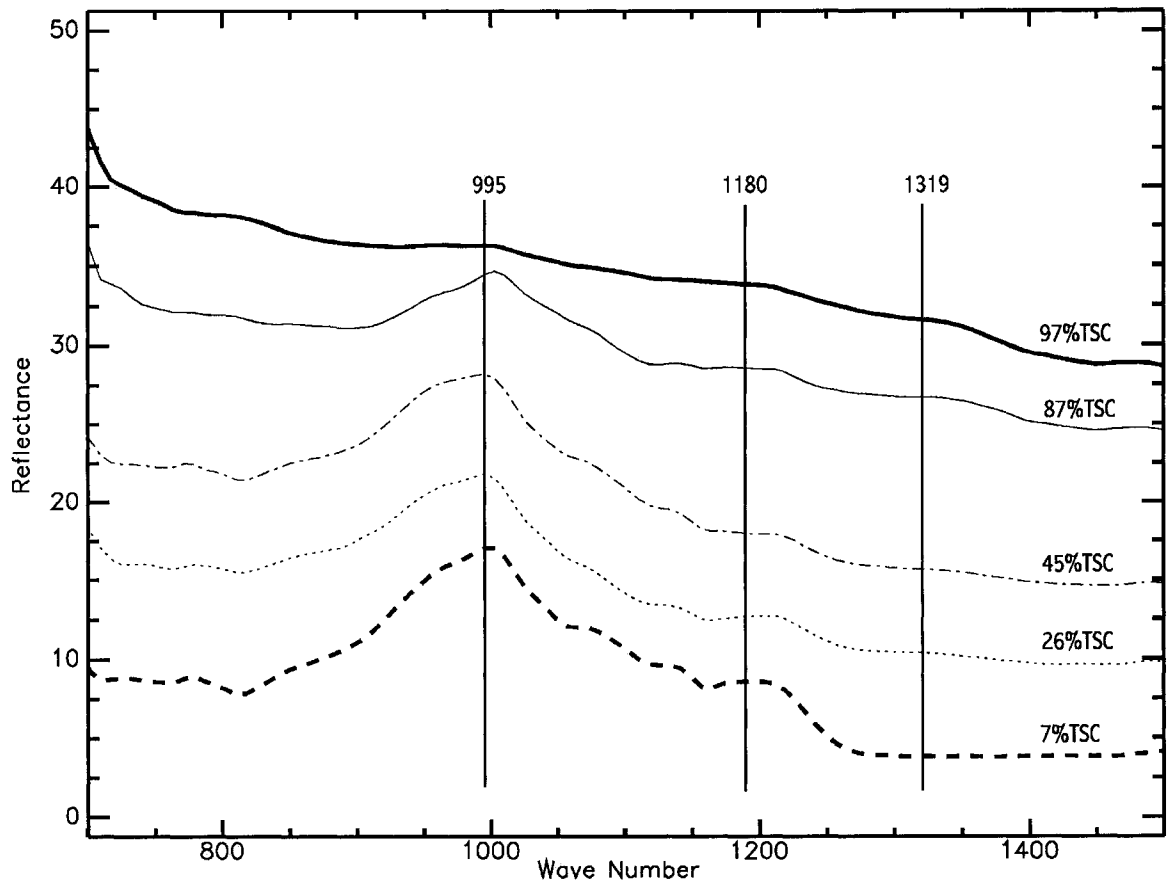


Figure 5.4 TIR spectra from typical spots on rock slab (sp#8) with different TSC values.

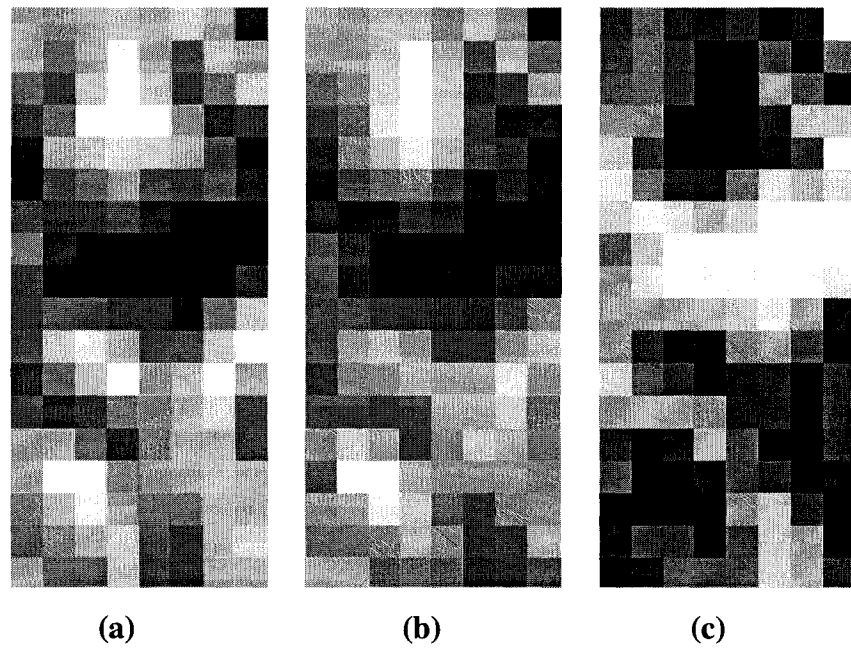


Figure 5.5 (a) left: visualization of local TSC (%) estimated from the photo for sp#8. Brighter grid cells indicate higher local TSC; (b) middle: visualization of TIR spectral slice of reflectance at  $1319\text{cm}^{-1}$ . Brighter positions represent higher TIR values; (c) right: visualization of TIR ratios. Brighter squares indicate bigger spectral ratios and lower TSC values.

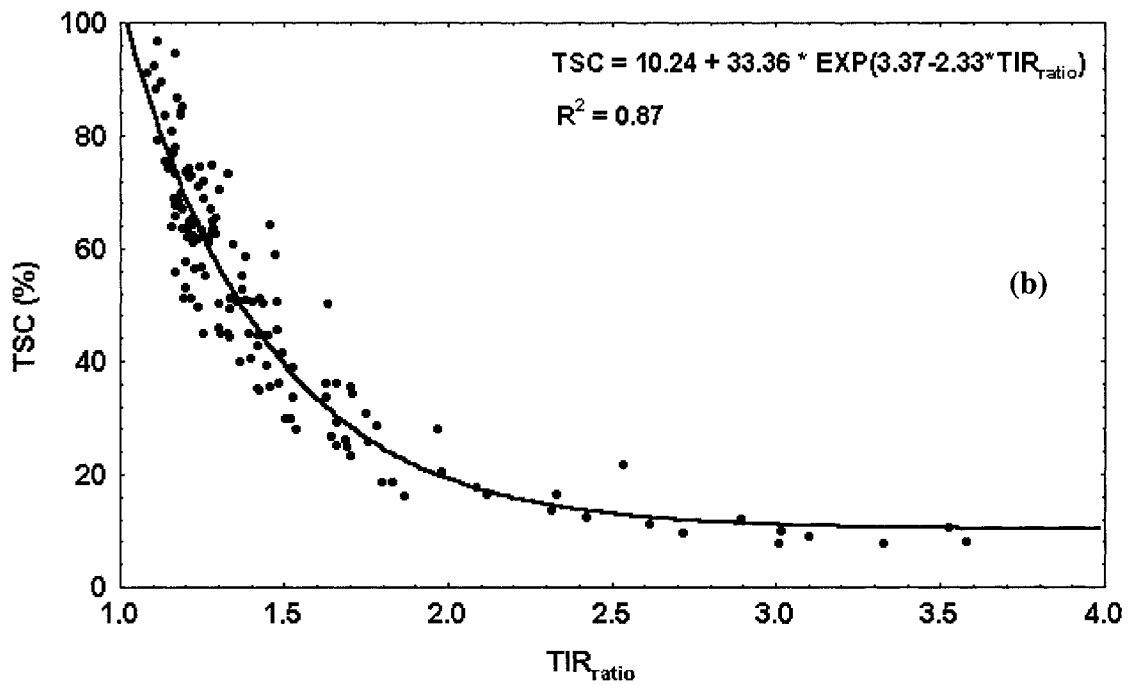
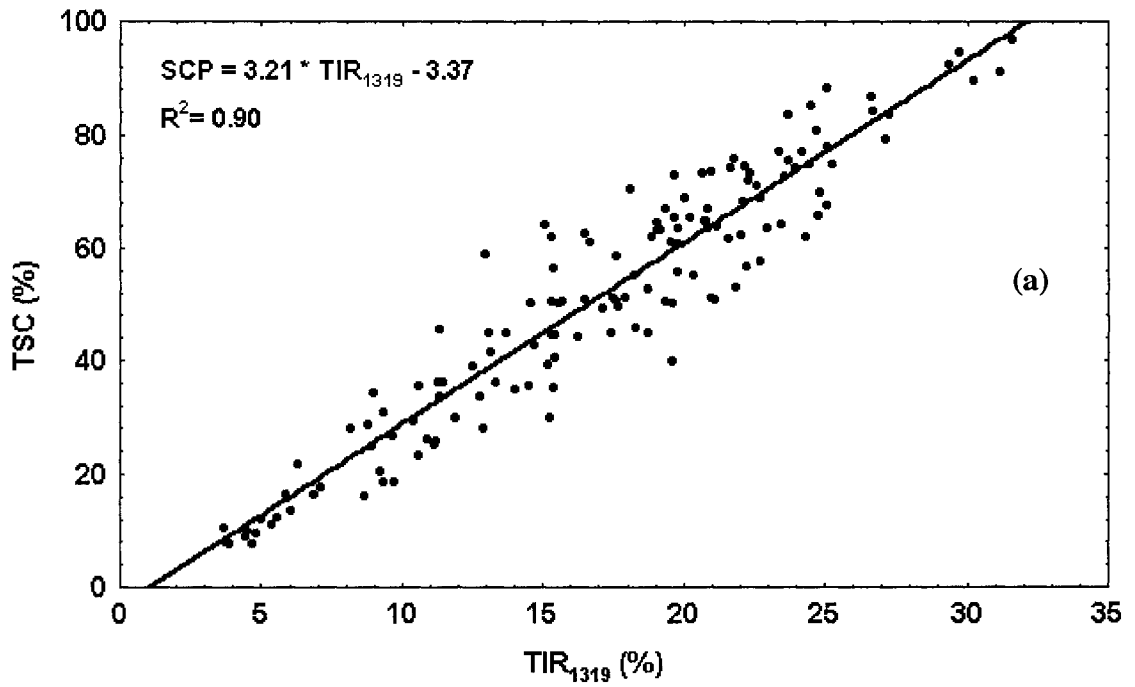


Figure 5.6 (a) upper: relationship between TSC (%) and  $TIR_{1319}$  (%) on rock slab sp#8;  
 (b) lower: relationship between TSC (%) and  $TIR_{ratio}$  on rock slab sp#8.

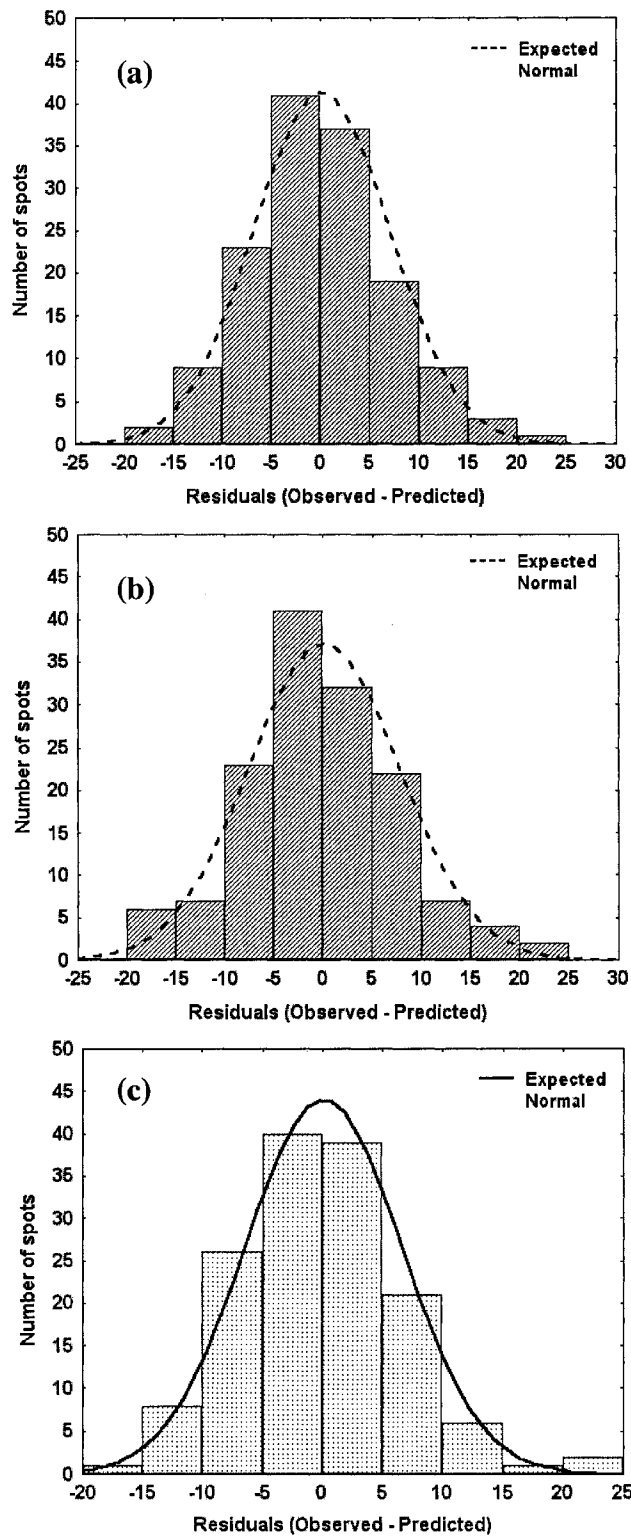


Figure 5.7 Distribution of estimation error (residuals) for different spectral indices. (a) upper: estimation by  $TIR_{1319}$ ; (b) middle: estimation by  $TIR_{ratio}$ ; (c) lower: estimation by  $TIR_{index}$  (linear combination of  $TIR_{1319}$  and  $TIR_{ratio}$ ).

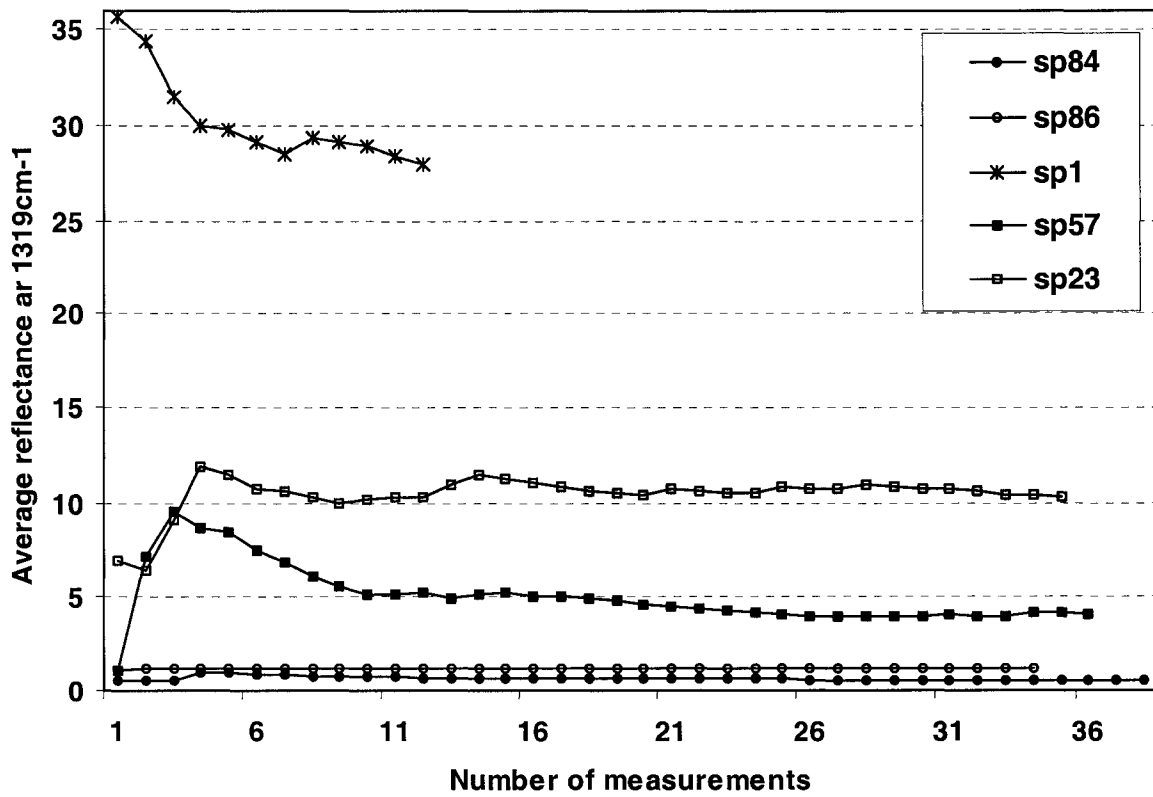


Figure 5.8 Average reflectance at  $1319\text{ cm}^{-1}$  of five samples as a function of the number of measurements on each sample.

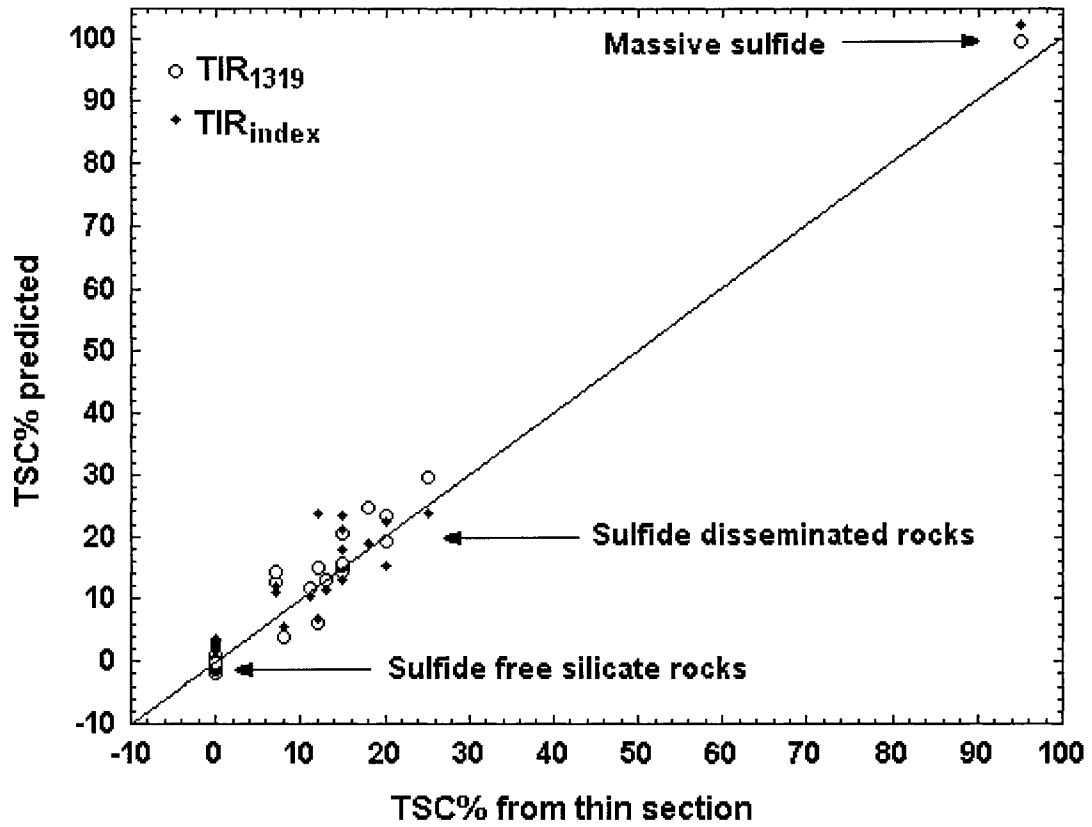


Figure 5.9 Scatter plots of observed total sulfide from thin section analysis and predicted total sulfide by  $TIR_{1319}$  and  $TIR_{ratio}$ .

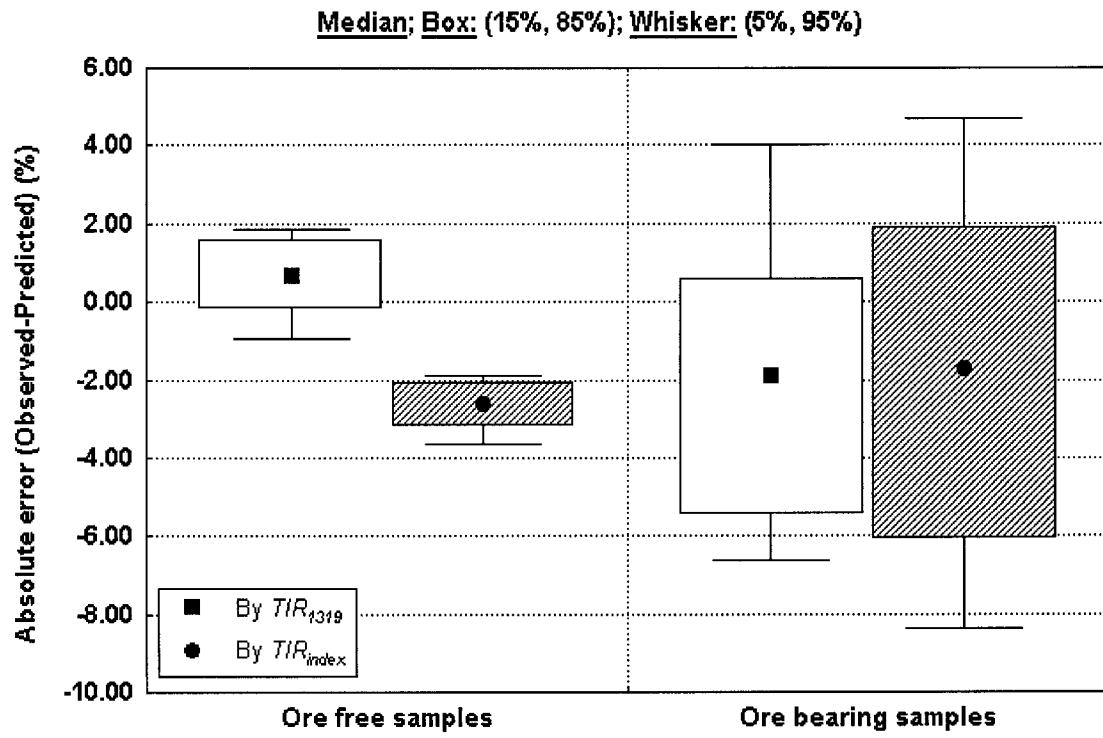


Figure 5.10 Error distributions for ore free samples and ore containing samples



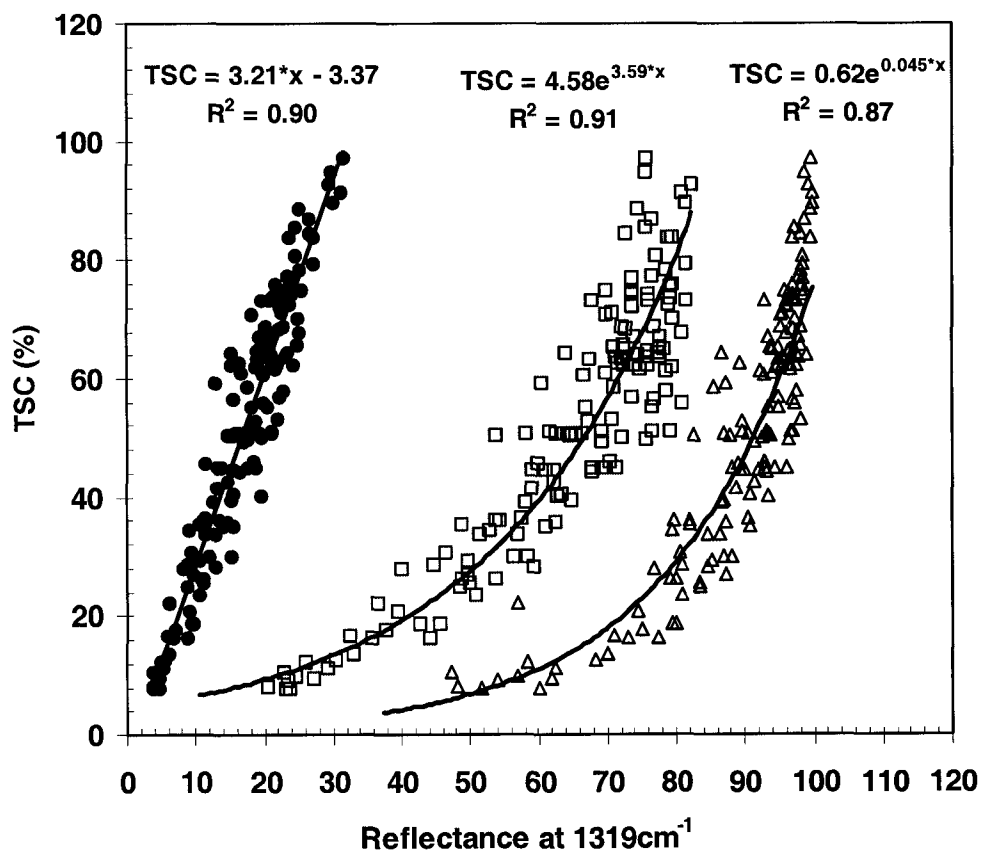


Figure 5.11 The effect of continuum removal on the relationship between TSC and reflectance at 1319cm<sup>-1</sup>. Black dots: original reflectance at 1319cm<sup>-1</sup>; squares: reflectance at 1319cm<sup>-1</sup> after continuum removal over 500 cm<sup>-1</sup> to 5000 cm<sup>-1</sup>; triangles: reflectance at 1319cm<sup>-1</sup> after continuum removal over 1080 cm<sup>-1</sup> to 3000 cm<sup>-1</sup>.

## CHAPTER 6

### SUMMARY AND CONCLUSIONS

This study has explored the usefulness of hyperspectral data to discriminate rock units and estimate the abundance of sulfides (chalcopyrite + pyrrhotite + pentlandite) in rocks. Four different research themes were explored corresponding to different geological application scenarios and demonstrating the potential of retrieving useful lithological information from rock spectra while minimizing detrimental effects from topography, moisture in the underground environment and surface properties of rocks. Salient achievements of this thesis include:

- (a) The topographic correction of CASI hyperspectral data at the pixel scale reconstructs a uniform solar illumination. This research demonstrates that for two of the major rock endmembers investigated (gabbro and peridotite) the DEM correction process, which uses publicly available topographic maps, can effectively reduce the variation in detected radiance due to changes in local illumination. Specifically, rock units located on sloping terrain, whose endmember signatures were initially difficult to isolate, became clearly identifiable after undertaking the topographic correction. A multi-dimensional view of CASI data also shows that topography has the effect of expanding endmember clusters; the correction process shrank the endmember clusters toward their virtual original positions. This study indicates that a topographic correction is beneficial for retrieving geologically meaningful rock unit endmember signatures from hyperspectral data acquired over rugged terrain.

- (b) Rock type discrimination for a simulated underground environment was conducted using 2<sup>nd</sup> order derivative thermal infrared reflectance spectra and demonstrates the feasibility of mapping rock faces in an underground environment. An innovative method applying the spectral angle mapper algorithm to 2<sup>nd</sup> derivative rock spectra has shown to be robust for minimizing the effects of liquid water on the rock surface, variations in local geometry and the presence of disseminated sulfides while preserving diagnostic rock signatures from 700-1300 $\text{cm}^{-1}$  necessary for rock type identification. An average accuracy of above 80% for rock type determination was achieved for all rock types tested. This study suggests that it is possible to automate the discrimination of rock types in an underground environment and provide real time lithologic information from cores for mine exploration, using thermal infrared reflectance spectroscopy.
- (c) An important finding for sulfide ore detection in broken silicate rocks is that, in the region of 1319  $\text{cm}^{-1}$ , most known silicate minerals converge to a common reflectance minima (less than 1.5%) but massive and disseminated sulfides have distinctly higher reflectance. Individual sulfide minerals (chalcopyrite, pyrrhotite, pentlandite) however, do not reveal diagnostic features in this spectral region. When sulfides are disseminated in the host rock, the average reflectance of the rock increases but the correlation with abundance is not systematic. However, the total sulfide concentration (TSC) as a function of continuum removed reflectance (CRR) is systematic. The empirical correlation between CRR at 1319  $\text{cm}^{-1}$  versus the total sulfide

concentration, estimated via thin section point counts, gives a coefficient of determination value ( $R^2$ ) of 0.93 for measurement of dry and wet surfaces when averaged. Similar results are observed when dry and wet locations are analysed separately. The relationship demonstrates the feasibility to estimate total sulfide concentration from TIR reflectance data even when samples are wet.

- (d) Further study on the estimation of sulfide ore from cut rocks and cores has identified a linear relationship between reflectance at  $1319\text{cm}^{-1}$  and TSC and has shown that TSC is exponentially related to a specific TIR band ratio ( $0.5 * \text{TIR}_{995} / \text{TIR}_{1319} + 0.5 * \text{TIR}_{1180} / \text{TIR}_{1319}$ ). Results show that sulfide-containing samples can be separated from barren host rocks with 90% confidence when TSC is greater than 7.68%. TSC can also be estimated from TIR data with a mean error of 2.27% and a standard deviation of less than 6.19%, when compared to estimates from thin sections. Removal of the continuum, which is often used to highlight spectral signatures in hyperspectral analysis, results in a non-linear TSC-TIR relationship. For cut rocks and cores, removal of the continuum is not necessary for ore detection and grade estimation.

Removal of the continuum as discussed in chapter 4 (published in 2001 in *Geophysics, vol. 66*) helps to minimize the effects of micro-topography on broken rocks and highlights the TSC-TIR relationship at  $1319\text{cm}^{-1}$ . As the research evolved, removal of the continuum was found to be unnecessary for the analysis of spectra for cut rock surfaces for which the measurement geometry is more constant than that of broken rocks.

Because the calculation of the continuum is dependant on the selection of the spectral range where the removal process is applied, an additional calibration step is required to calibrate the sulfide prediction models (in chapter 5).

The research in this thesis has expanded previous spectroscopy studies, which are mostly case-based or limited to the laboratory, by providing a wider scope for geological applications, especially the application of thermal infrared reflectance data to solve problems encountered by the mining industry. The research was conducted with a view towards the automation of mine operation and the design of appropriate prototype instruments of benefit to industrial partners, and to make significant contributions to the application of spectroscopy in geology. Though the usefulness and feasibility of using hyperspectral data for rock unit discrimination and sulfide ore detection was demonstrated in this thesis, much work remains to transform these research results into state-of-art technology designed for a mining application.

## **APPENDIX A**

### **EFFECT OF CHANGES IN INSTRUMENT FIELD OF VIEW ON THE ESTIMATION OF SULFIDE ORE**

#### **A1. Problem description and approaches**

In Chapter 5, the instrument instantaneous field of view (FOV) of the MB102<sup>TM</sup> spectrometer was set to different sizes for cut rock (5 mm x 5 mm) and core (4 mm x 4 mm) samples. This did not cause an obvious discrepancy in the results of total sulfide estimation and the sulfide prediction models worked consistently well for the cores and cut rocks under the given sampling strategy. However, it is important to quantitatively explore possible effects of varying the size of the FOV on sulfide estimation from spectra. This information will provide critical knowledge for applying the sulfide prediction models to real core logging scenarios, especially for the design of instruments and sampling strategies in customized applications.

Spectra collected on sp#8 (see Chapter 5 for sample description) were used to explore possible FOV effects on the estimation of sulfides. There were 144 independent measurements/spots (5 mm x 5 mm FOV) with known local (within each grid) total sulfide readings obtained from a high-resolution digital photo. Because the TIR measurement at each spot is independent of those of adjacent spots, it is statistically valid to mathematically average the spectra from more than two adjacent spots to simulate one spectrum under a larger virtual spot, which was assumed to be a linear mixture of spectra from those spots involved in the average process. The mixing systematics is basically linear if the components are arranged in spatially distinct patterns, analogous to the

squares on a checkerboard (Nash and Conel, 1974; Singer and McCord, 1979). The averaging process meets the checkerboard assumption.

As illustrated in Figure A1, the new virtual spot (FOV footprint) can be square or rectangular in shape with dimensions that may be many times that of the original spot size ( $25 \text{ mm}^2$ ). When  $dx$  is equal to  $dy$ , the new FOV is a square but it can be a rectangle if  $dx$  is not equal to  $dy$ . While moving the new FOV window (square or rectangle) over the entire surface of sp#8, spectral data for a bigger virtual FOV over the same sample surface can be simulated. Both square and rectangular FOV shape were simulated in this study. For square FOV, five different sizes were tested with  $dx=dy=10\text{mm}$ ,  $15\text{mm}$ ,  $20\text{mm}$ ,  $25\text{mm}$  and  $30\text{mm}$ . For rectangle FOV,  $dx$  was fixed to  $5\text{mm}$  and  $dy = 10\text{mm}$ ,  $15\text{mm}$ ,  $20\text{mm}$ ,  $25\text{mm}$  and  $30\text{mm}$ . The rectangle FOV was explored with a view towards core logging using hyperspectral devices because the use of a rectangular FOV makes it possible to minimize curvature effects for cores whose diameters are generally less than 2 inches.

## **A2. Analysis of data from various FOV**

The statistics of TSC (%) and  $\text{TIR}_{1319}$  data (in percent, thermal infrared reflectance at  $1319 \text{ cm}^{-1}$ ) will be explored for varying FOV shape (rectangle and square) and size to examine the possible effects on the linear TSC-TIR relationship presented in Chapter 5. Three kinds of data for the rock slab are available for this analysis: (1) total sulfide content (TSC%) counted at each spot from the digital photo; (2) TIR spectrum at each spot; (3) sulfide content of 47.9% for the whole sample based on the analysis of the thin section.

### **A2.1 Square FOV**

When  $dx=dy$  and  $dx$  is changed from 1 to 6 times that of the original size (5mm), the area of the FOV changes from 1 to 4, 9, 16, 25, and 35 times the original size respectively. The basic statistics of the local TSC and  $TIR_{1319}$  (Table A1 and Figure A2) for the new FOV show that,

- (a) The mean TSC value counted from the new grid system is stable (51.40% ~ 50.88%, Figure A2a and Table A1) and tends to approach the thin section value (47.9%) when applying the largest FOV. This indicates that a larger FOV generally provides a more representative reading for the entire rock face. The 0.52% difference between 51.40% (TSC counted at the smallest FOV) and 50.88% (TSC counted at the largest FOV) is mainly due to the edge effect from the pixels under virtual grid lines, which are 1 pixel wide.
- (b) The mean TIR value at  $1319\text{cm}^{-1}$  ( $TIR_{1319}$ ) from the new grid system is also stable (Figure A2a and Table A1) and is approaching the value of 16.04%, (the expected  $TIR_{1319}$  value for 47.9% TSC based on the linear model between TSC and  $TIR_{1319}$  described in Chapter 5) as the FOV increases.
- (c) The standard deviation for TSC and  $TIR_{1319}$  consistently decreases with increasing FOV size (Figure A2b). This indicates that a larger FOV is more reliable in terms of providing a stable and representative TIR spectra and local TSC data.

From the scatter plots of  $TIR_{1319}$  and TSC over different FOV sizes (Figure A3), it is obvious that while the FOV is increasing, the data clusters tend to shrink and approach the point where  $TSC=47.9\%$  and  $TIR_{1319}=16.04\%$ , which is the “true” data for sample sp#8 assuming that the linear TSC-TIR model in Chapter 5 is valid when the FOV



changes.

To validate the above assumption, the  $TIR_{1319}$  sulfide estimation index from Chapter 5 was applied to the TIR data set for new FOV sizes. The predicted sulfide contents using the  $TIR_{1319}$  model were compared with the local TSC established from the analysis of the digital photo. The results were evaluated using the same methods as that used in Chapter 5, including the absolute prediction error ( $e$ ), which is defined as observed total sulfide content (% from digital photo analysis) minus predicted TSC (% estimated from  $TIR_{1319}$  model), the mean ( $m$ ) of the absolute prediction error, which is calculated from the statistical distribution of the absolute errors and the standard deviation of the absolute prediction error ( $stdev$ ), which delineates the variation of absolute errors. As the field of view increases in size, the absolute sulfide prediction error at each spot generally decreases as illustrated in Figure A4, for which the biggest error drops from 23% (5mm x 5mm FOV) to less than 7% (30mm x 30mm). The standard deviation of the prediction error (Table A2 and Figure A5a and A6a) also systematically decreases when using a larger FOV. This indicates that the TIR-TSC prediction model works better with a larger FOV. The mean error varies from  $-0.42\%$  to  $0.07\%$  about zero without significant changes for different FOV sizes, suggesting that the  $TIR_{1319}$  model is unbiased for sulfide estimation at different FOV sizes.

When the confidence of the sulfide estimation is set to 90%, the absolute estimation errors are confined within  $\pm 7.28\%$  for a FOV of 5mm x 5mm to  $\pm 1.85\%$  for a FOV of 30mm x 30mm (Table A2) based on the error distribution seen in Figure A5a. This indicates that a larger FOV is preferred for reliable sulfide estimations.

## **A2.2 Rectangle FOV**

Five rectangular FOV sizes of 5mm x 5mm, 5mm x 15mm, 5mm x 25mm and 5mm x 35mm were examined. Similar results were found as those for square FOV. When the size of the rectangular FOV increases, the linear prediction remains unbiased with a near zero (<0.07%) mean prediction error (Figure A5b) and the deviation of the estimation error systematically decreases (Figure A6b). When the confidence level is set to 90% correctness, the error envelope for the prediction drops from  $\pm 7.28\%$  to  $\pm 4.32\%$ .

As the mean error remains stable near zero for both square and rectangular FOV, the standard deviation of absolute prediction errors (*stdev*) can be used to define the envelope of distribution of total sulfide estimation errors. An interesting finding is that the *stdev* decreases as a logarithmic function of the footprint area in  $\text{mm}^2$  (Figure A7). Data for six footprint sizes ranging from  $0.25\text{mm}^2$  to  $9.00\text{mm}^2$  (for square FOV) and four footprint sizes (for rectangular FOV) ranging from  $0.25\text{mm}^2$  to  $1.75\text{mm}^2$  tested are shown on Figure A7. Both data sets fit the logarithmic function well.

### **A3 Conclusions**

The following conclusions can be drawn from this investigation

- (a) The relationship between thermal reflectance at  $1319\text{cm}^{-1}$  and local total sulfide content remains linear at different FOV. The  $\text{TIR}_{1319}$  prediction model provides an unbiased estimation with near zero mean error (less than 0.42%).
- (b) The total sulfide estimation for the largest FOV has smaller estimation errors. The maximum error decreases from 23% absolute to less than 7% as the FOV increases from 5mm x 5mm to 30mm x 30mm.
- (c) The standard deviation of the estimation error systematically decreases logarithmically as the FOV increases. When the FOV area increases from 0.25

mm<sup>2</sup> to 9.00 mm<sup>2</sup>, the *stdev* of the prediction errors drops from 4.43% to 1.35% absolute.

- (d) Square and rectangle FOV gives similar results indicating that the shape of the FOV does not introduce noticeable differences in the estimation of sulfide abundance for flat cut rock surface but the footprint area is the dominant factor modulating the distribution of errors. This indicates that sulfide estimation models can be used on spectra collected with a rectangular FOV when necessary.

A general conclusion is that a larger FOV should be used for an instrument setup when attempting the estimation of sulfides from TIR spectra, especially for heterogeneous samples. A FOV can be devised to adjust the footprint area to fit the physical dimensions of targets and the target textural heterogeneity.

## REFERENCES

- Nash, D.B. and J.E. Conel, 1974, Spectral reflectance systematics for mixtures of powdered hypersthene, labradorite, and ilmenite. *J. of Geophys. Res.*, **79**, 1615-1621.
- Singer, R. B. and T. B. McCord, 1979, Mars: Large Scale Mixing of Bright and Dark Surface Materials and Implications for Analysis of Spectral Reflectance. *Proceeding of the Lunar Planetary Science Conference, 10th*, 1835-1848.

Table A1 Basic statistics of TSC and TIR1319 over varying square FOV

<b>FOV size</b>	<b>1x1<sup>(4)</sup></b>	<b>2x2</b>	<b>3x3</b>	<b>4x4</b>	<b>5x5</b>	<b>6x6</b>
<b>Footprint (mm<sup>2</sup>)</b>	0.25	1.00	2.25	4.00	6.25	9.00
<b>TSC (%) <i>Stdev</i><sup>(a)</sup></b>	22.31	18.83	16.31	13.97	12.38	10.73
<b>TSC (%) <i>Mean</i><sup>(b)</sup></b>	51.40	51.35	51.26	51.15	51.03	50.88
<b>TIR1319<sup>(c)</sup> (%) <i>Stdev</i></b>	6.58	5.68	5.09	4.45	4.00	3.44
<b>TIR1319 (%) <i>Mean</i></b>	17.04	17.17	17.04	17.11	16.90	16.99

<sup>(a)</sup> Standard deviation of readings from all virtual spots over the entire rock face. <sup>(b)</sup> Mean value of readings from all virtual spots over the entire rock face. <sup>(c)</sup> Thermal infrared reflectance value at 1319cm<sup>-1</sup>. <sup>(4)</sup> N x N FOV sizes represent (Nx5mm) x (Nx5mm) square FOV coverage.

Table A2 TSC prediction errors from TIR<sub>1319</sub> model under different square dimensions of FOV

FOV size	1x1 <sup>(a)</sup>	2x2	3x3	4x4	5x5	6x6
Mean ( <i>m</i> ) of absolute prediction error (%)	0.01	-0.42	0.01	-0.34	0.07	-0.36
<i>stdev</i> of absolute prediction error (%)	4.43	2.98	2.44	1.82	1.56	1.35
<i>m</i> +1.64* <i>stdev</i> (%)	7.28	4.46	4.00	2.64	2.62	1.85

(a) N x N FOV sizes represent (Nx5mm) x (Nx5mm) square FOV coverage.

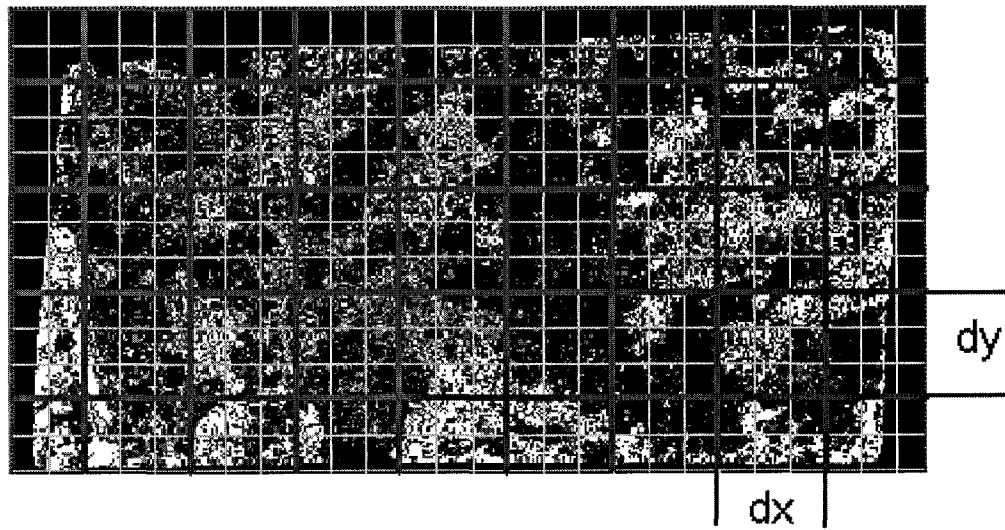
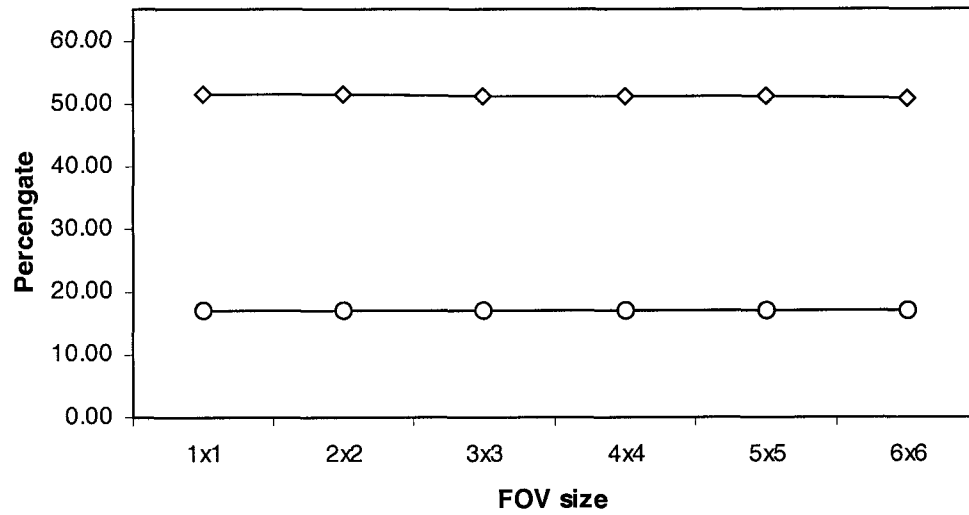


Figure A1 Schematic representation of simulating variable field of views on the cut surface of rock sample sp#8.

(a)



(b)

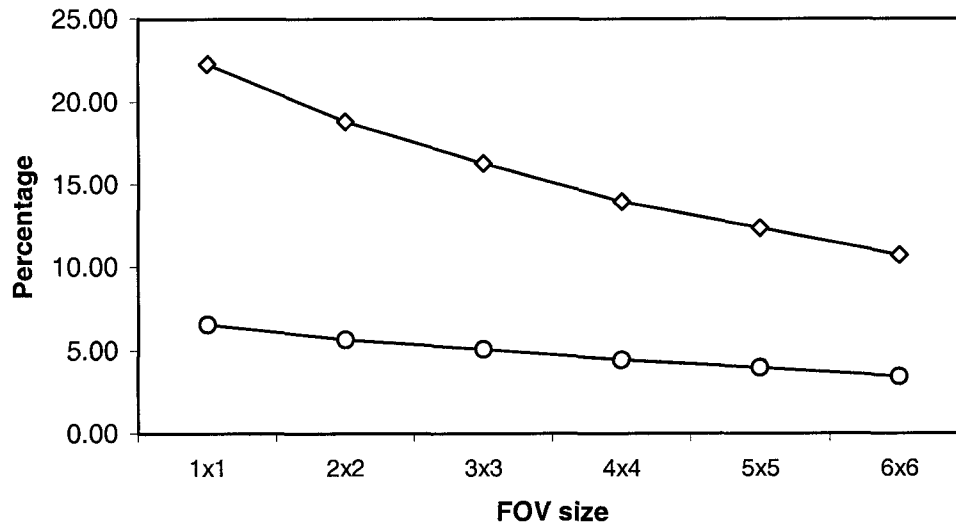


Figure A2 (a) Mean TSC (diamond, from digital photo) and mean TIR1319 (circle, from spectra) for all pixels at a given FOV. Results are shown for square FOV ranging 25 - 900mm<sup>2</sup>; (b) Standard deviation of local TSC (diamond) and TIR<sub>1319</sub> (circle) under various square FOV sizes.

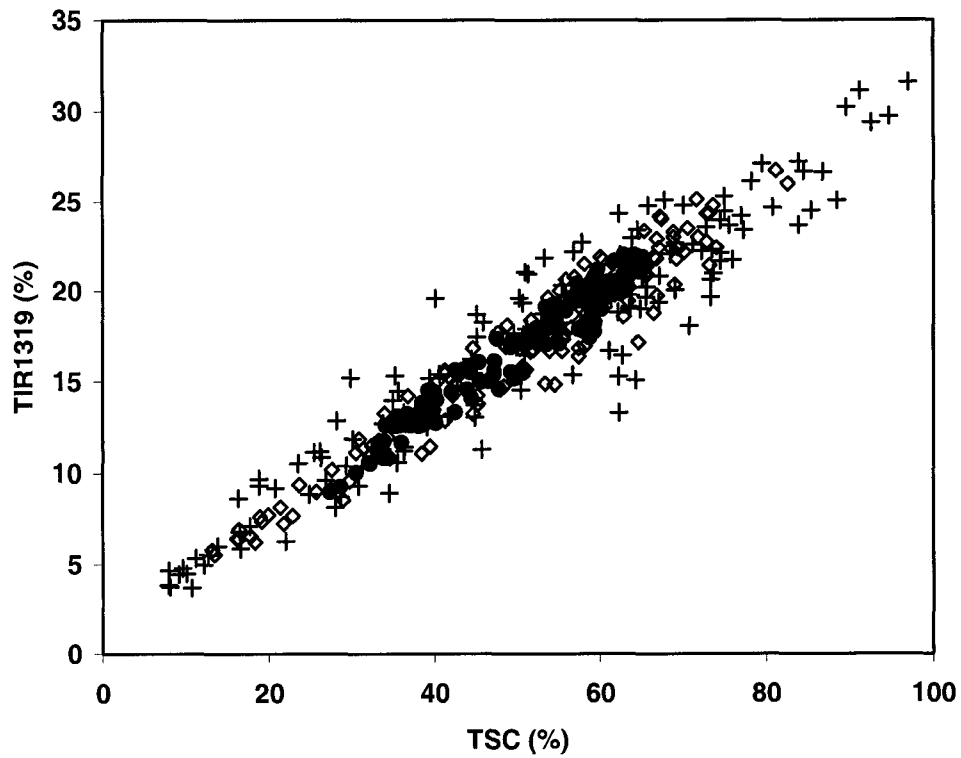


Figure A3 Scatter plot of local total sulfide content (TSC) vs. thermal infrared reflectance at  $1319\text{ cm}^{-1}$  (TIR1319) at different square field of view sizes. Cross=5mm x 5mm FOV; Diamond=15mm x 15 mm FOV; Black dot=30mm x 30 mm FOV.



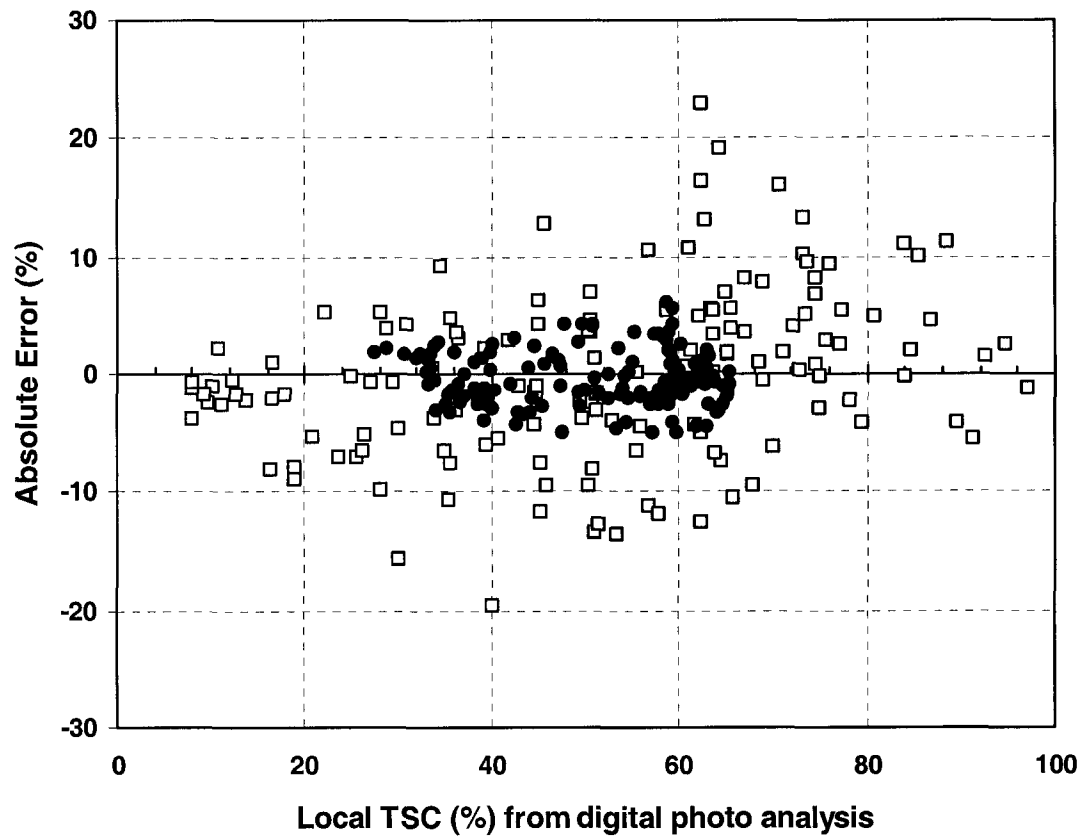


Figure A4 Distribution of absolute prediction errors at different total sulfide concentration under 5mm x 5mm (square) and 30mm x 30 mm (black dot) field view setups.

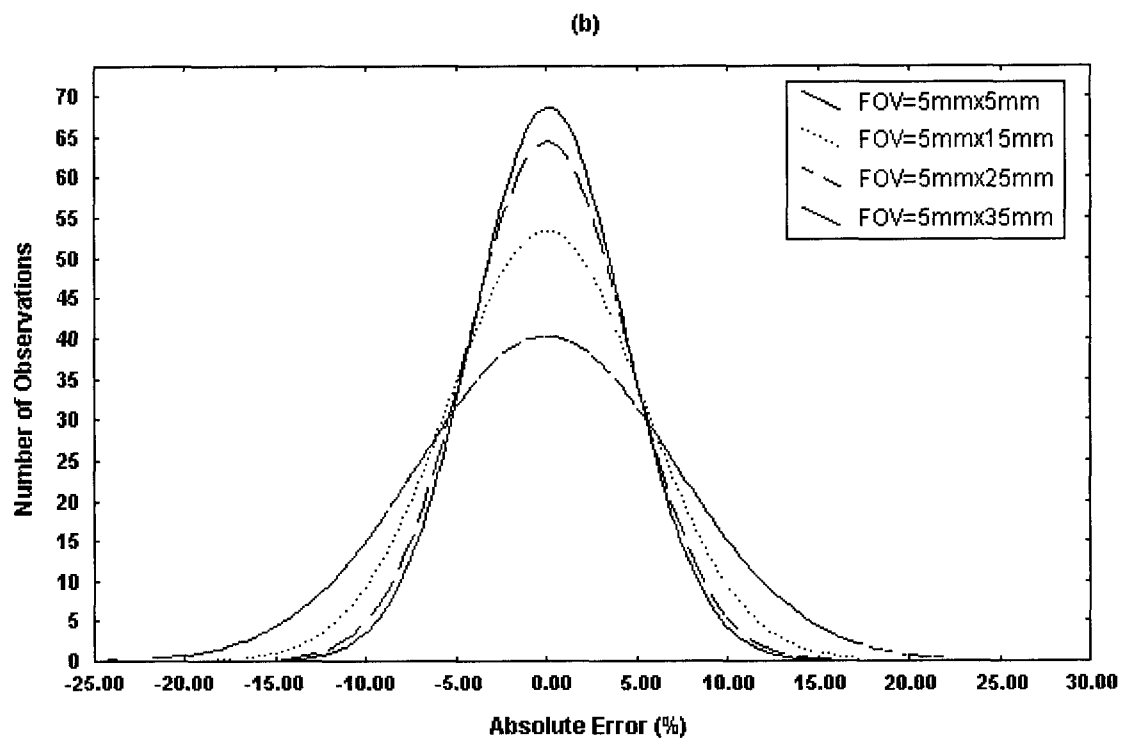
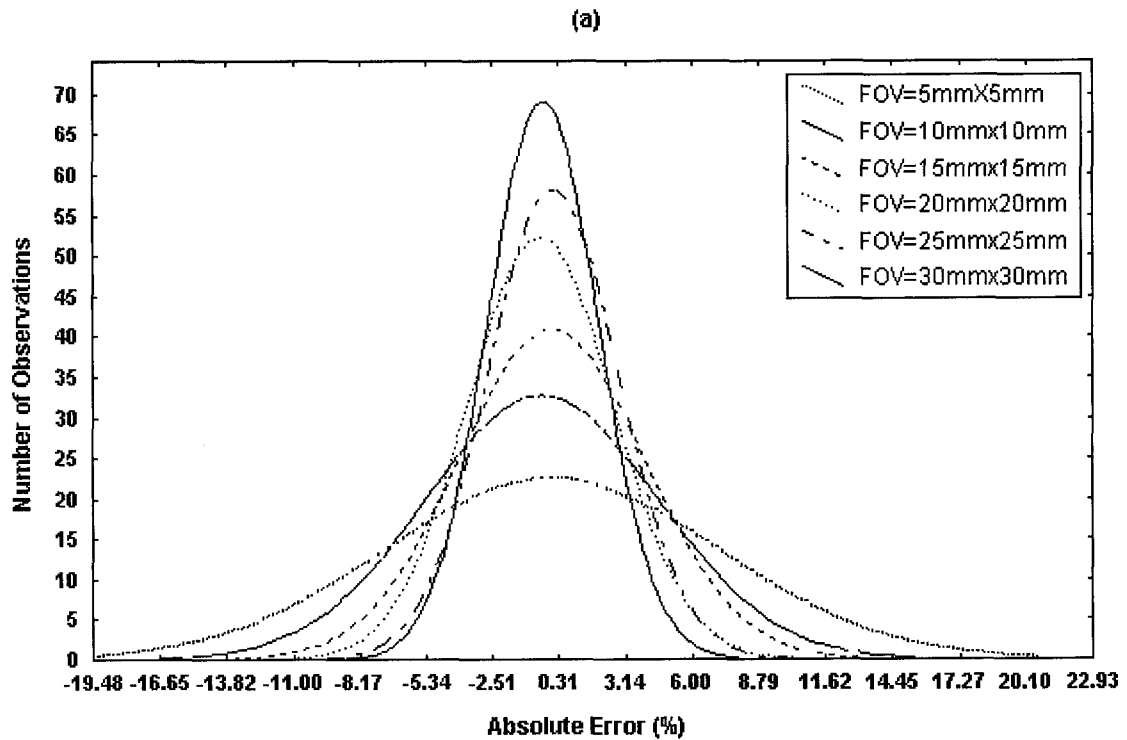


Figure A5 Distribution of total sulfide prediction errors from TIR<sub>1319</sub> model at different square (a) and rectangle (b) FOV sizes.

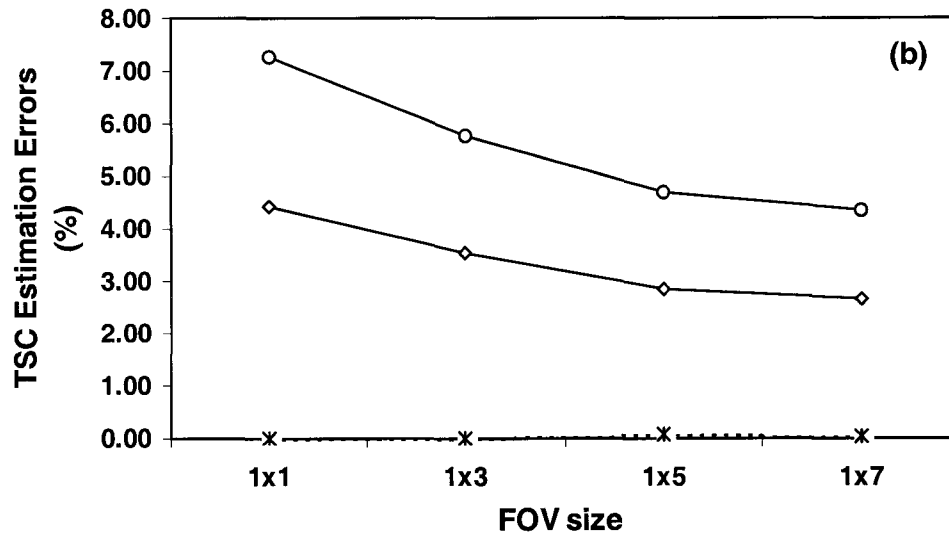
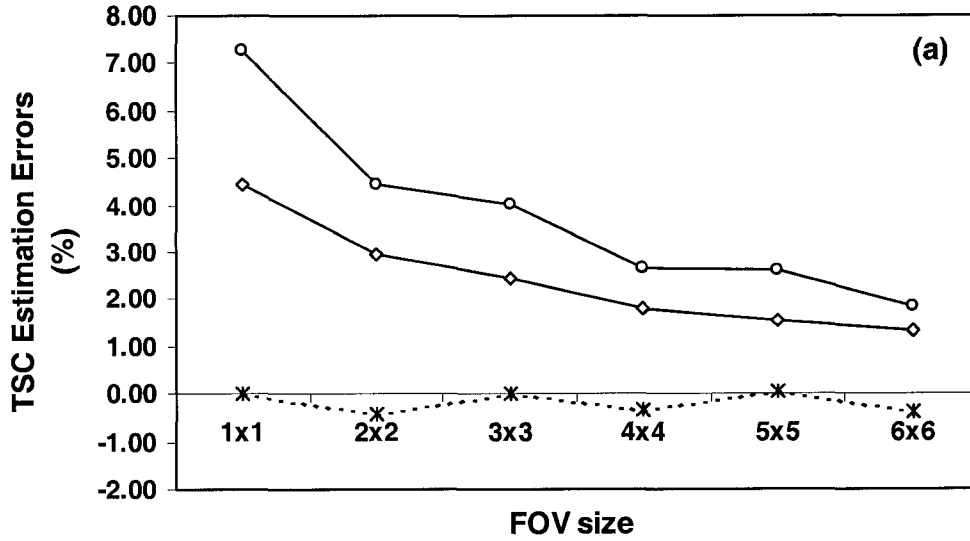


Figure A6 Variation of mean and deviation of total sulfide prediction errors from TIR<sub>1319</sub> model under different square (a) and rectangle (b) FOV sizes. 1 x 1 is original 5mm x 5mm square FOV. N x N FOV sizes represent (Nx5mm) x (Nx5mm) square FOV. Star= mean (*m*) absolute prediction error; Diamond=standard deviation (*stdev*) of absolute prediction error; Circle=  $m+1.64*stdev$ .

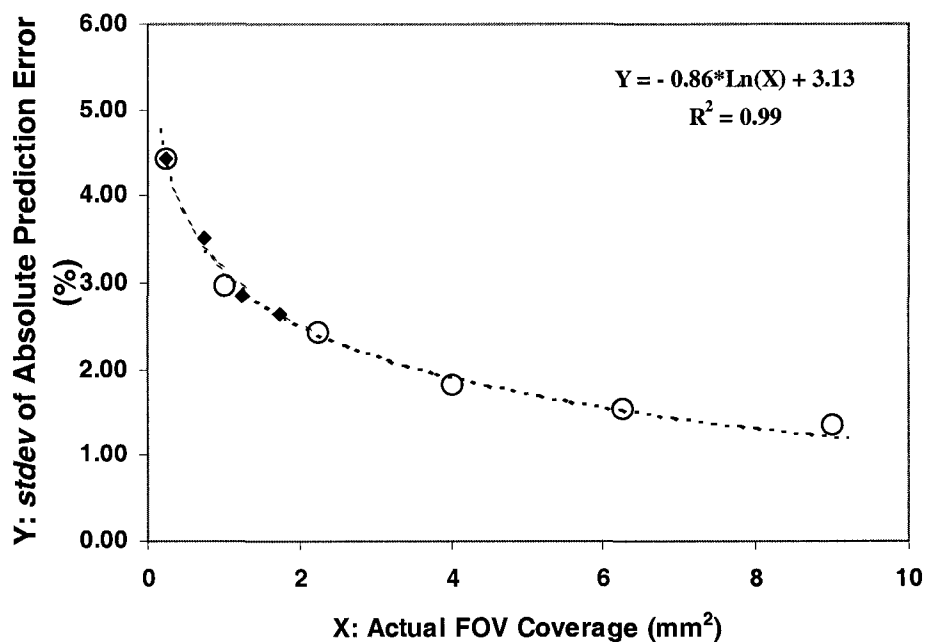


Figure A7 Relationship between standard deviation of sulfide prediction errors from TIR 1319 model and physical field of view coverage. Empty circle=data from square FOV setup; Black diamond=data from rectangle FOV setup; Dotted line= logarithm fit.

## **APPENDIX B**

### **THEORY AND PROCESSING TOOLS FOR TIR SPECTROACOPIY OF GEOLOGIC MATERIALS**

#### **B.1 Spectroscopy**

Spectroscopy is the study of interactions of electromagnetic radiation with materials. Spectrometers are used to measure emitted or reflected photons from a target as a function of wavelength. Because the density of the measured photons is affected by scattering and absorption processes occurring during the photon-target interactions which are modulated by the target composition, the measured spectra is indicative of the chemical composition of the target.

Spectroscopy is used in the laboratory, in the field, from aircraft and satellites. Reflectance and emittance spectroscopy of natural surfaces are sensitive to specific chemical bonds in materials, whether solid, liquid or gas. Spectroscopy has the advantage of being sensitive to both crystalline and amorphous materials. Its historical disadvantage is that it is so sensitive to small changes in the chemistry and/or structure of a material that special methods must be employed for data analysis.

The variations in material composition often cause shifts in the position and shape of absorption bands in the spectrum. With the vast chemical variety typically encountered in the real world, spectral signatures can be quite complex and sometimes unintelligible. However, an increased knowledge of the natural variation of spectral features and a better understanding of the causes of the observed shifts combined with rapidly improving computing resources have turned the disadvantage into an advantage, allowing us to probe in increasing detail the chemistry of terrestrial materials. Imaging spectroscopy is a

relatively new technique providing a spectrum for each position of a large array of spatial positions for many spectral wavelengths (hyperspectral image). The data might be for a rock measured in the laboratory, in the field or from an aircraft, or of a whole planet from a spacecraft or Earth-based telescope. By analyzing the spectral features, and thus specific chemical bonds in materials, one can map where those bonds occur, and thus map materials.

Thermal Infrared Reflectance (TIR) spectroscopy generally refers to the traditional mid-infrared (MIR) spectral region, 3.0 to 30  $\mu\text{m}$ , which covers thermally emitted energy which for the earth peaks near 10  $\mu\text{m}$  and decreases beyond the peak with a shape controlled by gray-body emission. In this region, Kirchoff's Law (Nicodemus, 1963) and the relationship between reflected and absorbed light reveal the basic theory of spectroscopy.

## **B.2 Absorption and reflection of minerals and rocks**

When a stream of photons encounters a rock surface, a subset is reflected and some are refracted into the rock. All minerals and rocks have a complex refraction index,

$$m = n - j * K$$

where  $n$  is the real part of the index,  $j = (-1)^{1/2}$ , and  $K$  is the imaginary part of the index of refraction.  $K$  dictates how far photons can travel into the material. When photons enter the sample, they are absorbed according to Beers Law,  $I = I_o e^{-kx}$ , where  $I$  is the observed intensity,  $I_o$  is the original light intensity,  $k$  is an absorption coefficient and  $x$  is the distance traveled through the medium. The absorption coefficient  $k$  is related to the complex index of refraction by the equation,  $k = 4\pi * K / \lambda$ , where  $\lambda$  is the wavelength of light. The reflection of light,  $R$ , normally incident onto a plane surface is described by

Fresnel equation,

$$R = [(n - 1)^2 + K^2] / [(n + 1)^2 + K^2]$$

All the above equations hold for a single wavelength. The absorption coefficient and index of refraction vary with wavelength, and thus the observed reflected intensity varies. The absorption coefficient as a function of wavelength is a fundamental parameter describing the interaction of photons with a material. In practice, only reflectance is measured. The relationship between reflectance and absorption makes it possible to determine the absorption property of rocks by measuring reflected light.

The real part of the index of refraction ( $n$ ) generally varies less than the absorption coefficient as a function of wavelength, especially at visible and near-infrared wavelengths, where electronic processes (absorption of photons at a specific wavelength causes a change of isolated atoms and ions from one energy state to a higher one) dominate the absorption process. At longer wavelengths,  $n$  reaches a minimum value (near 8.5  $\mu\text{m}$  for most silicate minerals) at a frequency called the Christensen frequency resulting in a minimum in reflected light (Figure B.1a). The exact location of the observed reflectance minimum is also controlled by the absorption coefficient  $K$ . At longer wavelengths  $K$  rapidly increases for silicate minerals giving rise to a maximum in reflectance known as the reststrahlen band (Figure B.1b). The location of this band corresponds to a fundamental vibrational stretching process, which dominates the absorption process of silicate minerals in the TIR region. In the laboratory, TIR is measured by illuminating the sample and measuring the reflected component.

### **B.3 Emissivity and reflectance in the thermal spectral region**

In many applications of thermal infrared spectroscopy, the surface investigated cannot be illuminated artificially. This is the case for airborne and spaceborne imaging. In such case, rock and mineral reflectance signatures can be estimated using measurements of emissivity ( $E$ ).  $E$  is defined as,  $E = L_\lambda / L_\lambda^B$ , where  $L_\lambda$  is the spectral radiance of the measured target, and  $L_\lambda^B$  is the blackbody radiance at an equivalent temperature, which is given by

$$L_\lambda^B = C1/[\lambda^5 \pi (e^{C2/(T\lambda)} - 1)]$$

where  $\lambda$  is wavelength,  $T$  is temperature and  $C1$ ,  $C2$  are radiation constants. Kirchoff's Law relates emissivity to reflectance ( $R$ ) by

$$R = 1 - E$$

This relationship holds for most geological materials (Salisbury, 1993) in the thermal region and thus reflectance can be calculated from the emissivity spectra.

### **B.4 TIR research in geology and TIR spectral library of rocks and minerals**

TIR geological applications have been conducted for decades. Most of the TIR geological applications are based on the relationship between  $R$  and  $E$ . Early research was conducted by Lyon in 1965 and 1972 and the key conclusion is that details of the spectral shape, intensity and individual secondary minima (or maxima) could reveal specific differences between mineral assemblages or within mineral groups in rocks. Vincent (1975) focused on the 7-14  $\mu\text{m}$  reflectance spectra of 26 different igneous rocks and found that most of these rocks have a reflectance minima around 11.75  $\mu\text{m}$  where the Christensen frequency (CF, Christensen, 1992) occurs. Walter (1989) found that the TIR



reflectance of rocks was correlated with the SCFM chemical index, which is defined as  $\text{SiO}_2/(\text{SiO}_2+\text{CaO}+\text{FeO}+\text{MgO})$ . This meant that quartz-rich rocks should be separable from mafic rocks. Nash (1991) found that plagioclase composition in rocks can be identified by a systematic band shifts (from 7.6 to 8.0  $\mu\text{m}$ ) as the anorthite content increases from 0% to 100%.

Work by Hunt (1976), Richard (1979), Gillespie (1984), Khale (1980, 1988), Christensen (1992) used emission or reflectance spectra for the compositional analysis of various geological materials. A wealth of laboratory spectra for minerals and rocks was reported by Salisbury (1991, 1993). The data illustrates the systematic absorption troughs and reflection peaks resulting from vibrational motions of bonds within crystalline materials. The strength of absorption/reflection features and their position vary with mineral composition and crystal structure and provide a possible means to determine mineral composition and rock type remotely. The spectra collected by Salisbury are now in the public domain as a TIR spectral library accessible via the John Hopkins University and found in some of the hyperspectral data processing software systems such as ENVI<sup>TM</sup> (The Environment for Visualizing Images).

### **B.5 Hyperspectral data analysis software**

Most of the current remote sensing data processing software systems such as ENVI, PCI<sup>TM</sup> (PCI Geomatics), ERDAS Imagine<sup>TM</sup> (ERDAS, inc.), TNT<sup>TM</sup> (MicroImages, Inc.), ISDAS (Canada Center for Remote Sensing), and ISIS (United States Geological Survey) provide some level of hyperspectral analysis functionalities. ENVI is built on IDL (The Interactive Data Language) and includes traditional processing techniques but the strengths of the software are dedicated techniques for hyperspectral data analysis and

visualization, which include extraction of spectral profiles, comparison with library spectra, spectral math, the Spectral Angle Mapper classification (SAM), linear spectral unmixing, Matched Filtering and spectral endmember visualization tools. The detailed references of these algorithms are documented in the ENVI user manual. ENVI also provides a user-friendly interface for the development of new functions. The spectral data processing conducted for this thesis was performed in ENVI with a small amount of programming in the IDL/ENVI environment.

## REFERENCES

- Christensen, P.R., 1992, Thermal emission spectrometer experiment: The mars observation mission. *J. Geophys. Res.*, **97**, 7719-7734.
- Gillespie, A.R., Kahle, A.B. and Palluconi, F.D., 1984, Mapping alluvial fans in death Valley, California, using multichannel thermal infrared images. *J. Geophys. Res.*, **11**, 1152-1156.
- Hunt, G.R. and Salisbury, J.W., 1976, Mid-infrared spectral behavior of metamorphic rocks. Environmental Research Paper **543-AFCRL-TR-76-0003**, Hanscom Air Force Base, Air Force Cambridge Research Laboratories, U.S.A.
- Kahle, A.B., Gillespie, E.A., Abbott, M.J., Walker, R.E. and Hoover, G., 1988, Relative dating of Hawaiian lava flows using multispectral thermal infrared images: a new tool for geologic mapping of young volcanic terranes. *J. Geophys. Res.*, **93**, 15239-15251.
- Kahle, A.B., Madura, D.P. and Soha, J.M., 1980, Middle infrared multispectral aircraft scanner data: analysis for geological applications. *Appl. Opt.*, **19**, 2279-2290.
- Lyon, R.J.P., 1965, Analysis of rocks by spectral infrared emission (8-25 $\mu$ m), *Econ.*

Geol. **60**, 715-736.

Lyon, R.J.P., 1972, Infrared spectral emittance in geology mapping: Airborne spectrometer data from Pisgash Crater, Calif. Sciences, **175**, 983-986.

Nash, D.B. and Salisbury, J.W., 1991, Infrared reflectance spectra of plagioclase feldspar. J. Geophys. Res., **18**, 1151-1154.

Nicodemus, F. E., 1963, Radiance. Am. J. Phys. **31**, 368-377.

Richard V.D. and Brian, J.S., 1979, Rocks and rock minerals: John Willey & Sons, New York, U.S.A. 117.

Salisbury, J.W., 1993, Thermal infrared (2.5-13.5  $\mu\text{m}$ ) spectroscopy: Laboratory data, Chapter 4, *in* Pieters, C., and Englert, P., Remote Geochemical Analysis: Elemental and Mineralogical Composition. Cambridge University Press.

Salisbury, J.W., Walter, L.S., Vergo, N. and D'Aria, D.M., 1991, Infrared (2.1-25  $\mu\text{m}$ ) spectra of minerals: Johns Hopkins University Press.

Vincent, R.K., Rowan, L.C., Gillespie, R.E. and Knapp, C., 1975, Thermal infrared spectra and chemical analysis of 26 igneous rock samples. Remote Sensing of Environ., **4**, 199-209.

Walter, L.S. and Salisbury J.W., 1989, Spectral characterization of igneous rocks in the 8- to 12- $\mu\text{m}$  region. J. Geophys. Res., **94(B7)**, 9203-9212.

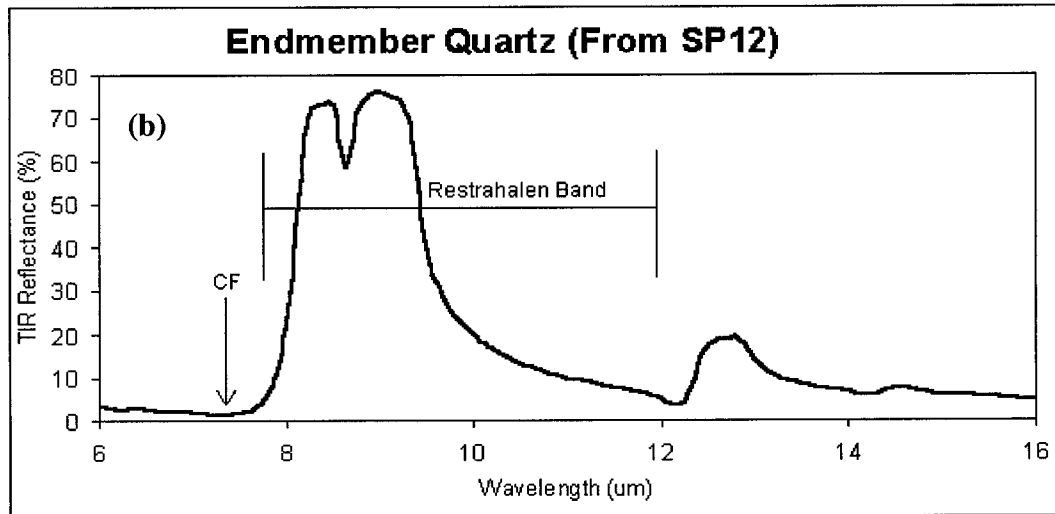
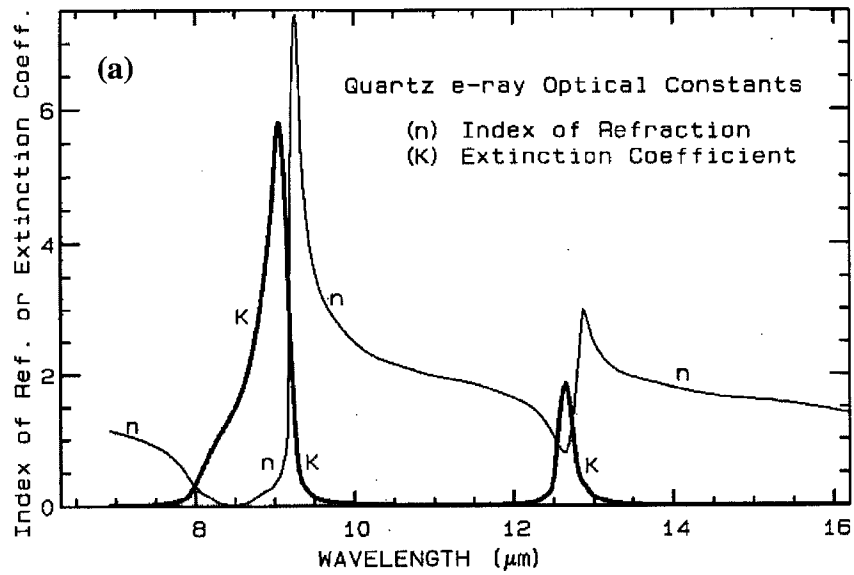


Figure B1 (a) Real (n) and Imagery (K) part of the complex refraction index of quartz (Clark, 1998); (b) TIR reflectance spectrum of quartz measured in this study.